DISSERTATION

The contact area and sliding friction in nanotribological systems

Ausgeführt zum Zwecke der Erlangung des akademischen Grades eines Doktors der technischen Wissenschaften unter der Leitung von

Univ. Prof. Dipl.-Ing. Dr. techn. Peter Mohn

und

Univ. Prof. Dipl.-Ing. Dr. techn. Josef Redinger

und

Priv. Doz. Dr. András Vernes

E 134

Institut für Angewandte Physik

eingereicht an der Technischen Universität Wien

Fakultät für Physik

von

DI Michael Wolloch

0426587

Juchgasse 40/20, 1030 Wien

Wien, am 27. August 2014

Abstract

Although friction, wear, and lubrication have been investigated for hundreds of years, many important questions in the field, now dubbed tribology, remain open. Two of these are the determination of the real contact area and the direction dependence of friction forces on the nanoscale, which are investigated in this thesis.

The invention of the atomic force microscope (AFM) in 1986 by Binnig , Quate, and Gerber was invaluable for the investigation of frictional forces on the atomic scale, giving a boost to the emerging field of nanotribology. While experimental AFM set-ups where quickly modeled with classical molecular dynamic (MD) simulations, the use of *ab-initio* methods on tribological problems remained scarce until recently. In this thesis density functional theory (DFT) is used to develop parameter free methods in the field of nanotribology.

Since the discovery that the apparent contact area can be orders of magnitude larger than the true contact area, the definition and determination of the latter has been an important topic of research. While classical contact mechanics provides satisfactory theories and results for various macroscopic systems, the application of these methods to atomistic systems is dubious, as the contacting bodies are not continuous at this length scale. We developed a parameter free approach to define and calculate the real contact area between two bodies depending on distance. Strong relaxations at distinct distances, like the "jump to contact", which is often observed in AFM experiments, are used to define the onset of contact and Bader's Quantum Theory of Atoms in Molecules is used to calculate the real contact area at a given distance. Bader's method partitions the charge density ρ unambiguously into atoms, which theoretically fill all space and thus give non zero contact areas for all distances. It is therefore necessary to use a density cutoff ρ_{cut} which assigns all regions in space where $\rho < \rho_{\mathrm{cut}}$ to the vacuum, resulting in surface atoms of finite size. In our proposed method the parameter ρ_{cut} is calculated by allowing contact only after the "jump to contact", or a similar discontinuity, has taken place, which can be clearly observed in our DFT simulations. We demonstrate the method by lowering a ten atom tungsten pyramid, which serves as a model of an AFM tip, onto a smooth surface. Two systems are examined, the first being moiré graphene on iridium (111), the second a clean copper (111) surface. Although the surfaces are very different, a similiar cutoff parameter ρ_{cut} of about 5×10^{-2} electrons per Å^3 is computed in both cases. The calculated contact area is found to increasing exponentially with the true relaxed distance between the tip apex atom and the surface atom below it.

Although there exist a number of models that tackle the problem of calculating friction forces on the atomic level, providing a completely parameter-free approach remains a challenge. To examine the direction dependence of dry sliding friction we

developed a quasi-static grid method with a mechanism to allow dissipative sliding, which relies on atomic relaxations. We define two different ways of calculating the mean nanofriction force, both leading to an exponential friction-versus-load behavior for all sliding directions. Since our approach does not impose any limits on lengths and directions of the sliding paths, we investigate arbitrary sliding directions for several metal interfaces and detect two periodic paths which form the upper and lower bound of nanofriction in all cases. For long aperiodic paths the friction force convergences to a value in between these limits. For low loads we retrieve the Derjaguin generalization of the Amontons-Coulomb kinetic friction law which appears to be valid all the way down to the nanoscale. We observe a non-vanishing Derjaguin-offset even for atomically flat surfaces in dry contact. Incorporating our approach to determine the true contact area into the evaluation of the loading force leads to higher loads for each selected pressure. This influences the friction versus load curves by stretching them laterally and thus reducing the coefficients of friction by about 25%–35%.

Kurzfassung

Obwohl sich Wissenschafterinnen und Wissenschafter seit Jahrhunderten mit Reibung, Schmierung und Verschleiß beschäftigen, sind viele wichtige Probleme in diesem, heutzutage als Tribologie bekannten, Feld noch immer ungelöst. Die Definition der Kontaktfläche und die Abhängigkeit der Reibkraft von der Reibrichtung, jeweils auf der atomarer Ebene, sind zwei dieser offenen Fragen und werden in dieser Dissertation behandelt.

Die Erfindung des Rasterkraftmikroskops (AFM), 1986 von Binnig, Quate und Gerber, ermöglichte eine rasante Entwicklung auf dem jungen Feld der Nanotribologie, da nun Reibkräfte auf atomarer Ebene untersucht werden konnten. Auf theoretischer Seite wurden diese Experimente bald durch Molekulardynamik Simulationen beschrieben, die in diesem Feld immer noch von überragender Bedeutung sind. *Ab-inito* Methoden werden allerdings erst seit kurzer Zeit vermehrt verwendet um tribologische Phänomene im Nanobereich zu modellieren. Die vorliegende Arbeit beschäftigt sich im Rahmen der Dichtefunktionaltheorie mit der parameterfreien Beschreibung von tribologischen Problemen.

Seit der Entdeckung, dass die reale Kontaktfläche zwischen zwei Körpern um Größenordnungen kleiner sein kann als die scheinbare, wurden viele Versuche unternommen, um die reale Kontaktfläche zu beschreiben. Klassische Kontaktmechanik ist geeignet um das Verhalten makroskopische Objekte, eventuell mit mikroskopischer Rauigkeit, zu erklären, aber da die Annahme kontinuierlicher, elastischer Körper auf atomarer Ebene nicht mehr gegeben ist, ist es unwahrscheinlich dass solche Theorien auch im Nanobereich gültig bleiben. In dieser Arbeit wird eine Methode vorgestellt um die reale Kontaktfläche auf atomarer Ebene zu definieren und zu berechnen. Dazu werden plötzliche Relaxationen, wie der "jump to contact", der häufig in AFM Experimenten beobachtet wird, verwendet um den Punkt des ersten Kontakts zu definieren. Baders Quantum Theory of Atoms in Molecules wird dann verwendet, um die Größe und Form der Kontaktfläche parameterfrei zu berechnen. Baders Methode teilt die Elektronendichte ρ eindeutig den involvierten Atomen zu, die theoretisch den ganzen Raum ausfüllen. Da dies zu Kontakt bei jedem beliebigen Abstand führen würde, muss die Elektronendichte ab einem bestimmten, kleinen Wert ρ_{cut} auf null gesetzt werden, um Oberflächenatome mit begrenzter Ausdehnung zu erhalten. Dieser Parameter kann über die erwähnte Diskontinuität, z.B. den "jump to contact", bestimmt werden, indem man ρ_{cut} so einstellt, dass Kontakt nur bei Abständen auftritt, bei denen sich die Geometrie bereits geändert hat. Das Konzept wurde an einer Pyramide aus 10 Wolfram Atomen, die eine AFM Spitze simulieren, erprobt, die mit zwei unterschiedliche Oberflächen in Kontakt gebracht wurde. Die zwei getesteten Systeme, Graphene auf fcc Iridium (111) und fcc Kupfer (111), besitzen unterschiedliche Eigenschaften, der berechnete Wert für

iii

ρ_{cut} ist, mit $\sim 5 \times 10^{-2}$ Elektronen pro Å^3, allerdings dennoch in beiden Fällen sehr ähnlich. Für beide Systeme konnte ein exponentieller Zuwachs der realen Kontaktfläche mit veringertem Abstand zwischen den relaxierten Atomen der Spitze und der Oberfläche festgestellt werden.

Die Beschreibung von Reibkräften mit parameterfreien Methoden ist, obwohl einige Modelle existieren, immer noch eine nur unzufriedenstellend gelöste Aufgabe. In der vorliegenden Arbeit entwickeln wir eine Raster-basierte, quasi-statische Methode, um die Richtungsabhängigkeit von Reibkräften zwischen glatten Flächen in trockenem Kontakt zu berechnen. Das Verfahren beruht auf der Annahme, dass der Energieverlust durch Reibung durch die Relaxation der Atome in der Kontaktzone abgeschätzt werden kann. Zwei unabhängige Wege wurden entwickelt, um die Reibkräfte bei konstanter Last aus den mit DFT gewonnenen Daten zu bestimmen. Beide führen zu einem exponentiellen Reibgesetz für alle Gleitrichtungen. Da unsere Methode keine Limits bezüglich der Länge der Reibpfade setzt, konnten auch aperiodische Pfade untersucht werden, bei denen die Reibkraft erst nach sehr langen Distanzen konvergiert. Für alle untersuchten Metall auf Metall Grenzflächen, konnten wir zwei periodische Gleitrichtungen finden, die obere und untere Grenzen für die Reibkraft bilden. Die aperiodischen Pfade konvergieren alle zum gleichen Wert zwischen diesen Limits. Für geringe Last erhalten wir die von Derjaguin generalisierte Form des Reibgesetzes von Amontons-Coulomb, welches auch auf atomarer Ebene gültig zu sein scheint. Wir beobachten auch einen nicht verschwindenden Derjaguin Offset für atomare glatte Metalle in schmiermittelfreiem Kontakt. Berücksichtigen wir unsere Methode zur exakten Berechnung der realen Kontaktfläche bei der Berechnung der Last, erhalten wir bei jedem Druck eine vergleichsweise höhere Last. Dies führt zu einer Streckung der Kurven im exponentiellen Reibgesetz und verringert in Folge die Reibzahlen um 25%–35%.

Contents

Chapter 1

Ab-initio Tribology

Nature isn't classical, dammit, and if you want to make a simulation of nature, you'd better make it quantum mechanical, and by golly it's a wonderful problem, because it doesn't look so easy.

Richard Feynman, "Simulating Physics with Computers", International Journal of Theoretical Physics,volume 21, 1982, p. 467-488, at p. 486 (final words)

1.1 A short and incomplete history of tribology

The word *tribology* was coined in 1966 by Peter Jost in a report of the UK department of education and science [1]. It consists of the greek word $\tau\rho\iota\beta\omega\sigma$ (rubbing) and the suffix $\lambda o\gamma\iota\alpha$ (study of), and is loosely translated to The science of friction, lubrication and wear. A better definition might be given in [2]: The science and technology of interacting surfaces in relative motion and of related subjects and particles. A nearly all-embracing definition that is more suitable to define a branch of research and technology that involves many disciplines of the natural sciences like physics, mechanical engineering, chemistry and metallurgy. In this brief introduction special concern is given to the history and development of theory on dry friction, as the main body of the present work deals with this problem. In the same famous Jost report potential yearly savings in excess of £ 500 million for Britain are given if better tribological practices would be used in industry. A large sum of money even today and more then 1% of the gross domestic product of 1966 Britain. Although the word is quite new, tribology has been studied for centuries and a relief in the tomb of Egyptian Pharaoh Djehutihotep from $\sim$ 1900 B.C. depicts the lubrication, with presumably water, of a sled used to pull a 58 ton statue, thus proving that people practiced tribology nearly 4000 years ago [3]. (Interestingly, the lubrication effect of water on a sled on sand was investigated very recently and explained by the strengthening of

the shear modulus of sand by capillary water bridges between the grains [4]).

In Leonardo da Vinci's (1452–1519) notebooks one finds numerous drawings and sketches concerning tribological experiments and devices including ball bearings and sliding blocks. Leonardo also formulated the first known friction laws in his unpublished notebooks, namely that friction does not depend on the area of contact and that the friction force is doubled when the load is doubled. Both of these laws were rediscovered and published in the late 17th century by Amontons [5] and in the 18th century Coulomb, who, beside clearly distinguishing static and kinetic friction, added a third law, stating that the friction force is also independent of velocity [6]. These are the classical laws of sliding friction, giving relations between the friction force F, the load L, the area of contact A and the sliding velocity v: $F(A) = $ const., $F(v) = $ const. and $F = \mu L$, where the last formula is the famous Amontons-Coulomb law which introduces the arguably most important figure of merit in tribology, the coefficient of friction μ. These laws are still used today and remain valid for a large number of problems and applications. Nevertheless, numerous cases have been thought were other friction laws have to be used, for example in the case of adhesive surfaces where friction does not vanish for zero load and the Amontons-Coulomb law has to be extended by an additive constant, the Derjaguin offset [7].

The perhaps most puzzling observation in the empirical classic friction laws is the independence of the friction force on the contact area, especially for adhesive surfaces. One would expect that a larger area of contact would lead to stronger bonding and therefore increased friction. This mystery was explained satisfactory only in the 20th century by Bowden and Tabor by correctly explaining the difference between the apparent and the real area of contact [8]. Due to microscopic roughness two bodies in contact actually touch only on a few of their protruding asperities even if they appear perfectly flat to the naked eye. This real area of contact is orders of magnitude smaller than the apparent area of contact and is linearly dependent on load, thus providing a theoretical explanation of the Amontons-Coulomb law. Bowden and Tabor are also credited with publishing the first modern tribology book in 1950, The Friction and Lubrication of Solids [9].

The next big step in understanding the fundamental principles of friction was the development of experimental techniques that allowed the study of tribological phenomena on small length scales. These were the surface force apparatus in the seventies by Tabor, Winterton, and Isrealachvili [10, 11], the scanning tunneling microscope (STM) in 1982 by Binnig and Rohrer [12] and most importantly the atomic force microscope (AFM) in 1986 by Binnig , Quate, and Gerber [13]. A modification of the AFM used in contact and constant force mode is also known as the friction force microscope (FFM) [14]. With these instruments it became possible to study tribological phenomena with atomic resolution in

various environments. The FFM tip acts as a single asperity which can be dragged over a surface at various loads and speeds and a multitude of different behaviors have been observed depending on the experimental conditions. Since friction in large scale contacts is a highly complex problem this single asperity studies are very useful to understand the fundamental interactions and dynamics involved in friction, wear, and lubrication problems. The rich field of science that evolved over time on this small length scales is known as nanoscale tribology, atomic-scale friction or simply nanotribology. To interpret the numerous results of FFM experiments computer simulations on the atomic scale became increasingly important [15], from simple fits to spring models [16, 17] and assumed complete energy dissipation [18, 19], over classical molecular dynamics (MD) [20], to first principle studies [21–28].

The field of computational nanotribology has become an important tool in the ongoing quest to solve the most fundamental riddles posed in the complex multiscale and multidisciplinary world of tribology. The present thesis comprises work using *ab-initio* methods on two different fields in computational nanotribology. The first one is dedicated to defining and quantifying the true area of contact between an AFM probe and the surface of a solid while the second one deals with determining friction forces in dry sliding contacts.

1.2   Ab-initio determination of frictional forces

As mentioned in the previous section the introduction of the SFA, the AFM, and the FFM increased the interest in atomistic modelling of frictional forces and other tribological phenomena such as wear and the area of contact. While the primary tool in the workshop of the computational tribologist is undoubtedly the wide field of classical molecular dynamics simulations (classical MD; for a review see for example [20]), more and more publications use first principle methods to describe and predict tribological events on the atomic scale. While models using these techniques are still severely limited in size and simulation time compared to classical MD, the substantial increase in computer power and better scaling of *ab-initio* codes have made realistic problems treatable with parameter free methods. The obvious advantage over classical MD simulations is the avoidance of empirical interaction potentials, which, while often very accurate, tend to be hit-and-miss and should not be trusted without supporting evidence.

The following sections should give a brief and by no means complete overview of contributions in the field of *ab-initio* nanotribology, focusing on the determination of frictional forces in dry contact. The actual method used in most of the presented publications is Density Functional Theory (DFT), which will be discussed in section 1.3.

1.2.1 The model of Zhong and Tománek

In the early 1990's Zhong and Tománek et al. [18] for the first time combined *ab-initio* calculations with the idea of stick-slip motion (see section 1.1 and for example reference 9). They computed the energy surface of a palladium layer sliding on a graphite surface. Movement on this smooth energy surface is conservative, meaning that on closed paths no energy is lost or gained and the average of all forces is zero. (The problem is also evident for open paths if they are long enough as will be discussed in detail in chapter 3). To calculate the frictional forces they devised a model to circumvent the problem of the conservative force field. In their model, it is assumed that, while moving, the palladium gets stuck at each maximum of the potential surface and is only released when the support reaches the next minimum. At this point a slip occurs and all stored energy is completely dissipated (see figure 1.1). Thus, friction is maximized as all force components pointing in the direction of movement are neglected in this model. The average friction force, F, in this approach can be related to the distance, δx, between the minima in the potential and the maximum potential height, ΔE. Care has to be taken, however, while calculating the energy landscape as ΔE might be underestimated as will be shown in section 3.2. Together with the external load L, which can be derived from the interaction energy, there is also a way to define a coefficient of friction μ assuming a Coulomb-Amonton like friction law

$$F = \frac{1}{\Delta x}\Delta E \quad , \quad \mu = \frac{F}{L} = \frac{\Delta E}{L\Delta x} \quad . \tag{1.1}$$

In the original paper this equation predicts a coefficient of friction which rises non linearly with external load, a result not really in accord with classical Coulomb-Amonton behavior but the overall behaviour of the friction versus load curve is comparable to early AFM experiments [29]. In a later paper by the same authors this process was also described for a single palladium atom as a model of an AFM tip as the "maximum friction microscope" [19]. In the same work an alternative and, in the view of Zhong and Tománek, more realistic model of an AFM tip was published which depends on a spring constant and is similar to a Prandtl-Tomlinson model [16, 17]. The calculation of coefficients of friction from equation 1.1 for the "maximum friction microscope" might be rather crude, but it is widely used (see .e.g. [27]).
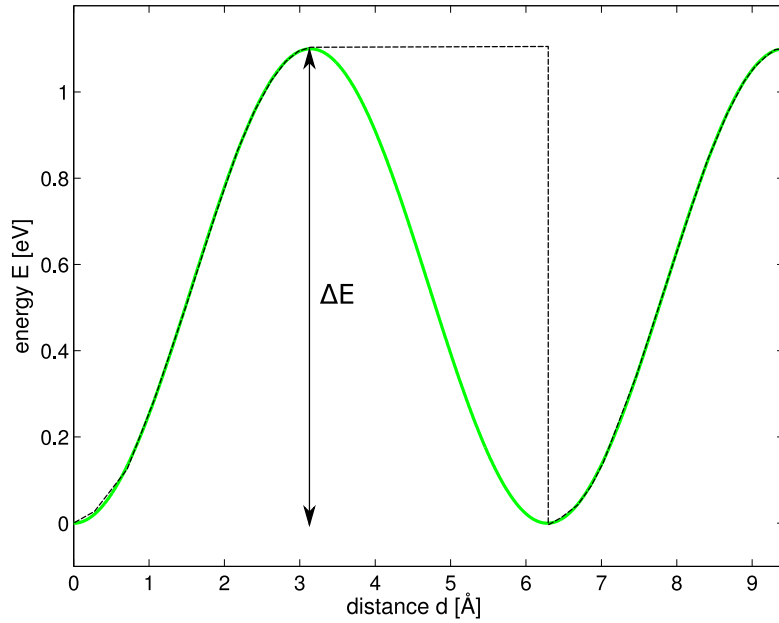
(a) Potential energy surface with maximum height ΔE. The dashed line corresponds to the path of the tip.
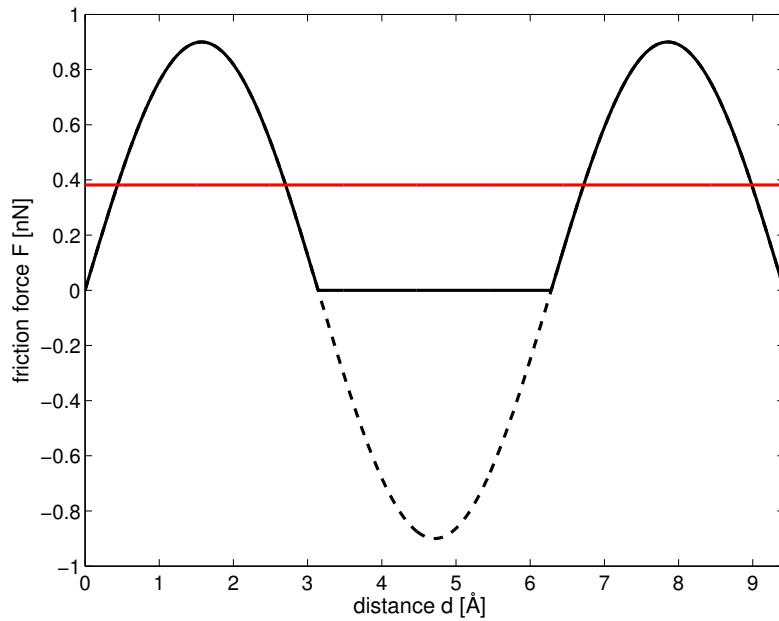
(b) Conservative forces (dashed line) and forces in the Zhong-Tománek model (solid line). The resulting average force is plotted in red.

Figure 1.1: A sketch of the energy and forces in the model of Zhong and Tománek for a "maximum friction microscope" as published in reference 19.

1.2.2 Friction between hydrogenated diamond surfaces and other carbon systems

As diamond-like carbon (DLC) is widely used as a wear resistant solid lubricant (see for example [30]), it is not surprising that a number of atomistic studies have been devoted to the interaction between different diamond surfaces, especially in the hydrogenated form. Two publications shall now be briefly presented here.

In 2001, Neitola and Pakkanen studied the friction between two (111) surfaces of diamond, as this surfaces does not show reconstruction [31]. They modeled the surfaces as two $C_{13}H_{22}$ flakes and carried out the required calculations with the Hartree-Fock method, using the split basis sets 3-21G* and 6-31G* and finding only minor differences between the two. Using the method by Zhong and Tománek discussed above, a linear friction law in accordance with Amonton's formula was obtained and a friction coefficient of 0.22 could be determined.

In contrast to this work, Dag and Çiraci investigated the friction between two diamond (001) surfaces, both clean and hydrogenated within the framework of DFT in 2004 [32]. Unsurprisingly they calculated a strong adhesive force between the bare surfaces which would lead to high friction. The situation changes however if hydrogen is present at the interface and the interaction of the slab becomes strongly repulsive. The estimations for the friction coefficient in the hydrogenated case vary between 0.05 and 0.07 depending on the load, using the method of Zhong and Tománek, while as estimation using lateral forces yields to even lower values of 0.01. All these numbers are one order of magnitude lower than the value calculated by Neitola and Pakkanen, a discrepancy that is not readily explained alone by the different surface planes investigated.

Further studies bei Neitola and Pakkanen involving different hydrocarbons [33], hydrogenated graphite [34], and fluorinated diamond surfaces [35], using both Hartree-Fock and Møller-Plesset perturbation theory of second order (MP2 [36]), always resulted in rather linear friction vs load behavior and friction coefficients between 0.05-0.16 (graphite), 0.15-0.25 (hydrocarbons), and 0.28-0.43 (fluorinated diamond), depending on system size and level of theory.

All this results should illustrate that, while it is difficult to gain consistent results even with *ab-initio* methods, the classical laws of friction are in many cases surprisingly still valid on the nano scale.

1.2.3 Accurate shearing of KCl on iron (001)

A fine example of utilizing *ab-inito* methods to calculate tribological properties is given in a series of papers from 2011 by Garvey, Furlong, Weinert, and Tysoe. They calculate the shear properties of potassium chloride (001) films (KCl) on iron (001) using density functional theory. The shear strength S is an important property of a sliding interface as the lateral force during sliding F is calculated by multiplying it with the real area of contact A_C, $F = SA_C$.

In the first paper two computational methods are compared and it is established that the projector-augmented wave (PAW) method is not able to deal with the quickly changing bonding environment between K and Cl ions and it is necessary to use full-potential linearized augmented plane-waves (FLAPW) to successfully model the sliding interface accurately [21]. The paper also demonstrates that the method is suitable to correctly reproduce the bulk shear moduli of KCl measured in experiments. Sliding is then mimicked by pulling the topmost atomic layer of the 3 layer thick KCl film, that covers the 7 layer thick iron slab on both sides, and allowing all other atomic layers to relax. It is found that the sliding plane is indeed located between the iron and the potassium chloride film and that the KCl slab moves like a rigid body. The shear strength at zero pressure is calculated for the $\langle 10 \rangle$ and $\langle 11 \rangle$ directions and is found to be rather isotropic at $S_{\langle 10 \rangle} = 79.8\,\mathrm{MPa}$ and $S_{\langle 11 \rangle} = 70.3\,\mathrm{MPa}$ and in good agreement with the experimental value of $S_{\langle 10 \rangle} = 65 \pm 5\,\mathrm{MPa}$.

The second paper of this series is concerned with the pressure dependence of the shear strength of the KCl-Fe interface [22]. In contrast to the previous paper the interface was now modeled as a KCl bilayer between two, 7 layer thick, Fe slabs. This arrangement was favored over the previous configuration as iron has a higher Young's modulus than KCl and was found previously to deform less under pressure than KCl. Thus, it was decided to put pressure on the contact by reducing the distance between the outermost iron layers. This approach also assures that both K and Cl ions are able to react to the imposed pressure independently. First, the total energy for the system was recorded for different compressions, which leads to data for different pressures, as the pressure can be calculated from the first derivative of the total energy with respect to the volume. Now the shear strength for each pressure was calculated analogous to the previous paper, leading to both a linear and quadratic term in the dependence of the shear strength S on the pressure P, $S = S_0 + \alpha P + \beta P^2$. As the linear coefficient α was found to be significantly larger than the quadratic coefficient β, the calculated behavior fits reasonable well to the experimental data that suggest an essentially linear pressure dependence of the shear strength. Depending on the sliding direction the calculated values for the shear strength

at zero pressure are $S_0\langle 10\rangle = 64\pm 9\,\mathrm{MPa}$ and $S_0\langle 11\rangle = 69\pm 8\,\mathrm{MPa}$, in excellent agreement with the experimental value of $S_0^{\mathrm{exp}} = 65 \pm 5\,\mathrm{MPa}$. The value for the linear coefficient was found to be equal for both directions and at $\alpha = 0.05 \pm 0.01$, lower, but in the same range as the experiment, which gives $\alpha^{\mathrm{exp}} = 0.14 \pm 0.02$.

In the third paper, Garvey et *al.* examined the impact of film thickness on the shear strength of KCl on Fe [23]. Instead of a two layer thick KCl slab, a 4 layer thick film was considered. Analogous to the previous paper, shear strengths of $S_0\langle 10\rangle = 62 \pm 15\,\mathrm{MPa}$ and $S_0\langle 11\rangle = 65 \pm 11\,\mathrm{MPa}$ at zero pressure where calculated for the 4 layer slab, very similar to the results obtained for the two layer thick film. The α value for both directions was also nearly the same at $\alpha = 0.06 \pm 0.01$. Thus the results are identical within the error limits for both slab sizes and the local bonding between the KCl and the Fe surface seems to play the most important role in the tribological properties of this interface.

1.2.4   Frictional figures of merit for single layered nanostructures

In 2012 Cahangirov et *al.* published their van der Waals corrected DFT calculations on layered honeycomb nano structures [25]. Using the well established Prandtl-Tomlinson model [16, 17] to distinguish between smooth sliding and stick-slip regimes they investigated the possibility of super low friction between layers of graphane (CH), fluorographene (CF), MoS_2, and WO_2.

To this end a 3D grid is constructed and the upper layer is moved in the x, y, and z direction over the lower one, relaxing both structures at any position. The movement in x and y direction is necessary to collect energy and force data for all possible lateral positions while the variation in z is needed to keep the load constant. (A similar method is explained in section 3.4.) The resulting energy landscapes for each specific load can be used to identify the likely friction paths along the valleys and determine the energy barriers needed to be overcome. By comparing the critical stiffness values of the contact k_c and the single layers k_s, that can both be fitted from the *ab-initio* data, the state of sliding can be deduced from the Prandtl-Tomlinson model. For $k_s < k_c$, stick-slip is observed while after the transition at $k_s = k_c$ sliding is continuous for $k_s > k_c$ where the creation of non equilibrium phonons is strongly suppressed and a main channel for energy dissipation is thus closed, leading to very low friction, an effect called superlubricity. The dimensionless fraction of these two stiffness values can be used to identify the sliding regime and is reported as the frictional figure of merit for the sliding material. Indeed the fraction k_s/k_c calculated at usual loading pressures for CH, CF, and MoS_2 are one order of magnitude larger than the critical value 2, while the result for WO_2 is even two orders of magnitude larger for low loads.

In contrast to these materials, calculations on two hydrogenated silicene (SiH) layers sliding against each other were also presented in this publication. There, stick-slip behavior is already observed for very low pressures.

These results, which where also confirmed by direct sliding simulations indicate that WO_2 is an excellent candidate for a solid lubricant especially since the negatively charged oxygen atoms at the surface are immune to oxidation, a process that is likely to hinder superlubric behavior in hydrogenated DLC [32].

1.3 Density functional theory

1.3.1 Introduction

In a 2005 paper [37] Sid Redner analyzed the citation statistics of Physical Review (PR), a group of journals published by the American Physical Society (APS) [38], from 1893 to 2003. Of the eleven papers with more than 1000 citations (only internal citations are counted in this study, meaning citations of PR articles in a PR journal) five are discussing ideas relevant to density functional theory (DFT). The top two are the seminal papers by Kohn & Sham and Hohenberg & Kohn [39, 40], while places 3 and 4 are studies on the self energy correction problem (by Perdew & Zunger [41]) and the correlation energy (Ceperley & Alder [42]) in the local density approximation. Place 11 on this distinguished list deals with efficient Brillouin zone integration, a topic essential in practical implementations of DFT codes. Updating the citation numbers to January 2014 and including citations in non-PR journals using the web of knowledge [43] gives staggering results between 21926 for the Kohn & Sham paper and 8334 for Ceperley & Alder. Another paper by Perdew [44], with Burke and Ernzerhof, detailing a flavor of the generalized gradient approximation to correlation and exchange, has a total citation score of 31404 as of January 2014 [43]. Papers by people developing DFT codes also rack up humongous numbers of citations: for example some papers dealing with the codes VASP [45] at 16670, Gaussian [46] at 7776, WIEN2k [47] at 1793, and ABINIT [48] at 1636.

These vast numbers of citations should help to illustrate the importance density functional theory calculations have in present times. From molecule adsorption to band structure calculations, from magnetic order prediction to simulated AFM images, from calculating photo electron spectra to molecular dynamics calculations, DFT has become a cornerstone in interpreting experimental results and predicting new interesting phenomena. The main advantages of the method, which will be briefly described in subsection 1.3.2, is the high accuracy and large predictive power compared to empirical methods while still retaining a quite moderate computational cost.

1.3.2 Formalism

As mentioned in subsection 1.3.1, Density Functional Theory, or DFT, is widely used in ab-initio calculations. The overview that is given here, is following reference 49. The idea is based on the observation of Hohenberg and Kohn, that the information contained in a many-electron wave function of a given problem is in principle completely represented by the electron density ρ. The Hohenberg-Kohn theorem [40] states now, that the ground state energy is a unique functional of the electronic density $E[\rho]$, which is minimized at the equilibrium density $\rho(\vec{r}) = \rho_0(\vec{r})$. This theorem can be proved in an elegant way (see [50]).

To obtain the functional, which is equal to the expectation value $\langle \Phi | H | \Phi \rangle$, were Φ denotes the many-body wave function, one usually splits it into four parts, expressing the kinetic energy, the ionic nuclear potential, the classical Coulomb electron-electron interaction term and the exchange and correlation term

$$E[\rho] = E_{\text{kin}}[\rho] + E_{\text{ion}}[\rho] + E_{\text{ee}}[\rho] + E_{\text{xc}}[\rho] \quad . \tag{1.2}$$

Now one strives to express these energies in terms of the electron density, which is easily done for the ionic potential and the classical electron-electron term

$$E_{\text{ion}}[\rho] = \int d^3r \, V_{\text{ion}}(\vec{r}) \rho(\vec{r}) \quad , \tag{1.3}$$

$$E_{\text{ee}}[\rho] = \frac{1}{2} \int d^3r' \int d^3r \, \frac{\rho(\vec{r}') \rho(\vec{r})}{|\vec{r} - \vec{r}'|} \quad . \tag{1.4}$$

At this point it is interesting to observe that $E[\rho] - E_{\text{ion}}[\rho]$ is a universal functional, which does only depend on the number of electrons in the system, but not on the ionic potential. This means, that, if the exact expression for E_{xc} could be found (it will be shown that the E_{kin} term does not make any trouble) all materials could be solved by simply adding the adequate potential. Unfortunately, no exact representations for the exchange-correlation term is known so one is forced to use one of several approximations.

To circumvent the difficulties in expressing the kinetic energy through ρ, Kohn and Sham [39] introduced auxiliary single-electron orbitals $\varphi_i(\vec{r})$, which form exactly the same charge density

$$\rho(\vec{r}) = \sum_{i=1}^{N} |\varphi_i(\vec{r})|^2 \quad . \tag{1.5}$$

With the new functions $\varphi_i(\vec{r})$, the kinetic energy now yields

$$E_{\text{kin}} = \sum_i \int d^3r \, \frac{\hbar^2}{2m} (\nabla \varphi_i(\vec{r}))^2 \quad . \tag{1.6}$$

For calculating the energy and density of the ground state, one has to minimize the energy functional $E[\rho]$ with respect to ρ

$$\frac{\delta\{E[\rho] - \mu(\int d^3r\, \rho(\vec{r}) - N)\}}{\delta\rho(\vec{r})} = 0 \quad , \tag{1.7}$$

where the Lagrange parameter μ fixes the number of electrons to N. This equation can now be transformed to minimize with respect to the φ_i instead of ρ, whereupon ε_i ensures the normalization of the functions φ_i

$$\frac{\delta\{E[\rho] - \varepsilon_i(\int d^3r\, |\varphi_i(\vec{r})|^2 - 1)\}}{\delta\varphi_i(\vec{r})} = 0 \quad . \tag{1.8}$$

The result leads to the Kohn-Sham equations [39],

$$\left[-\frac{\hbar^2}{2m_e}\Delta + V_{\text{ion}}(\vec{r}) + \int d^3r'\, \frac{\rho(\vec{r}')}{|\vec{r} - \vec{r}'|} + \frac{\delta E_{\text{xc}}[\rho]}{\delta\rho(\vec{r})} \right] \varphi_i(\vec{r}) = \varepsilon_i\varphi_i(\vec{r}) \quad , \tag{1.9}$$

which are Schrödinger equations of single electrons moving in an effective (single-particle) potential $V_{\text{eff}} = V_{\text{ion}} + V_{\text{ee}}[\rho] + V_{\text{xc}}[\rho]$,

$$V_{\text{eff}}(\vec{r}) = V_{\text{ion}}(\vec{r}) + \int d^3r'\, \frac{\rho(\vec{r}')}{|\vec{r} - \vec{r}'|} + \frac{\delta E_{\text{xc}}[\rho]}{\rho(\vec{r})} \quad . \tag{1.10}$$

The Kohn-Sham potential and the charge density could now be calculated selfconsistently, were it not for the unknown term E_{xc}. How approximations are found for the exchange and correlations will be shown in the next section.

1.3.3 LDA and GGA

The various Local Density Approximation (LDA) models are obtained by evaluating the correlation and exchange energy of the homogeneous electron gas at the local density of the non-homogeneous system. This is a good approximation for systems with a slowly varying charge density, which is true for s- and p-states, but should not work well for d- and f-electrons

$$\epsilon_{\text{xc}}^{\text{LDA}}[\rho(\vec{r})] := \epsilon_{\text{xc}}^{\text{hom}}(\rho_0)|_{\rho_0 \to \rho(\vec{r})} \quad . \tag{1.11}$$

For spin-polarized calculations, one usually speaks of LSDA (Local Spin Density Approximation) and the prescription is carried out for $\rho_+(\vec{r})$ and $\rho_-(\vec{r})$. (Also frequently the parameterization $\rho(\vec{r}) = \rho_+(\vec{r}) + \rho_-(\vec{r})$ and $\zeta(\vec{r}) = \frac{1}{\rho(\vec{r})}(\rho_+(\vec{r}) - \rho_-(\vec{r}))$ is used.) For reasons of simplicity, these distinction shall not be made in this section, although some calculations in the present work are spin-polarized.

The ground state of a homogeneous electron gas in a uniform background of positive charge (the jellium model) can be solved with the Hartree–Fock approximation using

plane waves. This yields an exchange term of fundamental constants, where V denotes the Volume, N the number of electrons and k_F the Fermi wavevector. (The solution for jellium, which yields the famous dependence of ϵ_x^{LDA} on $\rho_0^{\frac{4}{3}}$, can, for instance, be found in [51])

$$\epsilon_x^{\text{LDA}}(\rho_0) = -\frac{N}{V}\frac{3}{4}\frac{e^2 k_F}{\pi} = -\frac{3}{4}\left(\frac{3}{\pi}\right)^{\frac{1}{3}} e^2 \rho_0^{\frac{4}{3}} = -C_x\,\rho_0^{\frac{4}{3}} \quad . \tag{1.12}$$

This result is the exchange energy per unit volume. The correlation contribution ϵ_c^{LDA} of the jellium density ρ_0 can be obtained e.g. from advanced many-body techniques like Quantum Monte Carlo. The approximated functional is now obtained by integrating $\epsilon_{\text{xc}}^{\text{LDA}} = \epsilon_x^{\text{LDA}} + \epsilon_c^{\text{LDA}}$

$$E_{\text{xc}}[\rho] \stackrel{LDA}{\approx} \int d^3r\,\epsilon_{\text{xc}}^{\text{LDA}}(\rho_0 = \rho(\vec{r})) \quad . \tag{1.13}$$

This can now be inserted into equation (1.9), which then can be solved selfconsistently.

Surprisingly LDA does not only work well in the slowly varying limit of the charge density, but also gives quite acceptable results for many other systems. Gunnarsson et al. showed [52], that the exchange-correlation hole modeled by LDA does not have to be an exact replica of the true hole, but that it is sufficient to provide a reasonable approximation of the spherical average of the real exchange correlation hole and fulfill the sum rules. Other reasons for the surprising success of LDA as well as a detailed account of parameterizations can be found in [53].

The freedom to modify the exchange-correlation term however, has provoked a large amount of effort, culminating in the Generalized Gradient Approximations (GGA). The concept states that it should be possible to improve the functional by adding derivative terms. The resulting functional still does not take non-local contributions into account, but by adding the gradients of the density one obtains a semilocal exchange-correlation term

$$E_{\text{xc}}^{\text{GGA}}[\rho, \nabla\rho] = \int d^3r\,\epsilon_{\text{xc}}^{\text{GGA}}\left(\rho(\vec{r}), |\nabla\rho(\vec{r})|\right) \quad . \tag{1.14}$$

In general, GGA, in comparison to LDA, tends to improve total energies and atomization energies[54]. It also softens bonds to correct [55] or overcorrect [56] LDA and generally favors density inhomogeneity more than LDA does. There is no standard functional, but PW91 [57] by Perdew et al. and PBE [58] by Perdew, Burke and Ernzerhof, which was also utilized for the present work, are very commonly used. (There is also no standard functional for LDA, but in that case variations in the parametrizations are much smaller.)

1.3.4 Treating van der Waals forces in DFT

Quite naturally the local and semilocal functionals discussed in 1.3.3 are not suited to describe systems with sizable long range interactions, not only because they are "short sighted", but also because they do not take instantaneous fluctuations of the density into account. However, there are a multitude of problems that can profit from treatment with DFT where such long range interactions play a significant role. Most prominent are the cases where an important part of the interaction is formed by Van der Waals (vdW) forces, which are named after Johannes Diderik van der Waals who was the first scientist to describe intermolecular forces in 1873 [59]. This includes the attraction between nobel gas atoms, physisorption of molecules on surfaces, physics of large molecules in general, tip-substrate interactions and some crystalline solid state systems, for example the famous case of graphite [60–62]. Although they are generally week compared to forces in chemical bonds vdW forces play a role in these systems due to their long range nature and collective effect.

Arising from non-local electron correlations, vdW forces are usually divided into three contributions: *a*) forces between two permanent dipoles, ensemble averaged over different orientations (Keesom forces); *b*) forces between a permanent and an induced dipole (Debye forces) and *c*) forces between a quantum-induced spontaneous dipole and an induced dipole (London dispersion forces), together showing decay with distance in the form of r^{-6} [63].

Several methods have been proposed over the last years to incorporate dispersion forces into DFT calculations. (Please consult the recent paper by Klimeš and Michaelides for an overview and the references therein for detailed description of those methods [64].) A simple workaround to some major problems, e.g. the vanishing binding of graphite layers when treated with popular GGA functionals, is to use LDA, which gives usually better agreement to the experimental binding situation. However, as LDA is a local approximation and is therefore unable to capture long range correlation, this better agreement is obtained for the wrong physical reasons and can be attributed to the incorrect decay of the Kohn-Sham potential at the surface [65, 66]. Several methods have been proposed that include additive pairwise long range interactions capturing important physics without the use of external parameters. Examples include the VV10 [67], the local response dispersion (LRD) approach [68, 69], and the van der Waals density functional (vdW-DF) [70]. The random phase approximation [71–74] combined with the adiabatic connection and fluctuation dissipation theorem [75, 76] goes beyond this pairwise models, explicitly calculates polarizabilities, and intrinsically includes long range correlation effects. It is a very capable method to calculate vdW contributions although the enormous computa-

tional costs limit the approach to very small systems and benchmark calculations. Due to accurate results, implementation in popular codes, and moderate computational cost the optimized versions of Dions vdW-DF functional by Klimeš and co-workers are among the most widely used methods to treat systems in DFT where relevant vdW contributions are to be expected [66, 77]. The optB86b van der Waals functional is one of these optimized versions and combines a re-parametrized Becke86 exchange term [78] with local LDA correlation and a non-local correlation part for the vdW interaction

$$E_{\text{xc}}^{\text{optB86b-vdW}}\left[\rho\right] = E_{\text{optB86b(x)}}\left[\rho\right] + E_{\text{LDA(c)}}\left[\rho\right] + E_{\text{nl(c)}}\left[\rho\right] \quad . \qquad (1.15)$$

The non-local part of the correlation is constructed by double integrating over the whole space using an interaction kernel $\varphi\left(r_1, r_2\right)$ that captures the correct $O\left(1/|r_1 - r_2|^6\right)$ asymptotic behavior

$$E_{\text{nl(c)}} = \iint \mathrm{d}r_1 \mathrm{d}r_2 \, \rho\left(r_1\right) \, \varphi\left(r_1, r_2\right) \, \rho\left(r_2\right) \quad . \qquad (1.16)$$

It has been successfully used to describe graphene and noble gases on metals [79–81] and is therefore our choice to describe a tungsten AFM tip in contact with graphene on iridium in chapter 2.

1.3.5   VASP

The actual DFT code used to calculate all results in this thesis is the Vienna Ab-initio Simulation Package (VASP) [45, 82–84]. The term *ab-initio* indicates that the calculation is from the ground up, using as only input the type of lattice and the atomic species, but otherwise no empirical data. VASP uses a plane wave basis set, periodic boundary conditions and can be operated with either ultrasoft pseudopotentials (US-PP [85, 86]) or the projector-augmented wave method (PAW [87, 88]). Several approximations to the correlation and exchange energy are selectable, including for example LDA and several GGAs (see subsection 1.3.3), Hartree-Fock type calculations [89], hybrid functionals [90, 91], Green's function methods [92–95], functionals to approximate vdW interactions (see subsection 1.3.4 and RPA-ACFD calculations [74, 96, 97]). Forces and the full stress tensor can be calculated with VASP which can then be used to relax atoms into their ground-state.

Chapter 2

Calculating the real contact area on the nanoscale

An original idea. That can't be too hard. The library must be full of them.

Stephen Fry, "The Liar", (1991)

2.1 Introduction

Historically the introduction of the concept of a real area of contact in 1939, which is substantially smaller then the apparent area of contact, was a huge step forward in understanding the laws of friction[8]. Since then a multitude of methods have been used to predict the pressure dependent real area of contact for asperities of different configuration.

In 1881 Hertz laid the foundations of contact mechanics by describing the junctions between non-adhesive, homogeneous elastic solids of simple shape [98]. Nearly a hundred years later Johnson, Kendall, and Roberts (JKR) included short ranged adhesion forces inside the contact in their analysis, leading to larger contact areas compared to the Hertz model [99]. In contrast to this approach Derjaguin, Muller and Toropov (DMT) assumed that the Hertzian contact area remains undeformed but included long range adhesion forces acting outside the contact [100]. Tabor was able to show that both the JKR and the DMT model can be viewed as limiting cases of a more general model, with JKR suitable for soft materials with large adhesion and DMT for hard materials with low adhesion [101]. Further work on this unification was done by Maugis using Dugdale potentials [102]. The analytical solution by Maugis, however, produces rather cumbersome equations, which can be approximated with high accuracy by the generalized transition equation derived by Carpick, Ogletree and Salmeron [103]. This result also describes the transition between the DMT and the JKR models, but the simpler formulas can be used more easily to fit

experimental data and only differs to the Maugis-Dugdale model in the unstable low load region. Generally these theories, while differing in the particular size of the contacts, agree that the contact area between a single sphere and a flat surface is proportional to the load to a power of $\frac{2}{3}$. In the case of two nominally flat surfaces in contact works by Archard, Greenwood and Williamson, Bush, and Persson indicate that the real area of contact is directly proportional to the load [104–108].

These continuum mechanics models are undoubtedly very successful and play an important role in theoretical and experimental work in the field of tribology. On the nanoscale, however, for example in AFM experiments, the size of the the contact approaches the size of the involved atoms. It is doubtful that models based on continuum mechanics are applicable on this length scale as the involved materials are clearly discretized. Although the Maugis-Dugdale model is widely used to interpret AFM experiments, atomistic methods are of great value in checking the results and provide a much needed tool to increase the understanding of the real area of contact [20]. In recent studies and discussions a need for characterizing the area of contact on an atom-by-atom basis was expressed and various strategies to estimate the number of atoms in contact were proposed [109–112]. However, it is not trivial to decide at which distance two atoms are in contact or how big the resulting contact area should be. One possibility is to define a certain inter-atomic distance d_0 below which contact should be established, however, this just shifts the problem to find the correct distance d_0. A common method is to identify d_0, and thus the onset of contact, as the beginning of repulsion between the two observed atoms [111, 113]. To this end, classical molecular dynamics (MD) studies using Lennard-Jones potentials are often employed, sometimes without the attracting part if the surfaces of interest should be non-adhesive. In our view, this method is not ideal for describing the onset of contact on the nanoscale for the following reasons: (i) if only repulsive interaction is a sign of contact, the atoms in a solid or molecule at $0\,\mathrm{K}$ are not in contact with each other. (ii) in AFM experiments one often observes a "jump to contact", where either the tip, or some part of the surface or both jump towards each other because of strong attractive interactions. If now the tip support is lowered further, the distance between the surface and the tip apex might get even smaller as the chemical binding becomes stronger. It seems unreasonable to argue that the tip is not in contact with the surface after the jump, just because the interaction is still attractive.

In a widely cited study form 2009 Mo, Turner, and Szlufarska examined the area of contact between hydrogenated amorphous carbon tips of up to $30\,\mathrm{nm}$ radius and a flat hydrogenated diamond surface [110]. For this large scale finite temperature ($300\,\mathrm{K}$) molecular dynamics study they used a reactive empirical bond-order (REBO) potential [114] to model the chemical forces and added an analytical switching function to include vdW-like

long range forces. In the class of force field approaches in classical MD, REBO potentials are considered an accurate choice and although the modeling of vdW forces is rather crude compared to some *ab-initio* approaches (see section 1.3.4), even considering vdW interactions was a unusual step for this kind of large scale simulations. The multi-asperity picture of nanoscale contact presented in the publication relies on the assumption that contact is established between atoms that are interacting chemically through the REBO potential while a much larger part of the tip is attracted to the surface via the vdW forces. Now an area A_{at} is attributed to every chemically interacting atom of the tip leading to the total real contact area $A_{\mathrm{real}} = N_{\mathrm{at}} A_{\mathrm{at}}$, using the number of involved atoms N_{at}. Due to atomic scale roughness of the amorphous tip this real contact area may be significantly smaller than the expected area of contact of the single asperity, A_{asp}, which is defined in their paper by the envelope over the contact points. Summed up, Mo, Turner, and Szlufarska showed how important atomic corrugations are for an accurate evaluation of the real area of contact, underlining the need of accurate computational models. However, a few points remain to be analyzed further. In a realistic, continuous potential it might be hard to distinguish between long range dispersion forces and chemical forces, thus making it difficult to define the number of atoms in contact. There is also no load dependent method presented to obtain the single atomic contact area A_{at}, which is assumed to be an average over all single contacts and is calculated by dividing the surface of the hydrogenated diamond by the total number of hydrogen atoms covering it.

In the following sections we will describe an *ab-initio* way to calculate the distance dependent real contact area of a tungsten tip on a graphene substrate (see section 2.4) as well as on a fcc(111) copper surface (see section 2.5). We employ van der Waals corrected density functional calculations (see section 1.3) and use Bader-partitioning of the charge density to identify accurate atomic volumes and surfaces in different chemical surroundings (see section 2.2).

2.2   Quantum Theory of Atoms in Molecules

In the 1960s Richard F. W. Bader and coworkers started the development of the Quantum Theory of Atoms in Molecules (QTAIM), see [115] and references therein. After Lewis focused the attention of the chemical community on the concept of bonds in 1916, this concept renewed the interest in the idea of atoms as building blocks defined as mononuclear regions of real space inside a molecule or a solid [116]. A quantum mechanical system is defined by the state function Ψ and every observable is described by an operator acting on this state function. If a system is now separable in building blocks in real space, these should be defined by Ψ as well and quantum mechanics should provide a complete

description of each subsystem, as it does for the whole system. Using an extension of Schwinger's principle of stationary action allows to rigorously proof that a meaningful partitioning of real space in such subsystems is possible and unique [115, 117]. The necessary and sufficient condition that needs to be fulfilled to define the boundaries of specific atoms in a molecule is formulated using the basic quantity in DFT, the charge density ρ and is given in [118], as

$$\nabla\rho(\mathbf{r}) \cdot \mathbf{n}(\mathbf{r}) = 0 \quad \forall \mathbf{r} \in S(\mathbf{r}) \quad . \tag{2.1}$$

Here S is the boundary surface of the atom, ρ is the electronic charge density and $\mathbf{n}(\mathbf{r})$ is the unit vector normal to the surface. The condition states that the flux of the gradient field of the charge density, $\nabla\rho$, through the surface S has to vanish. S is therefore called a zero flux surface. This definition of atoms is additive in the sense that all averaged observables of the whole system $\langle\hat{A}\rangle$ are sums of the contributions by the included atoms Ω

$$\langle\hat{A}\rangle = \sum_\Omega A(\Omega) \quad , \tag{2.2}$$

a result which can be seen as an important foundation of chemistry [115]. It also can be shown that principles which are valid for the whole system, e.g. the virial and the Ehrenfest theorems, also hold for the subsystems defined by equation 2.1.

A cornerstone of the theory are the descriptions of critical points in the charge density where $\nabla\rho = 0$, characterized by rank σ and signature λ in the form (σ, λ). In three dimensions σ is fixed to 3, whereas the sum of the eigenvalues of the Hessian matrix of ρ determines the sign and value of λ. For example the charge density has maxima only at the positions of the nuclei, where the curvature in all three dimensions is negative and we find (3,-3) critical points. Bonded atoms are joined by a line called a bond path that maximizes charge compared to neighboring lines and a (3,-1) critical point is encountered between the atoms. Here the charge density is at a maximum perpendicular to the bond path and at a minimum in the direction of the bond. This is then called a bond critical point. Lines of $\nabla\rho$ always start and end at critical points. The main attractors are the nuclei and around each nucleus lies a basin of charge which is bordered by a zero flux surface and whose gradient lines terminate at the (3,-3) critical point. These basins are the atoms.

Of course charge density gradient lines may also start at infinity, because although the charge density decays exponentially with distance, it theoretically is non-zero everywhere. The gradient lines originating from infinity terminate almost exclusively at the nuclei positions of surface atoms. This means that atoms at the surface of a solid or at the borders of a molecule theoretically have infinite volume. In practice some arbitrary (but

small) cutoff density (ρ_{cut}) is used to disregard all regions in which the charge density is smaller than the selected cutoff. In figures 2.1 the Bader volume of a single carbon atom in an ethanol molecule is plotted for different density cutoffs. In figure 2.2 we see the Bader volume for three rather large cutoffs of a titanium atom in a infinite hexagonal closed packed titanium crystal. Here a small cutoff is far less important, as the bonding environment ensures that the volumes converge very quickly with the decrease of the cutoff density. (In the case of hcp titanium at about 0.02 electrons per Å^3.)

(a) $\rho_{\mathrm{cut}} = 0.01\,\mathrm{e}/\text{Å}^3$ (b) $\rho_{\mathrm{cut}} = 0.001\,\mathrm{e}/\text{Å}^3$ (c) $\rho_{\mathrm{cut}} = 0.0001\,\mathrm{e}/\text{Å}^3$
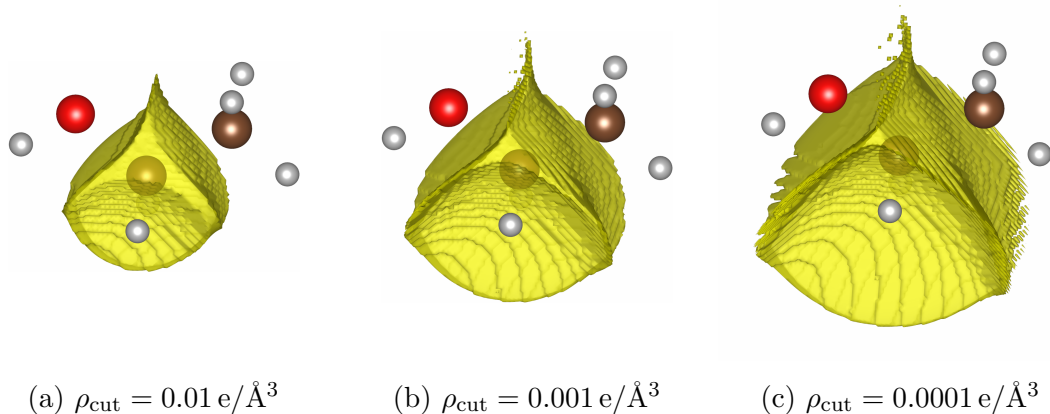
Figure 2.1: Bader volume (yellow) of one carbon atom in a ethanol molecule for different density cutoffs of a) 0.01, b) 0.001, and c) 0.0001 electrons per Å^3. Carbon atoms are brown, oxygen is red and hydrogen grey. This figure was created using the VESTA program [119].

On a technical level the QTAIM integrates seamlessly with DFT as the basic variable for the zero flux condition is the charge density ρ which is also the central quantity in DFT. The actual Bader analysis in this work was performed with the code developed by Henkelman, Sanville, and Tang which is compatible with VASP (see section 1.3.5) output files [120–122]. The standard cutoff density in this code is 10^{-3} electrons per Å^3 but can be varied arbitrarily or turned off entirely. Care must be taken to use a fine enough fast Fourier transformation grid in the VASP calculation on which the partitioning takes place to converge to the total number of electrons. A complete account of the QTAIM including the necessary background can be found in reference [123].

2.3   General model

If one seeks to define the real area of contact on an atomic scale, it is quite natural to think about the size, shape, and deformations of the involved atoms. Once the size and

(a) $\rho_{cut} = 0.03 \, e/\text{Å}^3$ (b) $\rho_{cut} = 0.02 \, e/\text{Å}^3$ (c) $\rho_{cut} = 0.01 \, e/\text{Å}^3$
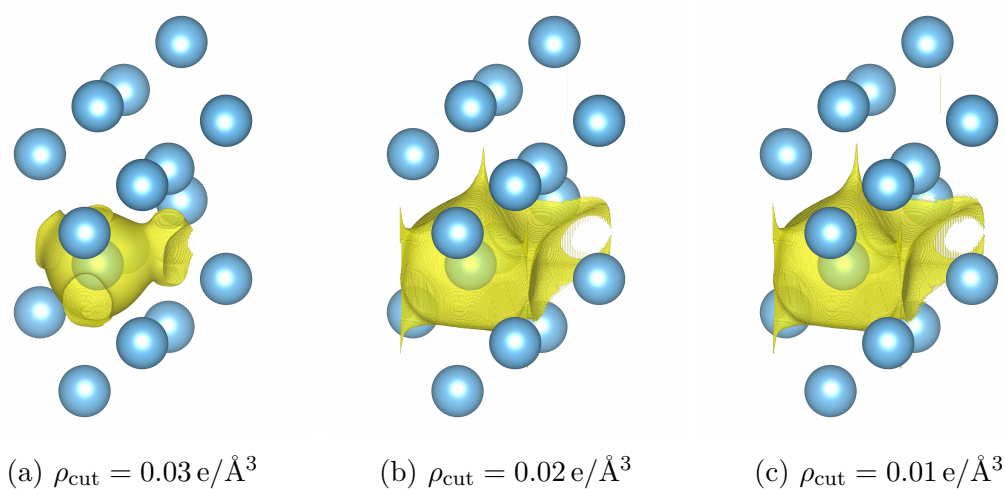
Figure 2.2: The Bader volume (yellow) of a single titanium atom in a hexagonal close packed crystal for density cutoffs of a) 0.03, b) 0.02, and c) 0.01 electrons per Å^3. This figure was created using the VESTA program [119].

shape of all atoms in the contact region are determined, the calculation of the real contact area is reduced to a simple summation of the regions that are actually in contact, provided one can distinguish unambiguously between the two contacting bodies and can attribute each atom to one of them.

The division of molecules into single atoms has long been an interesting and widely studied problem in chemistry and numerous methods have been proposed to solve it. Mullikan's projector approach from 1955, using atomic centered wave functions, is still widely used for example [124–127]. After Bader began the development of his QTAIM theory in the sixties (see section 2.2), Hirshfeld developed a different and also highly successful partitioning scheme in 1977 which does not feature sharp borders between atoms but rather distributes the density at each point among all atoms in the system [128]. Some ambiguities in this approach, mainly the dependence of the resulting charges on the initially chosen promolecular density, the comparably very small atomic charges, the connection to information entropy, and problems in dealing with charged molecules, have been addressed by Bultinck, Van Alsenoy, Ayers, and Carbó-Dorca, by constructing an iterative version of the method [129]. Other approaches which feature overlapping atoms include for example the Voronoi approach by Baerends and coworkers [130, 131], the fuzzy atoms method of Mayer and Salvador [132], or Becke's approach [133].

It is important to notice at this point that the concept of atoms in molecules, while highly useful, is not an objective property of a given system as a matter of principle, as single atoms are not directly observable in molecules [134]. This means that none of the

methods mentioned above is superior to the others, as multiple versions are consistent with chemical measurements and there are no ways to measure enough of a single atoms properties in a molecule to define it unambiguously. Thus one has to choose carefully between the various possible definitions and methods depending on the specific reason for the partitioning and the system in question. In their paper "What Is an Atom in a Molecule?" [134], Parr, Ayers, and Nalewajski describe the concept as a perfect example of a *noumenon* in the Kantian sense, meaning a purely rational and non-empirical concept or idea, or, an object of purely intellectual intuition. Kant uses the word nearly synonymously with the "thing-in-itself", the unknown and unobservable transcendental object which is unaffected by the limitations of our perception [135].

It is quite evident, however, that for the purpose of the calculation of an accurate real area of contact, a diffuse partitioning with overlapping atoms is far from ideal. We therefore chose the QTAIM, or Bader partitioning scheme, which provides an elegant way to calculate the shape and size of all atoms in the contact zone. Our model was developed with tapered AFM tips in mind, but we believe that it can be quite naturally used also for other geometries, as long as the system is within the limitations set by the calculation providing the charge density ρ.

2.3.1   Choosing a cutoff

As discussed before, ρ formally is non-zero everywhere, the Bader atoms at the surfaces of the contacting bodies extend into the vacuum region to infinity or until they reach another atom. Thus, without some cutoff being used, contact between two bodies is established at all distances, which is a clearly unphysical result. This density cutoff ρ_{cut} cannot be chosen arbitrarily, as the size of the contact at all separations depends crucially on it. The problem of choosing the correct cutoff density ρ_{cut} is equivalent to the problem of defining the beginning of contact. If the point of contact is defined correctly it is easy to tune ρ_{cut} accordingly, so that the Bader partitioning results in non vanishing contact only for distances smaller than that particular separation. As mentioned in section 2.1, Mo, Turner, and Szlufarska defined atoms to be in contact if they came close enough to each other to chemically interact [110]. However, as long range interactions are included implicitly in the approximation to the exchange-correlation potential that we use (see section Computational Methods), the separation into a long and a short range part is not straightforward. It might also be difficult to unambiguously define the distance when close range interaction starts even if accurate interaction data are available. For example figure 2.3 shows data collected by calculating the total energy of a tungsten tip and moiré graphene on iridium with a GGA functional.
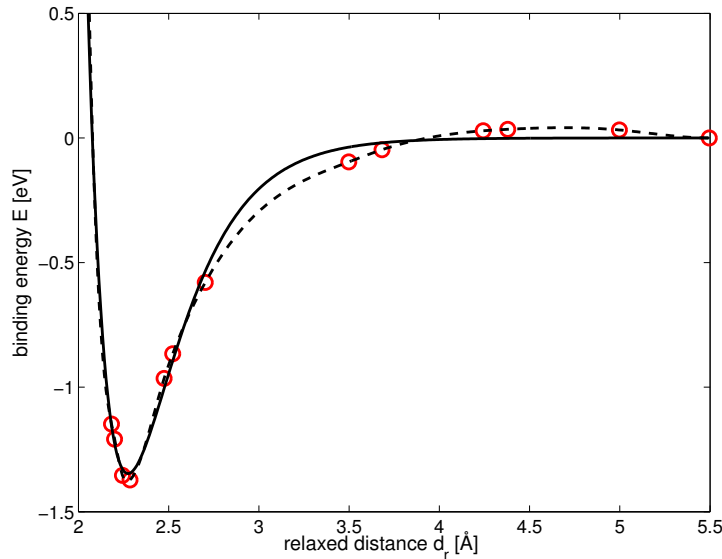
Figure 2.3: Total GGA energy (red circles) versus distance of a ten atom tungsten tip and moiré graphene on iridium. The solid line is a fit of the data with a Morse function, the dashed line is a cubic spline interpolation.

The geometries were optimized using the optB86 functional including long range van der Waals contributions (see section 1.3.3). More information about the system and the computational methods can be found in section 2.4, but it is important to notice that figure 2.3 corresponds roughly to the close range potential between two contacting bodies. To define a point where this potential becomes attractive seems to be a rather arbitrary choice and could be for example either the point of inflexion or some threshold value, e.g. the point where the potential reaches 5% of it total depth. Moreover, once this choice is made, there might still be some ambiguity concerning the fitting function that is used to describe the potential, as can be seen in the differences between the spline and the physically more relevant Morse fit [136] in figure 2.3.

A more unambiguous way to define the onset of contact is to analyze the relaxations that happen if the tip is lowered towards the surface. We distinguish the distance for the static, unrelaxed system (d_s) and the relaxed distance (d_r), which are both measured between the tip apex atom and the carbon atom directly under it. For large distances no relaxations will take place, although there might be attraction due to vdW forces and d_r will be equal to d_s. At some point during the approach of the tip stronger forces will cause relaxations, which will result either in a "snap" or "jump" to contact (a phenomenon often observed in AFM experiments) if the interaction is attractive, or in a depression of the surface layer if the interaction is purely repulsive. A sketch of this process is given in figure 2.4. In any case, the d_r versus d_s curve will have a discontinuity at some distinct

22

distance where the system begins to strongly interact. Below this distance the system will try to hold the ideal distance between tip and surface. It is straightforward to identify this discontinuity as the onset of contact.
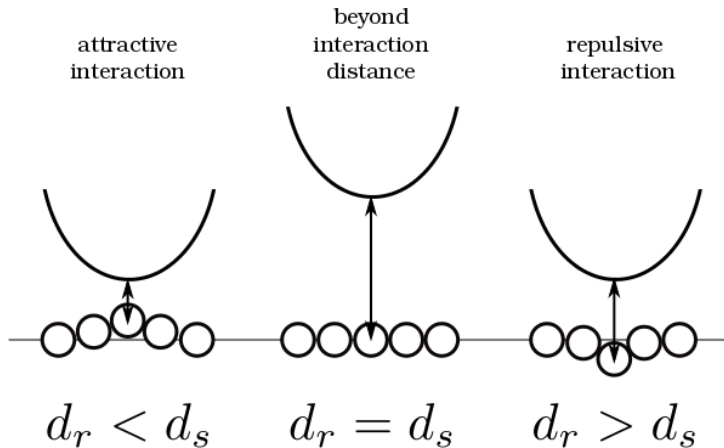
Figure 2.4: Sketch of possible tip-surface interactions. If the tip is far away from the surface (middle panel), relaxing the system will not have an effect on the distance between the tip and the surface. If the tip gets closer, the surface will interact with the tip and will either jump towards the tip if the interaction is attractive (left panel) or will get depressed if the interaction is repulsive (right panel). This instability can be used to define the onset of contact.

In the graphene (Gr) on Ir(111) system mentioned before and described in detail in section 2.4, the interaction between the tip and the surface is attractive at the onset of contact and a jump to contact occurs between $d_s = 3.65\,\text{Å}$ and $d_s = 3.53\,\text{Å}$ (see figure 2.5a). Here d_r is reduced from $3.5\,\text{Å}$ to $2.7\,\text{Å}$, while most of the movement is done by the surface, which jumps upwards to meet the tip (see figure 2.5b). This means that when the tip support is lowered by only $0.12\,\text{Å}$, the distance between the tip apex and the surface is reduced by $0.8\,\text{Å}$. This allows us to define the onset of contact at $d_s \simeq 3.6\,\text{Å}$ and to tune the value of the density cutoff ρ_{cut} accordingly.

After the jump to contact d_r is a linear function of d_s,

$$d_r = \kappa d_s + \delta \quad , \tag{2.3}$$

with $\kappa = 0.23$ and $\delta = 1.48\,\text{Å}$ (see the solid black line in figure 2.5a). The graphene layer that buckled up at the jump to contact is pushed down again and the region under the tip is finally compressed substantially below its equilibrium position (see figure 2.5b). The closest recorded static position, $d_s = 1.30\,\text{Å}$, leads to a relaxed distance of $d_r = 2.18\,\text{Å}$.

As we have now defined at with distance contact is established it is now possible to tune the density cutoff to an appropriate value, so that the resulting Bader atoms begin
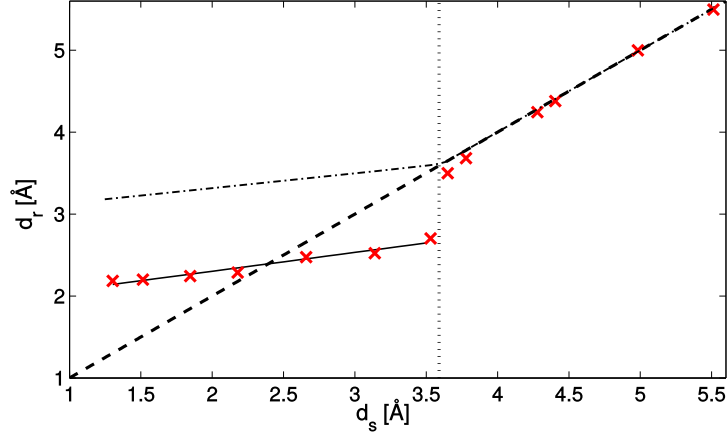
(a)
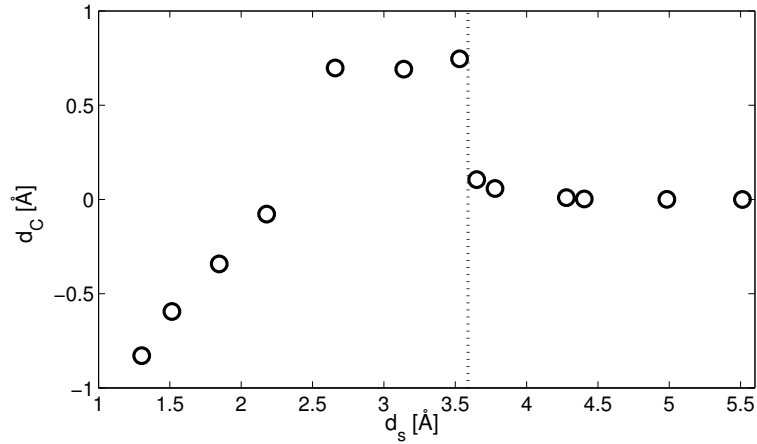
(b)

Figure 2.5: (a) Plot of the relaxed distance d_r (red crosses) versus the static distance d_s of the tungsten tip on the Gr/Ir(111) surface. The dashed line gives $d_r = d_s$. Attractive interactions cause a jump to contact between $d_s = 3.65\,\text{Å}$ and $d_s = 3.53\,\text{Å}$, which is marked with a vertical dotted line. A hypothetical curve for a purely repulsive interaction is sketched by the dashed-dotted line. After the jump to contact the relation between d_r and d_s is also linear (solid black line). (b) Displacement d_C of the carbon atom situated directly below the tip apex, with respect to its static position, versus static distance d_s. The jump to contact is again marked by a vertical dotted line.

to touch at the relevant distance. While this procedure is a little cumbersome initially, as the correct distance of the jump to contact has to be found and several cutoff densities have to be examined, the resulting cutoff parameter can be reliably used for any geometry of the studied materials.

2.3.2   Calculating the area of contact

Once the appropriate density cutoff, ρ_{cut}, is selected the determination of the real area of contact for each distance is rather simple. First the grid based Bader code by Henkelman, Sanville, and Tang [120–122] is used to sum up the Bader volumes of both contacting bodies separately. (Presently there is no possibility of printing out the zero flux surfaces directly, only Bader volumes are supported.) The program generates output in the same format as the input files, so in the case of VASP the output is generated in CHGCAR form (for more information about VASP files please consult the online guide on VASP [137]). In these files the charge density is written on a 3D grid which spans the whole simulation cell. A FORTRAN 95 code was developed to compare the two files and print out the Cartesian coordinates of each point at which one of the files has a non-zero entry and the other file has a non-zero entry at a neighboring grid point. This procedure generates a point cloud with corresponds to the true area of contact between the quantum mechanically calculated Bader atoms. The area of contact can now be simply obtained by triangulation of the point cloud.

2.4   Tungsten tip over moiré graphene on iridium

2.4.1   Introduction

To proof the feasibility of the method we choose a realistic and rather complex system that has previously been used to explain contrast inversion between constant current scanning tunneling microscope and constant frequency AFM images of graphene moiré on metals [138, 139]. The unit cell consists of 4 layers of a 9×9 iridium(111) substrate covered by a 10×10 graphene layer forming a moiré structure in an average distance of $3.42\,\text{Å}$ with a corrugation of $0.35\,\text{Å}$. The lattice constants calculated with the optB86b vdW functional, $a_{\mathrm{Ir}} = 2.735\,\text{Å}$ and $a_{\mathrm{Gr}} = 2.465\,\text{Å}$ are close to the experimental values of $2.71\,\text{Å}$ and $2.46\,\text{Å}$, respectively. This leads to a small mismatch for the non-rotated structure of $10a_{\mathrm{Gr}} - 9a_{\mathrm{Ir}} = 0.015\,\text{Å}$ [139]. The tungsten AFM tip was modeled as a ten atom pyramid with one atom at the apex, four in the next layer and five at the top. The only adsorption site considered was a on-top position in a top-hcp region of the moiré

structure. This means that the tip apex atom is positioned above over a carbon atom in a region where each carbon atom is either directly over an iridium atom or over an iridium hcp position. The 534 atom unit cell is shown in figure 2.6. To keep the computation time manageable and to control the distance between the tip apex and the graphene sheet relaxations were limited to the graphene layer and the bottom five atoms of the tip, holding the iridium substrate and the top of the tip rigid.

(a) View along a axis

(b) View between a and b axis

(c) View along the negative c axis
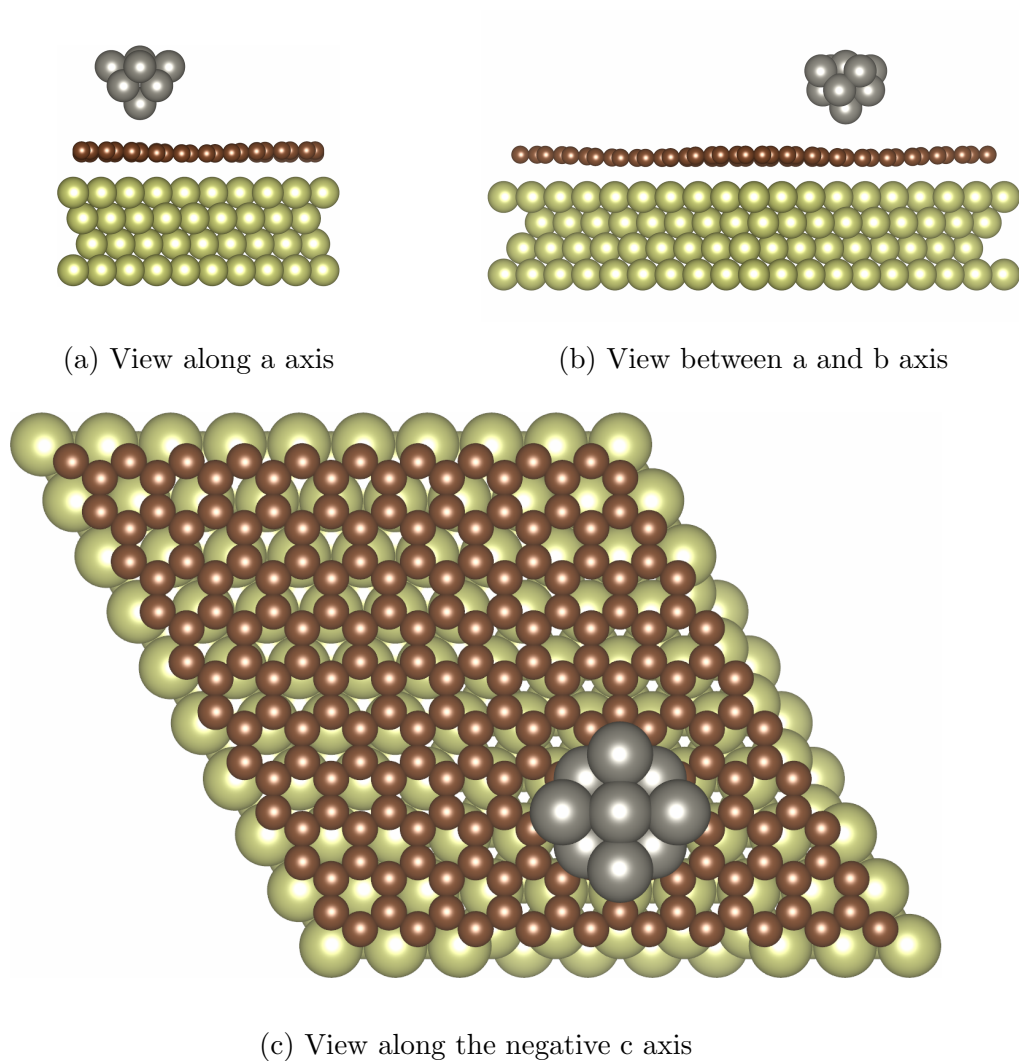
Figure 2.6: Two side (a) and (b), and one top view (c) of the unit cell consisting of a tungsten tip and graphene/Ir(111). Iridium atoms are shown in ligth green, carbon is brown and tungsten grey. All atoms are depicted as space filling spheres. This figure was created using the VESTA program [119].

26

2.4.2 Computational methods

All calculations were performed with the Vienna Ab-Initio Simulation Package *VASP* [45, 82–84] using the Projector Augmented Wave (PAW) method [87, 140]. To include van der Waals (vdW) forces, which are relevant in this system, the optB86b-vdW functional was employed [66, 77]. This functional was used to obtain all parameters in the system unless they are specified as GGA results in which case the long range correlation part was excluded from the calculations. However, energies obtained with the GGA functional where still calculated at the vdW relaxed positions. The Brillouin zone sampling is performed on a Γ-centered $3 \times 3 \times 1$ k-grid, with a smearing of $0.1\,\text{eV}$ using the first order method of Methfessel and Paxton [141]. To ensure good accuracy for the Bader partitioning scheme, the resolution of the second (finer) fast Fourier transform grid on which the charge density is written was doubled for each direction compared to the default values for this cell. This led to a quite dense mesh of $432 \times 432 \times 448$ points. Electronic steps were converged to $10^{-6}\,\text{eV}$ and forces were relaxed to $0.01\,\text{eV/Å}$ during the ionic relaxations. A plane wave cutoff of $300\,\text{eV}$, which is the minimum recommended value for carbon, but larger then the proposed maximum values for iridium an tungsten, was chosen due to the large system size. These system parameters follow the work presented in Andreas Garhofer's PhD thesis who also provided us with a significant amount of the structural data [139]. Detailed information about the computational methods employed can be found in section 1.3.

2.4.3 Results

Energetics

The chosen system exhibits medium adhesion with comparably large long range vdW contributions to the total energy as can be seen in figure 2.7. Using the optB86b vdW functional (see section 1.3.4) the binding energy is about $2.25\,\text{eV}$ per moiré unit cell, of which about $1\,\text{eV}$ can be attributed to the vdW forces.

Upon careful examination figures 2.3 and 2.7 show that the GGA energy is not perfectly converging to zero for long distances d_r, but becomes positive in between $d_r = 4$ and $d_r = 5$. We attribute this fact to the imperfect decoupling of our cell in the c direction (the direction of movement for the tip), as the top of the tip is only about $7.5\,\text{Å}$ away from the repeated iridium slab in the $d_r = 5.5$ position. However, as the effect is small and completely irrelevant for the contact area, the unit cell is very large anyway, we disregard this interaction as a repetition of the study with a larger cell would have severely strained our computational resources. Also several relaxed positions were already available in the
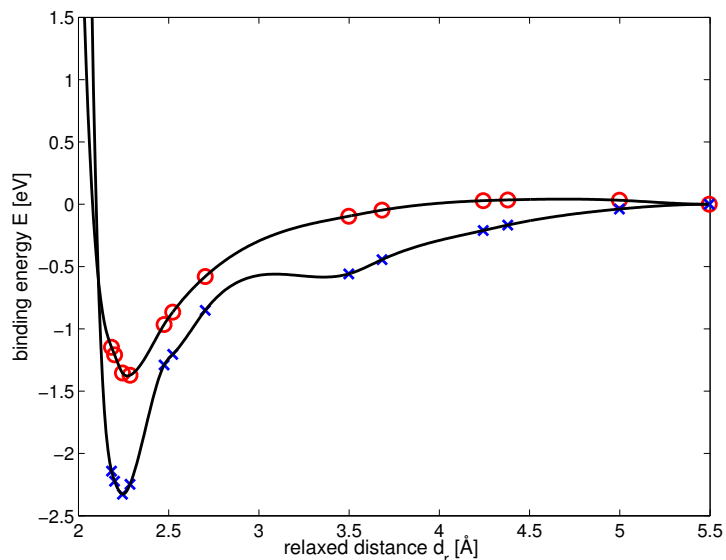
Figure 2.7: Total energy versus distance for relaxed configurations of the tungsten tip on graphene/Ir(111) system. Blue crosses are results obtained with the optB86b vdW functional, red circles are calculated with the modified Becke86 GGA method at the vdW relaxed positions. Black lines are cubic spline fits to guide the eye. The results are normalized to zero for the largest distance.

present unit cell from the studies by Garhofer.

Geometry

The approach of the tip to the surface is depicted in the panels of figure 2.8. The jump to contact occurs between $d_s = 3.65\,\text{Å}$ and $d_s = 3.53\,\text{Å}$, as already shown in figure 2.5. As was to be expected for the stiff tungsten tip, contact is formed predominantly by buckling of the graphene layer. Compared to the rigid case, the apex atom of the tip only moves down by about $0.03\,\text{Å}$, while the carbon atom underneath is jumping up nearly $0.8\,\text{Å}$, (see figure 2.8c).

After the contact is established, further lowering of the tip reduces the buckling, as the graphene layer can relax back to its equilibrium moiré structure (see figures 2.8d and 2.8e). Close to a static distance $d_s = 2.18\,\text{Å}$, the graphene has relaxed almost completely, $d_r \simeq d_s$, and the system is in its minimum energy configuration (see figure 2.7). Upon further lowering of the tip, the graphene buckles now in the opposite direction, towards the iridium substrate, with the relaxed distance d_r still being greater than $2\,\text{Å}$, as seen in figure 2.8f.

28

(a) $d_s = 5.51$ Å   (b) $d_s = 3.65$ Å   (c) $d_s = 3.53$ Å

(d) $d_s = 3.14$ Å   (e) $d_s = 2.18$ Å   (f) $d_s = 1.51$ Å
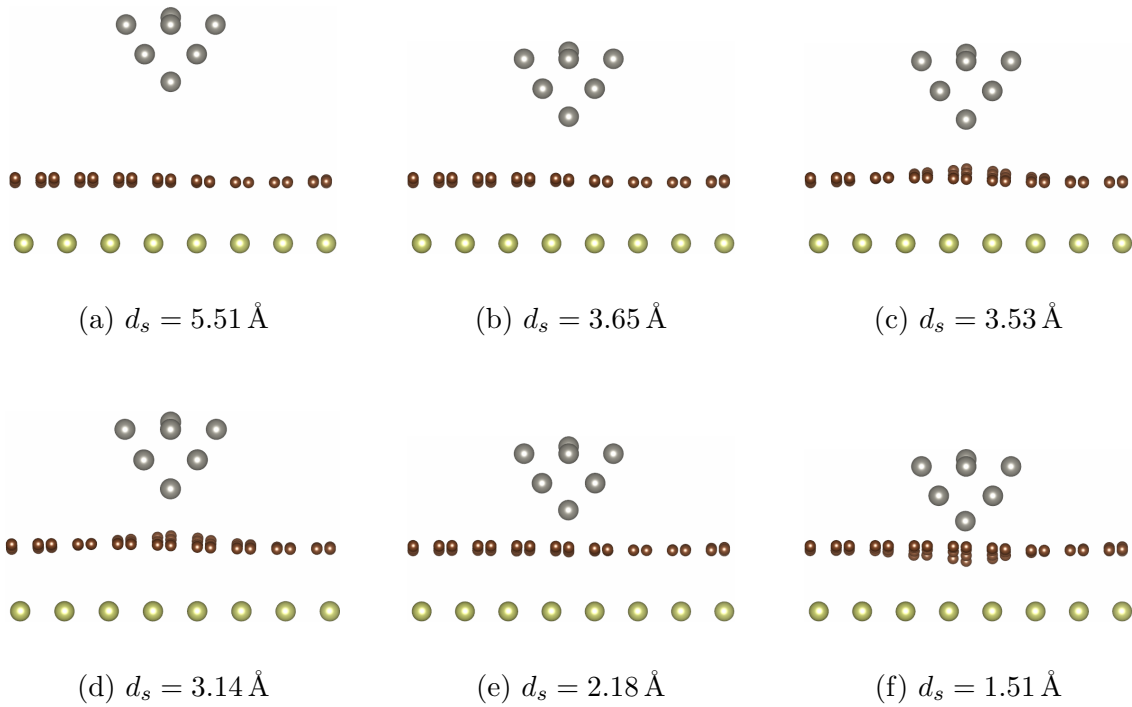
Figure 2.8: (a) – (f), approach of the tungsten tip towards the graphene/Ir(111) surface. The structures have been relaxed using the optB86 vdW functional, but the distances correspond to the static situation before relaxation. The jump to contact occurs between (b) and (c) or 3.65 and 3.53 Å. Iridium atoms are shown in light green, carbon is brown and tungsten grey. This figure was created using the VESTA program [119].

Electronic density cutoff

As mentioned in section 2.3, we can only calculate a meaningful contact area if we select a density cutoff ρ_{cut} for the Bader partitioning in our system as otherwise the opposing bodies would be in complete contact for all distances. As we have already established the desired point of contact (there should be no contact before, and contact after the snap described in section 2.4.3), we now have to find a specific value for ρ_{cut} that is consistent with these data. Figure 2.9 shows calculated contact areas for cutoff densities as low as 10^{-3} electrons (e) /Å^3 (the default cutoff in the applied partitioning code) to the large cutoff of 10^{-1} e/Å^3. Surprisingly, the contact area appears to rise linearly with decreasing distance for all values of ρ_{cut}. This behavior, however, is only observed if one plots A versus d_s, the distance between the static tip to the undisturbed graphene surface, and there only for low values of ρ_{cut}. The relaxed distance d_r is different from d_s after the snap to contact (see figure 2.5a) but the two are connected by a linear relation (see equation 2.3). The two highest cutoff densities (10^{-1} e/Å^3 and 5×10^{-2} e/Å^3) alone show the desired effect of established contact only for $d_s < 3.5$, while the default $\rho_{\text{cut}} = 10^{-3}$ e/Å^3 is giving sizable contact areas for all distances.

Naturally, a very high ρ_{cut} has to be avoided, as the number of electrons that are "lost" into the vacuum region is increasing with rising cutoff. This means that we want to select a value that is high enough to guarantee that the contact area A is only non-zero after the snap to contact has occurred, but is otherwise as low as possible. Figure 2.10 is zooming in to the relevant region, both in distance d_s and cutoff, compared to figure 2.9, but the cutoff density of 5×10^{-2} e/Å^3 is still the best solution to the problem.

As the ideal cutoff of 5×10^{-2} e/Å^3 is 50 times larger then the default value it is important to check if it is still a reasonable number and does not give any unphysical results. In table 2.1 the nominal number of electrons that are assigned to the vacuum region and are therefore not part of any Bader-atom N_e is shown for the density cutoff values of figure 2.9. For the default ρ_{cut} of 1×10^{-3} e/Å^3 only about half of an electron is lost to vacuum. For the cutoff value needed for the calculation of the contact area, 5×10^{-2} e/Å^3, this number is increased to nearly 30 electrons. Although this value seems very large, one has to consider the total system size, which includes $N_{\text{tot}} = 3776$ electrons. Thus, the relative number of "missing" electrons is below 0.8%. Also shown in table 2.1 are the calculated Bader radii R_B of a single tungsten atom and a single carbon atom in a box. The value of 2.9 Å obtained for $\rho_{\text{cut}} = 5 \times 10^{-2}$ e/Å^3 is more than twice as large as the empirical atomic radius of tungsten, 1.35 Å [142], and about 1 Å larger than the previously calculated atomic radius of 1.93 Å [143]. Previously reported values for the atomic radius of carbon reach from the calculated value of 0.67 Å [143], over the empirical
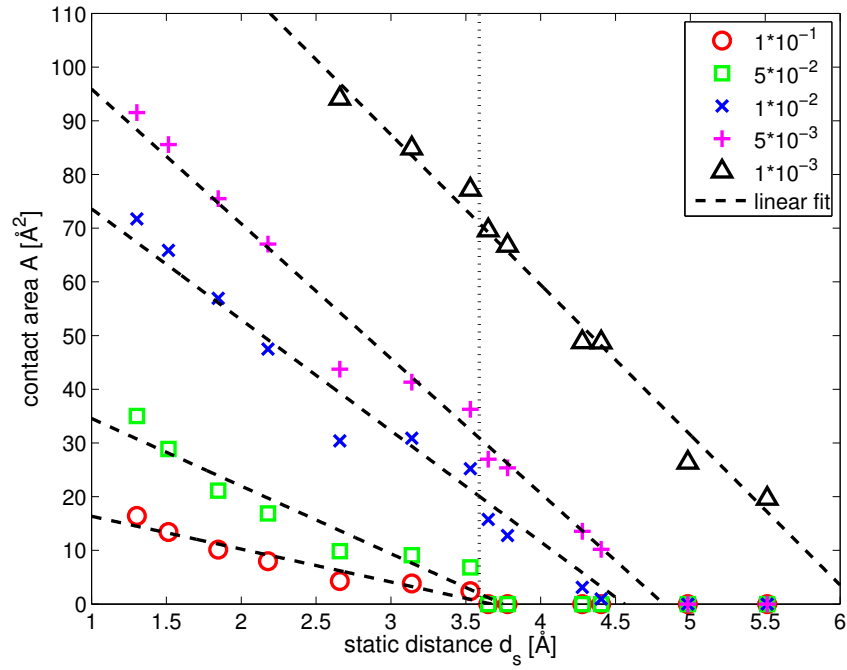
Figure 2.9: Real contact area A of the relaxed system versus the distance of the static tip to the undisturbed graphene surface d_s for several density cutoffs. For each cutoff, the linear fit comprises all positive data points down to the first zero value. The vertical dotted line marks the jump to contact. For the two highest cutoff values the linear fit is a rather bad approximation to the data.
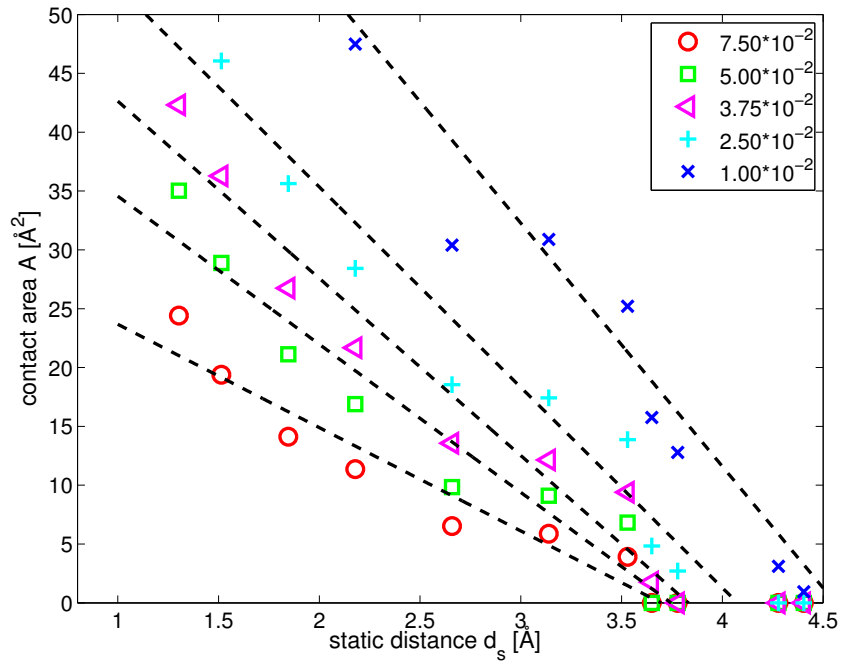
Figure 2.10: Real contact area A of the relaxed system versus the distance of the tip support to the undisturbed graphene surface d_s for several density cutoffs. For each cutoff, the linear fit comprises all positive data points down to the first zero value. Compared to figure 2.9, this plot is zooming in on the relevant region for the jump of contact both in distance d_s and cutoff density. In this region the linear fits give only a crude picture of the true behavior of $A(d_s)$.

ρ_{cut} [e/Å^3]	1×10^{-1}	5×10^{-2}	1×10^{-2}	5×10^{-3}	1×10^{-3}
N_e/N_{tot} [%]	2.03	0.79	0.12	0.06	0.01
N_e	76.51	29.87	4.66	2.46	0.52
$R_B(W)$ [Å]	2.5	2.9	4.1	4.7	6.2
$R_B(C)$ [Å]	1.8	2.3	3.3	3.7	4.8

Table 2.1: Number of electrons N_e assigned to the vacuum region depending on the chosen density cutoff value, both in absolute numbers and in a percentage of the total number of electrons. The radius of a single (spherical) tungsten Bader-atom $R_B(W)$, and a single (spherical) carbon Bader-atom $R_B(C)$, in a large box dependent on ρ_{cut}.

value of 0.70 Å [142] to a van der Waals radius of 1.70 Å [144]. As for tungsten, also the carbon Bader-atom radius for a cutoff density of 5×10^{-2} e/Å^3 is larger than all these reported values at 2.30 Å. This ensures that neither the tip atoms not the surface atoms are artificially small. It also shows that it is wrong to assume that contact between two bodies is established only after the surface atoms overlap if one uses spherical atoms and traditional radii.

It is worthwhile to compare our approach to the onset of contact with the method by Mo, Turner, and Szlufarska, which uses the beginning of short range interaction as a criterion for contact [110]. As already mentioned in section 2.3, the distinction between long range and short range forces is non trivial. We approximate the short range interaction of our system by using a semilocal GGA functional to treat exchange and correlation, however, to analyze these data thoroughly we need a continuous curve, which leaves several fitting options. To illustrate this dilemma we plot figure 2.3 again but add a dotted horizontal line to highlight the point of the jump to contact (see figure 2.11). While the spline interpolation arguably predicts an earlier onset of attractive interactions (at the jump to contact already more than 6% of the total potential depth is reached) the more physically relevant Morse fit gives better results. The interaction strength at the jump to contact is 2.5% of the total potential depth which could be classified as the "beginning of the interaction". This means that our method, at least for this system, is in accordance with the approach of reference 110, but, in our point of view, less ambiguous.

The contact area

As seen in figure 2.9, the true contact area rises linear with decreasing distance d_s of the tip support to the unrelaxed graphene/Ir(111) surface low density cutoffs, but behaves
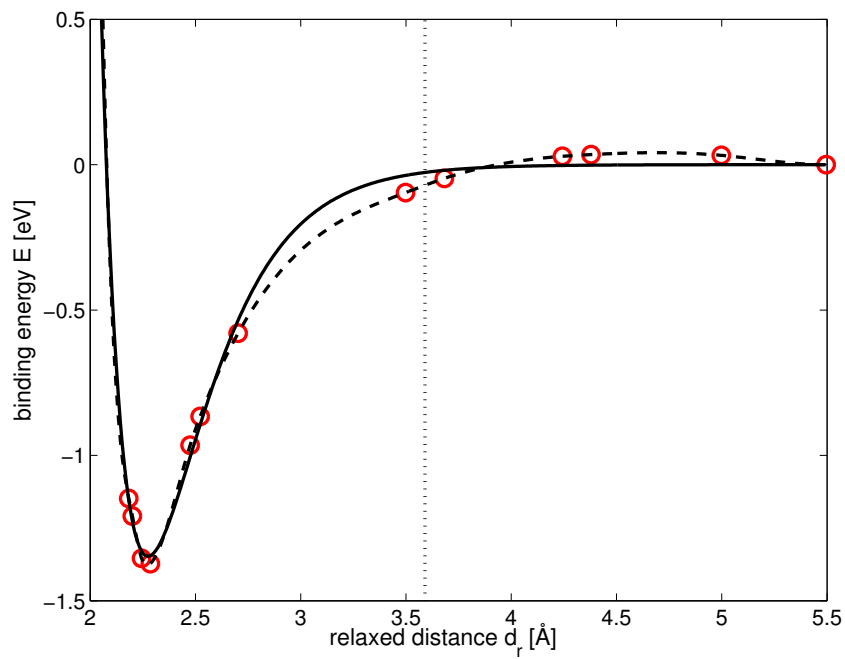
Figure 2.11: Total GGA energy (red circles) versus distance of a ten atom tungsten tip and moiré graphene on iridium. The solid line is a fit of the data with a Morse function, the dashed line is a cubic spline interpolation. The dotted line marks the jump to contact as in figure 2.5.

differently for the optimal value of $\rho_{\text{cut}} = 5 \times 10^{-2} \, \text{e}/\text{Å}^3$ (see also figure 2.10). Plotting A versus d_r leads to a very steep increase of contact area with decreasing distance, as d_r is varying much less than d_s in the contact regime as the system tries to keep the most stable binding distance of about $2.3 \, \text{Å}$ (see figure 2.12).
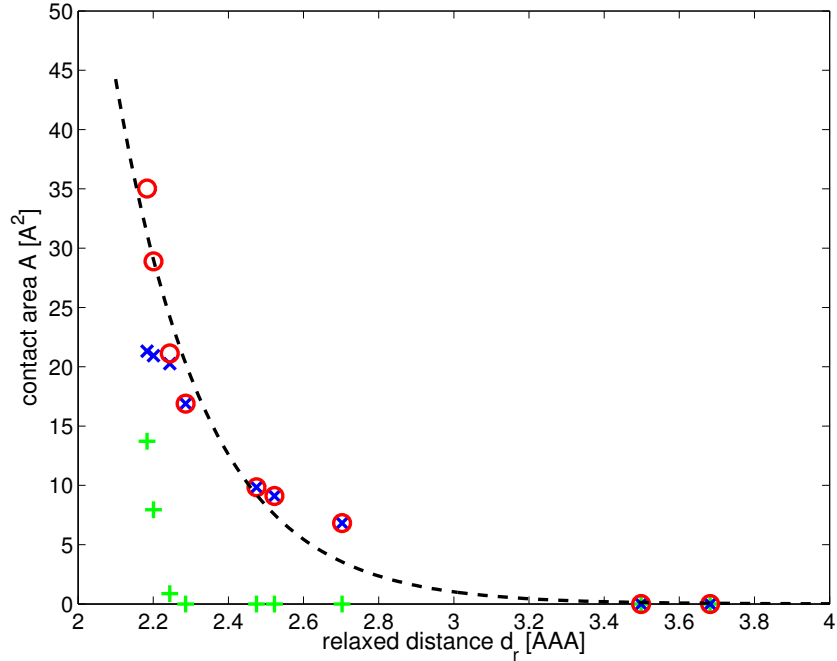
Figure 2.12: Real contact area A versus relaxed distance d_r for a tungsten tip lowered onto a graphene/Ir(111) surface. Blue crosses give the contribution of the apex atom of the tip and green plus signs show the contribution of the second tip layer (four atoms). The total contact area (red circles) is given by the sum of these 2 contributions and can be fitted by an exponential (dashed line).

Figure 2.12 also gives a decomposition of the contact area into contributions of the tip apex (one atom) and contributions from the second layer (four atoms). It is interesting that the second layer only contributes to the total contact area for the three closest distances but is responsible for nearly a third of the area in the two closest configurations. The dashed line in figure 2.12 is an exponential fit to the 7 non-zero data points (red circles) of the form

$$A(d_r) = A_0 \exp(-\lambda_r (d_r - \Delta_r)) \quad , \tag{2.4}$$

with the coefficients $\lambda_r \simeq 4.2 \, \text{Å}^{-1}$ and $\Delta_r \simeq 3.0 \, \text{Å}$. The factor $A_0 = 1 \, \text{Å}^2$ is included for dimensional reasons and has not been used as a fitting parameter. While the fit is not perfect, the agreement with the data is certainly reasonable, especially considering that only two free parameters where used. Also the point of vanishing contact is predicted

well, although only points with finite contact area where used in the fitting process. As there is a linear relation between d_r and d_s in the region where contact is established (see solid black line in figure 2.5a and equation 2.3), it is also possible to express the contact area A through the static distance d_s, which is easier accessible in experiments through the vertical displacement of the tip support, using equations 2.3 ad 2.4. As a linear coordinate transformation does not change the general form of an exponential law, it is obvious why the linear fits in figures 2.9 and 2.10 do not reproduce the data well for low density cutoffs. In the relation $A(d_s) = A_0 \exp(-\lambda_s(d_s - \Delta_s))$, the decay constant is smaller than in $A(d_r)$ with $\lambda_s = \lambda_r \kappa \simeq 1.0\,\text{Å}^{-1}$, while $\Delta_s = (\Delta_r - \delta)/\kappa \simeq 5.0\,\text{Å}$ is increased compared to Δ_r. $A_0 = 1\,\text{Å}^2$ is the same dimensionality factor as before.

Figure 2.13 shows the geometrical shape of the true contact area in top view for four distances that have a non-zero contact area. The different colors denote different depths, ranging from $\sim 0.3\,\text{Å}$ in figure 2.13a to $\sim 1.4\,\text{Å}$ in figure 2.13d. Initially, for larger distances, the shape is rather flat and is dominated by the threefold symmetry of the graphene layer (2.13a and 2.13b). As the graphene layer gets depressed towards the iridium substrate, the contact area is beginning to show a pronounced bowl shape (2.13c), which increases in depth for decreased distance (2.13d). Note that for the closest distance (2.13d, $d_s = 1.30\,\text{Å}$) not only the threefold symmetry of the graphene layer is visible in the center, but the edges of the bowl have the fourfold symmetry of the second tip layer.

The shapes of the contact area plotted in figure 2.13 are also shown in figure 2.14, including the tip, the graphene layer, and the first layer of the iridium substrate.

We can also analyze how many carbon atoms are in contact with the tip for each distance and compare the contact area predicted by our model with the results from the model by Mo, Turner, and Szlufarska [110]. To this end we count every surface Bader atom that touches our tip as contacting, an approach different from that described in reference 110, since we have no pairwise forces at our disposal. In our case, with a cross section of the unit cell $A_C \sim 262\,\text{Å}^2$, and 200 carbon atoms in the graphene layer the contribution per atom is $A_{\text{at}} = A_C/200 = 1.31\,\text{Å}^2$. Each carbon atom has 3 nearest neighbors in $d_{\text{nn}} = 1.42\,\text{Å}$, 6 next nearest neighbors in $d_{\text{nnn}} = 2.46\,\text{Å}$, 3 third nearest neighbors in $d_{\text{tnn}} = 2.84\,\text{Å}$, and 6 fourth nearest neighbors in $d_{\text{fnn}} = 3.76\,\text{Å}$ distance. Already directly after the jump to contact at $d_s = 3.53\,\text{Å}$, more than one carbon atom is in contact with the tip, although the majority of the contact is formed by the central atom which is responsible for $5.90\,\text{Å}^2$ of the total $6.82\,\text{Å}^2$. This is about 30% more than the contact area predicted by the model in reference 110, with $4A_{\text{at}} = 5.25\,\text{Å}^2$. The area contributed by the central atom alone exceeds the value of $4A_{\text{at}}$ by $\sim 12\%$. The next nearest and third nearest neighbors begin to play a role at $d_s = 2.18\,\text{Å}$, contributing to about 7% of the total area $16.89\,\text{Å}^2$. Here the method by Mo,

(a) $d_s = 3.53\,\text{Å}$

(b) $d_s = 3.14\,\text{Å}$

(c) $d_s = 2.18\,\text{Å}$

(d) $d_s = 1.30\,\text{Å}$
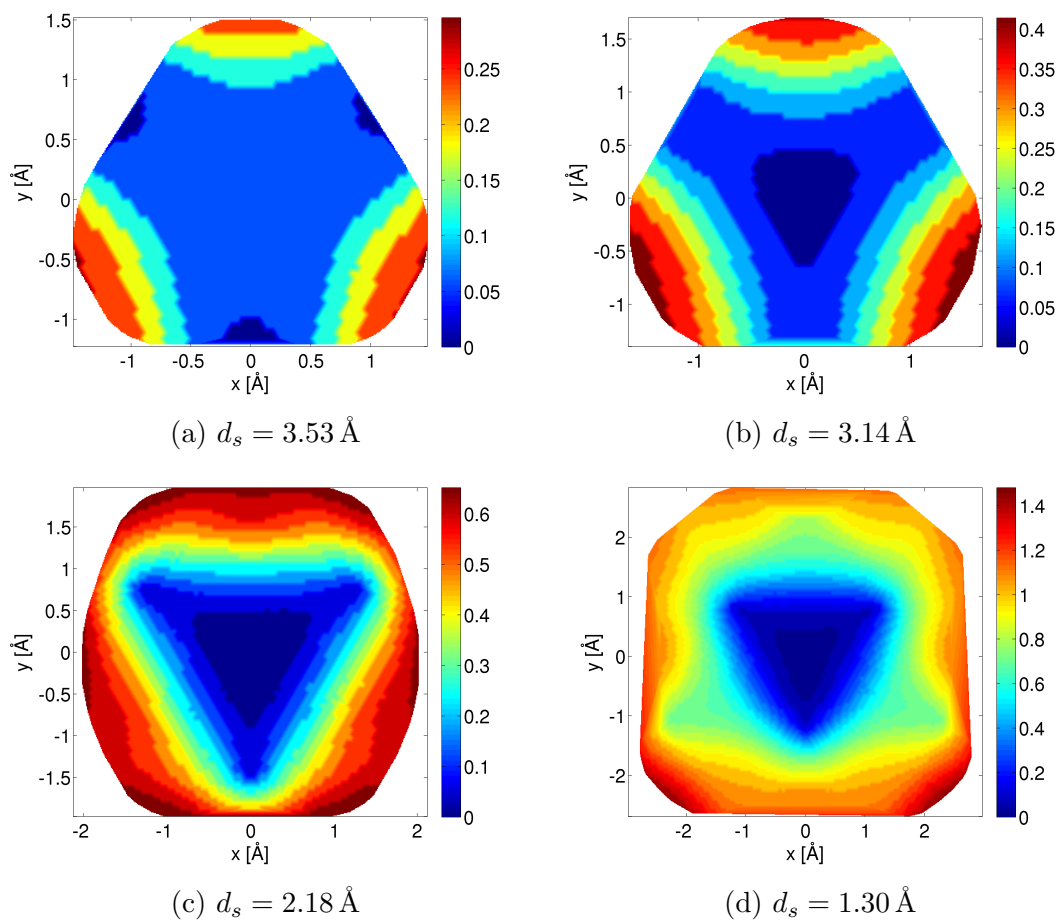
Figure 2.13: Top view of the contact formed by lowering a tungsten tip onto a graphene/Ir(111) surface. The contact area increases from (a) $6.8\,\text{Å}^2$, over (b) $9.1\,\text{Å}^2$, and (c) $16.9\,\text{Å}^2$, to (d) $35.0\,\text{Å}^2$. Different heights are coded by color. Please note the different color bars and axes scaling in each panel.

(a) $d_s = 3.53\,\text{Å}$

(b) $d_s = 3.14\,\text{Å}$

(c) $d_s = 2.18\,\text{Å}$

(d) $d_s = 1.51\,\text{Å}$
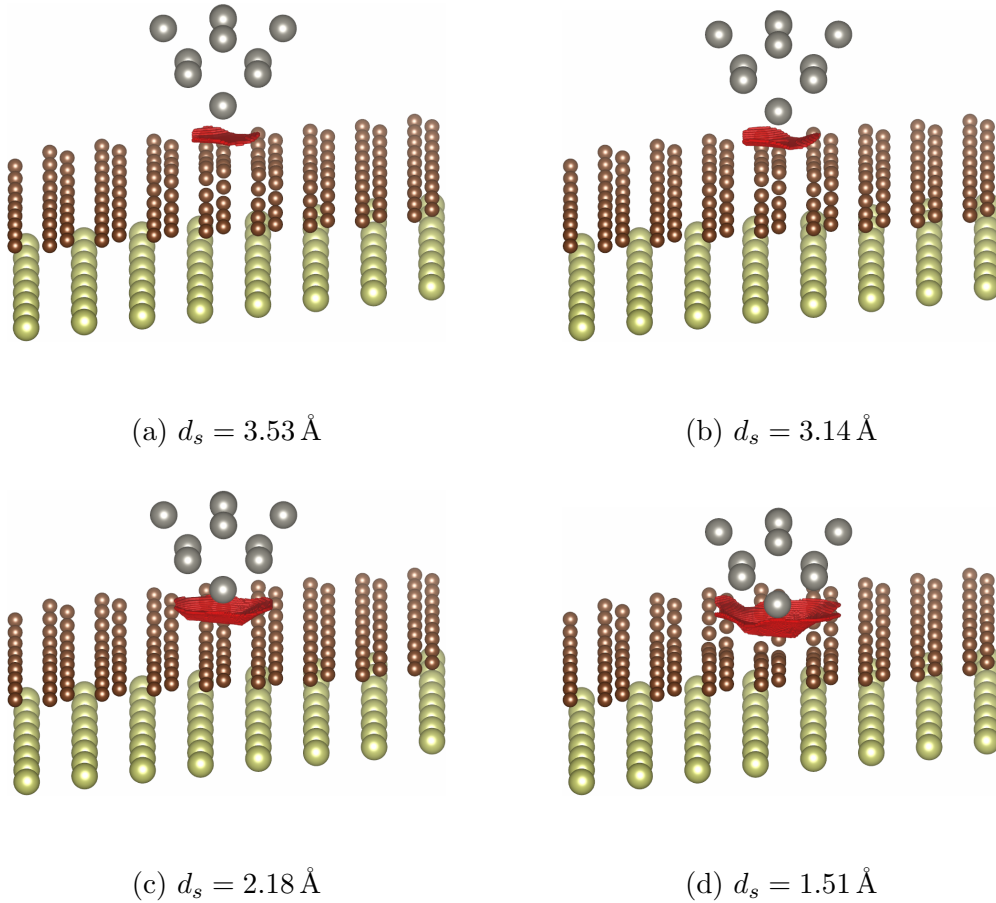
Figure 2.14: Axonometric view of the contact formed by lowering a tungsten tip onto a graphene/Ir(111) surface including the tip, the graphene layer and the first layer of the iridium substrate. The contact area increases from (a) $6.8\,\text{Å}^2$, over (b) $9.1\,\text{Å}^2$, and (c) $16.9\,\text{Å}^2$, to (d) $29.9\,\text{Å}^2$. This figure was created using the VESTA program [119].

Turner, and Szlufarska gives a very comparable area of $13A_{\text{at}} = 17.05\,\text{Å}^2$. However, the 9 outermost atoms that contribute 7% to the area in our model are responsible for nearly 70% of the area in the previously published approach which considers all contacting atoms equally. Only for the two closest positions at $d_s = 1.51\,\text{Å}$ and $d_s = 1.30\,\text{Å}$ more than 13 atoms are in contact, according to the Bader partitioning, and the central 13 are still responsible for 98% and 87% of the contact area, respectively. Including the 6 fourth nearest neighbours into the model by Mo et al. leads to $19A_{\text{at}} = 24.92\,\text{Å}^2$ for both of these distances, while our approach gives $A(1.51) = 28.89\,\text{Å}^2$ and $A(1.30) = 35.03\,\text{Å}^2$. Thus, the results are comparable, but the outermost atoms are again over represented compared to our method. Our approach offers higher resolution in the contact area and allows for a distance dependent contribution of each atom. It is important to note that our contact areas have a more or less pronounced bowl shape (see figure 2.13) while the method by Mo, Turner, and Szlufarska gives flat contact areas. Overall both methods show fair agreement.

Our chosen system, which has been proven to accurately model the interaction between a tungsten tip and moiré graphene on Ir(111) [138], limits our investigation to the attractive region ($d_r \geq 2.24\,\text{Å}$) and small positive loads ($2.18\,\text{Å} \leq d_r < 2.24\,\text{Å}$). For $d_r < 2.18\,\text{Å}$, the tip forms bonds with the iridium substrate leading again to negative values of the load. Thus, it is difficult to predict the behavior of the real contact area A dependent on the load L in this regime. However, we can assume that the interaction potential $E(d_r)$ can be approximated by a Morse potential E_{M} in the vicinity of the minimum [136],

$$E_{\text{M}}(r) = E_0 \left\{ \left[1 - e^{-\gamma(d_r - d_0)} \right]^2 - 1 \right\} \quad , \tag{2.5}$$

where $E_0 = 2.33\,\text{eV}$ is the depth of the potential at the equilibrium position $d_0 = 2.24\,\text{Å}$, values that we can get directly from our data. The third parameter has to be fitted, resulting in $\gamma = 4.11\,\text{Å}^{-1}$. We can now derive the load $L = -\partial E_{\text{M}}/\partial d_r$ yielding

$$L(d_r) = -2\gamma E_0 \left[1 - e^{-\gamma(d_r - d_0)} \right] e^{-\gamma(d_r - d_0)} \quad . \tag{2.6}$$

Solving this equation for d_r produces

$$d_r = d_0 - \frac{1}{\gamma} \ln \xi(L) \quad , \tag{2.7}$$

where

$$\xi(L) = \frac{1 \pm \sqrt{1 - 4u}}{2} \,, \qquad \text{with} \qquad u = \frac{L}{2\gamma E_0} \quad . \tag{2.8}$$

Now it is possible to express the real contact area dependent on load using equations 2.4 and 2.7 and yielding a power law,

$$A(L) = A_0 e^{-\lambda_r(d_0 - \Delta_r)} \left[\xi(L) \right]^{\frac{\lambda_r}{\gamma}} \quad . \tag{2.9}$$

39

As $\gamma = 4.11\,\text{Å}^{-1}$ and $\lambda_r = 4.19\,\text{Å}^{-1}$ the exponent is very close to 1, thus we arrive at a dependence of $A(L) = C\xi(L)$, which corresponds to a increase of A with L to the power of $\frac{1}{2}$.

2.5 Tungsten tip on fcc(111) copper

2.5.1 Introduction

In contrast to section 2.4 where we studied the contact area between a tungsten tip and a stiff and rather inert graphene sheet, we selected a soft metal surface for our second system, fcc copper (111). Another difference to the previously described graphene/Ir(111) system is that we do not expect significant van der Waals forces in the tungsten/copper system. Tungsten and copper are completely immiscible, even in the liquid phase due to the very high positive heat of mixing of about $35.5\,\text{kJ/mol}$ [145]. It is however possible to construct a pseudo-alloy with ultra fine structure by milling tungsten and copper powder in high energy ball mills, a technique known as mechanical alloying [146].

We modeled the copper (111) surface as a 4×4 slab with 4 layers, of which the bottom two were fixed at the bulk positions and the top two were allowed to relax. The lattice constant for the copper slab, $a_{\text{Cu}}^{\text{PBE}} = 3.634\,\text{Å}$, was chosen as the bulk value obtained from relaxation with the PBE functional and is in excellent agreement with the experimental one $a_{\text{Cu}}^{\text{exp}} = 3.615\,\text{Å}$ [147]. The tungsten tip is centered directly over one of the surface atoms and moves down along the c-axis (see figure 2.15). The length of the c axis is chosen so that the distance of the top of the tip to the repeated bottom of the slab in the tip position farthest away from the surface ($d_s = 10\,\text{Å}$) is $10\,\text{Å}$. The lateral dimensions of the unit cell are rather minimalistic as the distance between repeated tips is only marginally larger than $5.6\,\text{Å}$ and interactions between the repeated tips cannot be completely ruled out. Concerning the contact area the unit cell turned out to be just large enough for the ideal cutoff density for this system, but for lower cutoffs and small distances the contact area is bordering the lateral edges of the unit cell, thus the accuracy of its calculation is limited.

2.5.2 Computational methods

The computational set-up for this series of calculations differs significantly to the one described in section 2.4.2. As vdW contributions were not expected to be significant, all relaxations were done with the PBE functional, which belongs to the class of generalized gradient approximation functionals. For reasons of consistency and to ensure comparable

<table>
<tr><td>(a) Side view 1</td><td>(b) Side view 2</td><td>(c) Top view</td></tr>
</table>
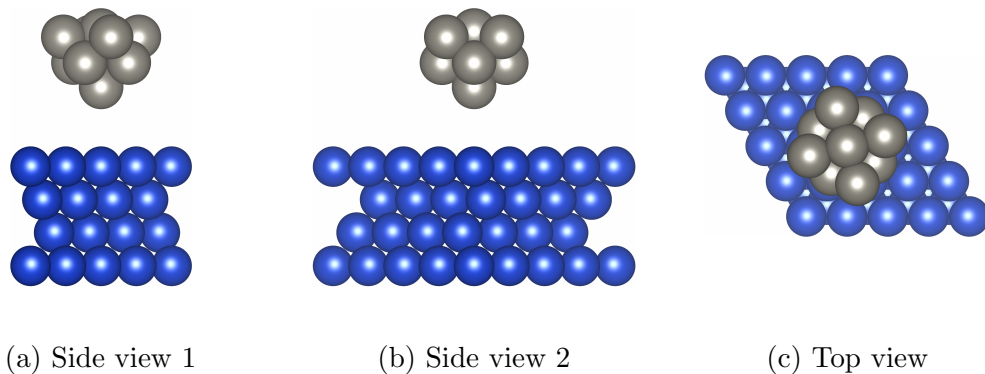
Figure 2.15: Two side (a) and (b), and one top view (c) of the tungsten tip on copper (111) unit cell. Copper atoms are blue and tungsten atoms grey. All atoms are depicted as space filling spheres. This figure was created using the VESTA program [119].

results we also employed the optB86b vdW functional for a static calculation at the PBE relaxed positions. Charge densities used for the Bader partitioning where calculated with the vdW functional. The plane wave cutoff was $341.5\,\mathrm{eV}$ and a Γ-centred $12 \times 12 \times 1$ k-points grid was used to sample the Brillouin zone. For relaxations k-point smearing was done with the first order scheme of Methfessel and Paxton using $\sigma = 0.1$ [141], while the energies and final charge densities were calculated using a tetrahedron method with Blöchl corrections and $\sigma = 0.2$ [148]. Electronic steps were converged to $10^{-6}\,\mathrm{eV}$ and forces were relaxed to $0.01\,\mathrm{eV/Å}$ for the ionic relaxations. To ensure good accuracy for the Bader partitioning scheme a very dense mesh of $432 \times 432 \times 448$ points was used for the grid which is used to calculate the charge densities. Detailed information about the computational methods employed can be found in section 1.3.

2.5.3 Results

Energetics

As it was expected for this system, van der Waals forces do not play a very important role in the adhesion process of a ten atom tungsten tip on a clean fcc Cu(111) surface as can be seen in figure 2.16. For most distances the difference between the two curves is rather small and becomes only substantial for the closest configurations, although the small physisorption minimum around $d_r = 4$ is more pronounced in the vdW corrected calculation. The maximum difference between the optB86b and the PBE results is $1.83\,\mathrm{eV}$ for the closest distance of $d_r = 2.25\,\text{Å}$, but as the total vdW energy of the system at the point is -8.25 eV, the close range GGA part is still responsible for nearly 80% of the

bonding.
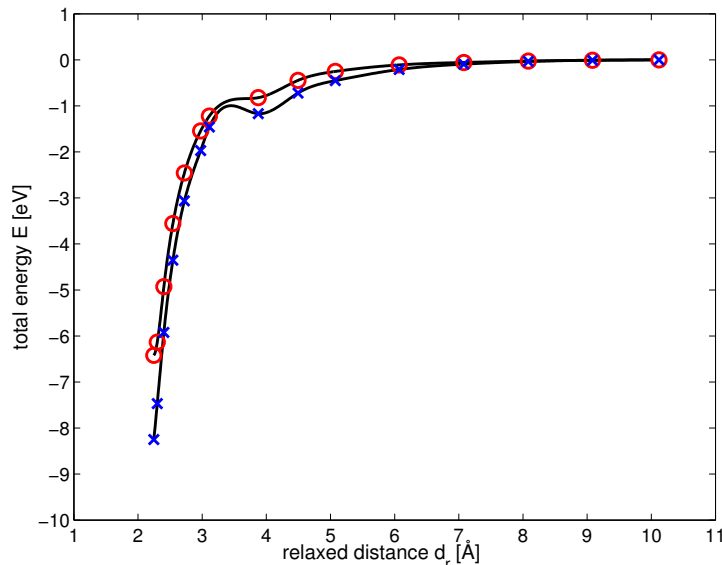
Figure 2.16: Total energy versus distance for relaxed configurations of the tungsten tip on Cu(111). Red circles are calculated with PBE, blue crosses are results obtained with the optB86b vdW functional at the PBE relaxed positions. Black lines are cubic spline fits to guide the eye. The results are normalized to zero for the largest distance.

It is important to note that in figure 2.16, the interaction potential is still attractive for the closest distances and no minimum was found in the potential. The closest point plotted in figure 2.16 is at $d_r = 2.25\,\text{Å}$, however, the distance between the tip apex atom and the copper atom directly beneath it is only $d_s = 1\,\text{Å}$ in the unrelaxed system when the tip is simply lowered on the undisturbed copper surface. This means that the tip is already very close to the surface at this point and the copper atom directly underneath it is pushed $1.25\,\text{Å}$ below the undisturbed surface layer, more than half of the equilibrium interlayer distance of fcc(111) copper planes which is $\sim 2.1\,\text{Å}$. Apparently the energy lost by the significant deformation of the copper surface layer is smaller than the gain achieved by saturating more of the dangling bonds at the surfaces of the slab and the tip.

After pushing the tip even further into the slab ($d_s = 0.5\,\text{Å}$), the surface atom directly below the tip cannot be pressed down much more since the copper layer underneath hinders this move. This results in a complete melting of the two free surface layers around the tip which are rearranged in three irregular layers and coat the tip up to the third (fixed) layer. This process is accompanied with a large energy gain of nearly $4.2\,\text{eV}$ which can be explained by the high surface energy of tungsten, which is, depending on the surface orientation, between $4.01\,\text{J/m}^2$ and $4.64\,\text{J/m}^2$ and thus at least twice that of the (111) surface of fcc copper ($1.95\,\text{J/m}^2$) [149]. It is therefore energetically favorable

to cover the large surface area of the tip as much as possible with copper, even if this means to melt the surface. Effectively this process is analogous to the mechanical alloying mentioned in section 2.5.1. As the interaction is still attractive at this point it is obvious that the assumption that contact is formed if the interaction potential becomes repulsive fails for this system, although it is quite commonly used in literature (see section 2.1).

As the distance to the nearest atom in the layer below the tip apex atom d_r has increased in the melted configuration compared to the one for $d_s = 1\,\text{Å}$ we plot optB86b and GGA energies versus the static distance d_s in figure 2.17.
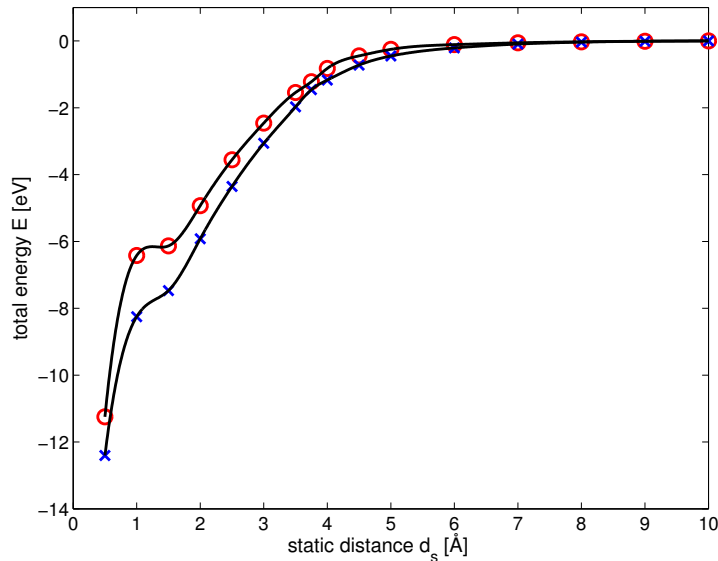
Figure 2.17: Total energy versus d_s of a tungsten tip on Cu(111). Red circles are calculated with PBE, blue crosses are results obtained with the optB86b vdW functional at the PBE relaxed positions. Between $d_s = 1.0\,\text{Å}$ and $d_s = 0.5\,\text{Å}$ the copper surface melts and the two free surface layers transform into three irregular layers around the tip. Black lines are cubic spline fits to guide the eye. The results are normalized to zero for the largest distance.

A preliminary study on the reversibility of this melting effect was conducted by slowly pulling the tip back out of the melted copper and allowing the system to relax at every step. This results in the uppermost copper layer being removed together with the tip, resulting in irreversible wear of the surface. The rather small lateral size of our unit cell, however, might be responsible for some part of this effect.

To obtain some information about the repulsive interactions between the tungsten tip and copper we performed a series of static PBE and optB86b calculations for a single copper atom in different distances to the tungsten tip. The results are plotted in figure 2.18. The minimum energy is reached at a distance of 2.5 Å for both functionals and becomes

43

strongly repulsive for smaller distances, in near perfect agreement with a Morse potential. The results indicate that for the tungsten tip with a single copper atom vdW forces play no role whatsoever in the interaction potential. This again highlights the difficulties one might face when trying to define the onset of contact by distinguishing between short and long range interactions, as proposed in reference 110.
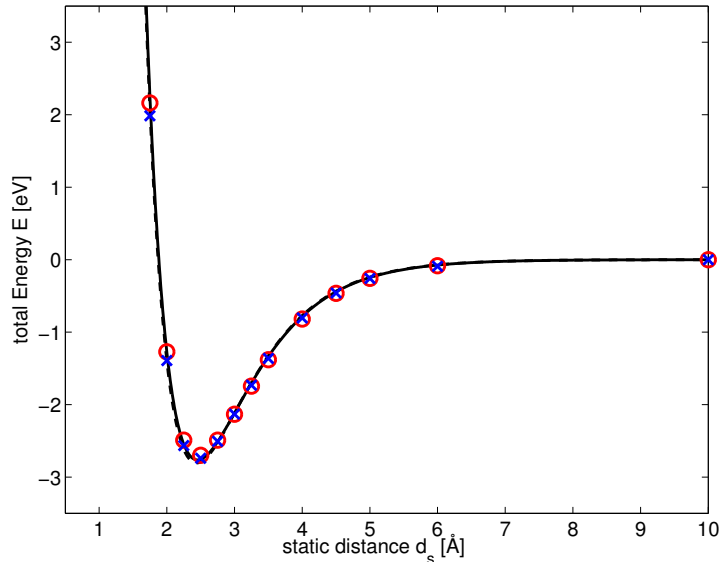
Figure 2.18: Total PBE (red circles) and optB86b (blue crosses) energies versus d_s of a tungsten tip and a single copper atom. The black solid and dashed lines are Morse fits to the data and basically lie on top of each other. The results are normalized to zero for the largest distance. It is evident that the results do not differ essentially.

Geometry

The tungsten Cu(111) system, like the tungsten on grahene/Ir(111) structure, exhibits a pronounced jump to contact where suddenly d_r becomes smaller than d_s. Although vdW contributions are comparably small in this system, the jump happens a little earlier as in the system discussed in section 2.4 between $d_s = 4.00$ Å and $d_s = 3.75$ Å as can be seen in figure 2.19.

Again the jump to contact (0.77 Å) occurs by an upwards movement of the substrate, which is much more compliant than the tungsten tip which moves down by only ~ 0.04 Å. In contrast to the graphene/Ir(111) substrate where a large portion of the graphene layer is bending towards the tip after the jump, only a single copper atom is meeting the tip in this system (see figure 2.20). At a static distance of 2.5 Å the copper surface is relaxed back to its equilibrium position. Although closer positions of the tip are favorable in
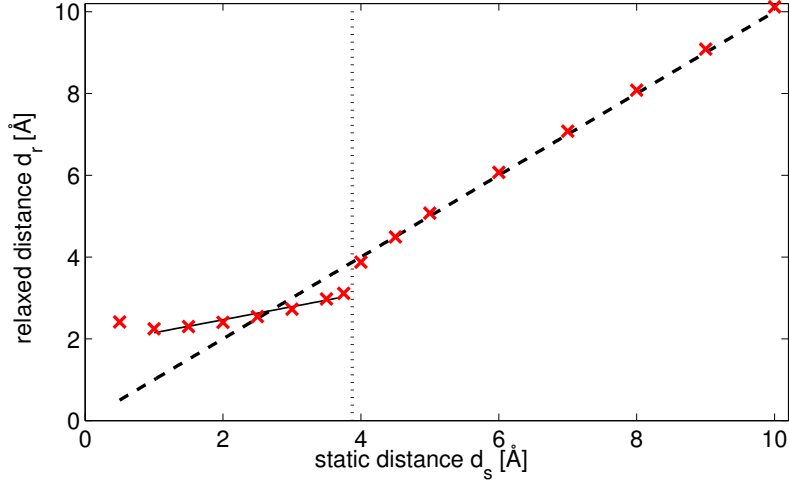
Figure 2.19: Relaxed distance d_r versus static distance d_s for the tungsten tip over Cu(111). The dashed line corresponds to $d_r = d_s$. Between $d_s = 3.75\,\text{Å}$ and $d_s = 4\,\text{Å}$ the jump to contact occurs (marked by the dotted line) and d_r is reduced from $3.88\,\text{Å}$ to $3.11\,\text{Å}$. The linear fit of d_r versus d_s after the jump to contact is marked by the solid black line and omits the data point corresponding to the molten copper slab.

energy, this distance corresponds to the equilibrium separation between the tip and a single copper atom as seen in figure 2.18. At the close distance of $d_s = 1.0\,\text{Å}$, the copper lattice is distorted also in the second layer (see figure 2.20h) and it is rather surprising that the configuration is lower in energy by $3.9\,\text{eV}$ than for the system at $d_s = 2.5\,\text{Å}$ (2.20f). The ability of the two metals to saturate most of the dangling bonds in the contact region and minimize the surface energy is responsible for this strong reduction in total energy. After the jump to contact the d_r versus d_s behavior is again fairly linear, if the data point after the melting transition is excluded. Compared to the case discussed in section 2.4, the slope of the fit (see equation 2.3) is steeper at $\kappa = 0.32$, with an offset of $\delta = 1.83\,\text{Å}$. The melting transition that was described previously and further lowers the total energy is plotted in figure 2.21.

Density cutoff

The determination of the density cutoff needed for the tungsten tip on Cu(111) system is equivalent to the method used in section 2.4. We look for the smallest value of ρ_{cut} that does not predict any formation of contact for distances larger than $d_s = 3.75\,\text{Å}$, the distance where the jump to contact occurs. The linear behavior of A versus d_s that was observed for low cutoffs at the graphene/Ir(111) surface is not pronounced at the Cu(111) surface as can be seen in figure 2.22. The rather noticeable steps between $d_s = 2.0\,\text{Å}$ and

(a) $d_s = 4.0\,\text{Å}$ (b) $d_r = 3.9\,\text{Å}$ (c) $d_s = 3.5\,\text{Å}$ (d) $d_r = 3.0\,\text{Å}$

(e) $d_s = 2.5\,\text{Å}$ (f) $d_r = 2.5\,\text{Å}$ (g) $d_s = 1.0\,\text{Å}$ (h) $d_r = 2.4\,\text{Å}$
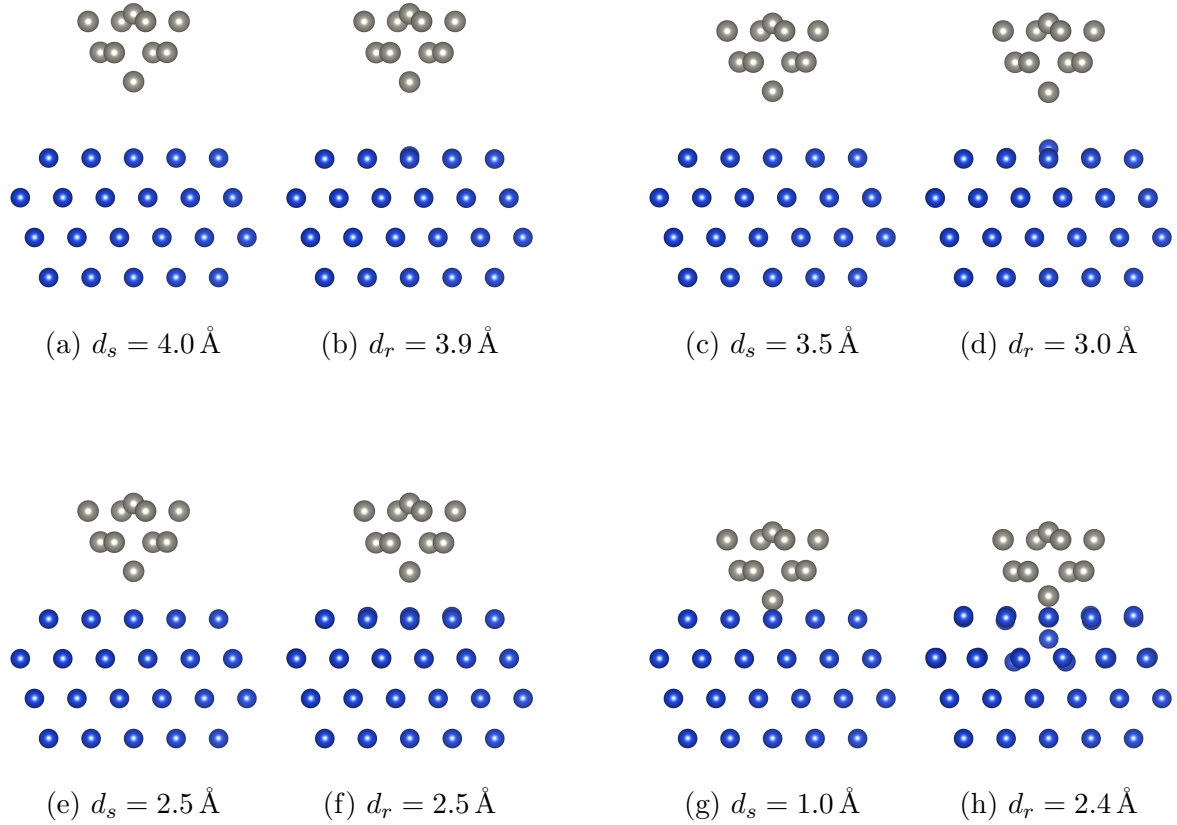
Figure 2.20: Sides views of static and relaxed configurations for different distances d_s and d_r between the tungsten tip and the Cu(111) surface. The upper row shows the system before (a and b) and after the jump to contact (c and d). The lower row depicts the tip in the $d_r = d_s$ position which corresponds to the energy minimum of the tip and a single copper atom in figure 2.18 (e and f), as well as a very close position where the copper atom directly under the tip is pressed significantly into the surface and the second layer is also affected (g and h). This figure was created using the VESTA program [119].

(a) $d_s = 0.5\,\text{Å}$ (b) $d_r = 2.4\,\text{Å}$
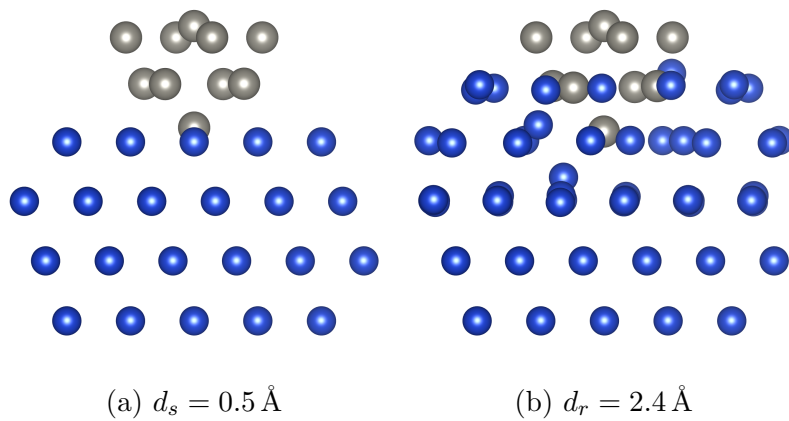
Figure 2.21: Sides views of static (a) and relaxed (b) configurations for the closest distances $d_s = 0.5\,\text{Å}$ between the tungsten tip and the Cu(111) surface. The melting transition occurs and an additional irregular copper layer is formed, covering a large portion of the tip. This figure was created using the VESTA program [119].

$d_s = 2.5\,\text{Å}$ for a ρ_{cut} of 1×10^{-1} and 5×10^{-2} correspond to the formation of contact of the second layer of the tip with the surface, while the curve visible for higher cutoffs hint at the true exponential relation of $A(d_s)$. The points for the closest distance $d_s = 0.5\,\text{Å}$ are not included in the linear fits, which are plotted for the sake of comparison, as the melting transition has already occurred at this point, approximately doubling the contact area. The scale of the plot is too small for the corresponding points of the two lower cutoff values to be shown. The jump between $d_s = 4.5\,\text{Å}$ and $d_s = 4\,\text{Å}$ for $\rho_{\text{cut}} = 1 \times 10^{-3}\,\text{e}/\text{Å}^3$ also corresponds to the onset of contact of the second tip layer. For $d_s < 4\,\text{Å}$, the values of A are inaccurate for this low cutoff as the contact area is beginning to reach the edges of the unit cell.
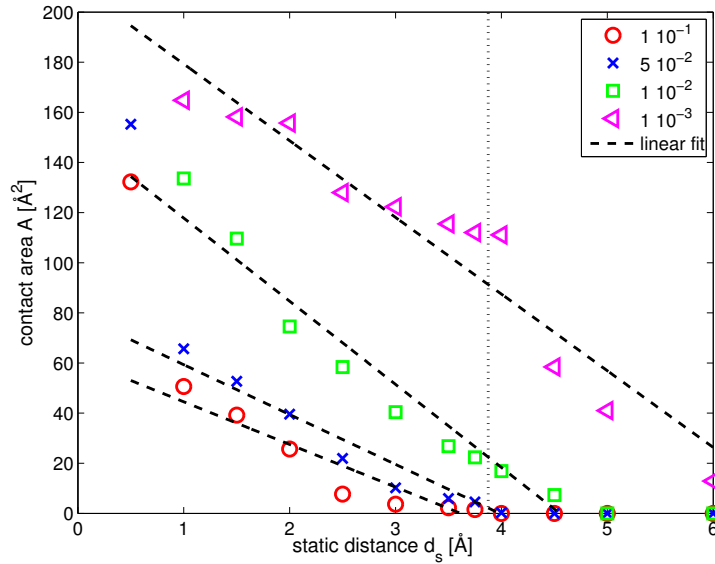
Figure 2.22: Real contact area A of the relaxed system versus the distance of the static tip to the undisturbed copper surface d_s for several density cutoffs. The vertical dotted line marks the jump to contact. Data for the linear fits do not include the contact area after the surface melting or any other than the first point with vanishing contact.

As we want to establish contact for all distances $d_s < 4\,\text{Å}$, figure 2.22 seems to suggest the value of $\rho_{\text{cut}} = 5 \times 10^{-2}\,\text{e}/\text{Å}^3$, the same value found for the system examined in section 2.4. If one looks closely at the data, however, this density cutoff still produces a small unwanted contact area for $d_s = 4\,\text{Å}$ of $0.24\,\text{Å}^2$. The value of ρ_{cut} therefore has to be increased to $5.3 \times 10^{-2}\,\text{e}/\text{Å}^3$, 6% higher than for the tungsten on graphene/Ir(111) system. Comparing the areas of contact obtained with $\rho_{\text{cut}} = 5.3 \times 10^{-2}\,\text{e}/\text{Å}^3$ with the ones calculated for $\rho_{\text{cut}} = 5 \times 10^{-2}\,\text{e}/\text{Å}^3$, the latter one gives results that are $\sim 7\%$ larger than the former one for largest distances. At closer separations when the contact areas become larger this difference is reduced to under 3%. Table 2.2 shows that this slightly increased

ρ_{cut} [e/Å^3]	1×10^{-1}	5.3×10^{-2}	1×10^{-2}	5×10^{-3}	1×10^{-3}
$N_{\text{e}}/N_{\text{tot}}$ [%]	2.02	1.12	0.25	0.13	0.02
N_{e}	15.46	8.55	1.90	0.98	0.18
$R_{\text{B}}(\text{W})$ [Å]	2.5	2.8	4.1	4.7	6.2
$R_{\text{B}}(\text{Cu})$ [Å]	2.1	2.3	3.5	4	5.4

Table 2.2: Number of electrons N_{e} lost to the vacuum region depending on the chosen density cutoff value, both in absolute numbers and in a percentage of the total number of electrons. The radius of a single (spherical) tungsten Bader-atom $R_{\text{B}}(\text{W})$, and a single (sperical) copper Bader-atom $R_{\text{B}}(\text{Cu})$, in a large box dependent on ρ_{cut}.

cutoff value is still reasonable, as just over one percent of the electrons in the system are lost in the vacuum region. The radius of a single copper Bader-atom is also reasonable and with 2.3 Å significantly larger than the reported empirical value of 1.35 Å [142], the previously calculated value 1.4 Å [143], and the van der Waals radius 1.4 Å [144]. The radius of the tungsten Bader-atom at 5.3×10^{-2} electrons per Å^3 is decreased by 0.1 Å to 2.8 Å, compared to the value for 5×10^{-2} e/Å^3 reported in table 2.1 in section 2.4.

Contact area

Figure 2.23 shows the total contact area and the contributions to it from the tip apex atom and the rest of the tip versus the relaxed distance d_r. As seen before in section 2.4, the total contact area increases exponentially with decreasing distance. In this case, the function $A(d_r) = A_0 \exp(-\lambda_r(d_r - \Delta_r))$ (see also equation 2.4) is an excellent fit to the data, using the coefficients $\lambda_r = 3.64$ Å^{-1}, and $\Delta_r = 3.39$ Å. Again, $A_0 = 1$ Å^2 is not used as a fitting parameter and is only included for dimensionality considerations. The data point at $d_s = 0.5$ Å has been omitted in both figure 2.23 and the exponential fit, as the melting transition increases the contact area from 64.2 Å^2 by $\simeq 140\%$ to 153.8 Å^2, while the relaxed distance is actually slightly increasing from $d_r = 2.25$ Å at $d_s = 1$ Å to $d_r = 2.41$ Å at $d_s = 0.5$ Å. Using the parameters $\kappa = 0.32$ and $\delta = 1.83$ Å that define the linear relation $d_r = \kappa d_s + \delta$ it is again possible to calculate $A(d_s)$, which is important as d_s is easier accessible in experiments than d_r. We obtain $A(d_s) = A_0 \exp(-\lambda_s(d_s - \Delta_s))$, with $\lambda_s = \lambda_r \kappa \simeq 1.2$ Å^{-1} and $\Delta_s = (\Delta_r - \delta)/\kappa \simeq 4.9$ Å.

At $d_r < 2.54$ Å, the second tip layer is also contributing to the total contact area. In figure 2.24, this corresponds to the images 2.24d – 2.24f. While the contact area is a flat round disc at the onset of contact when only the apex of the tip is touching the surface
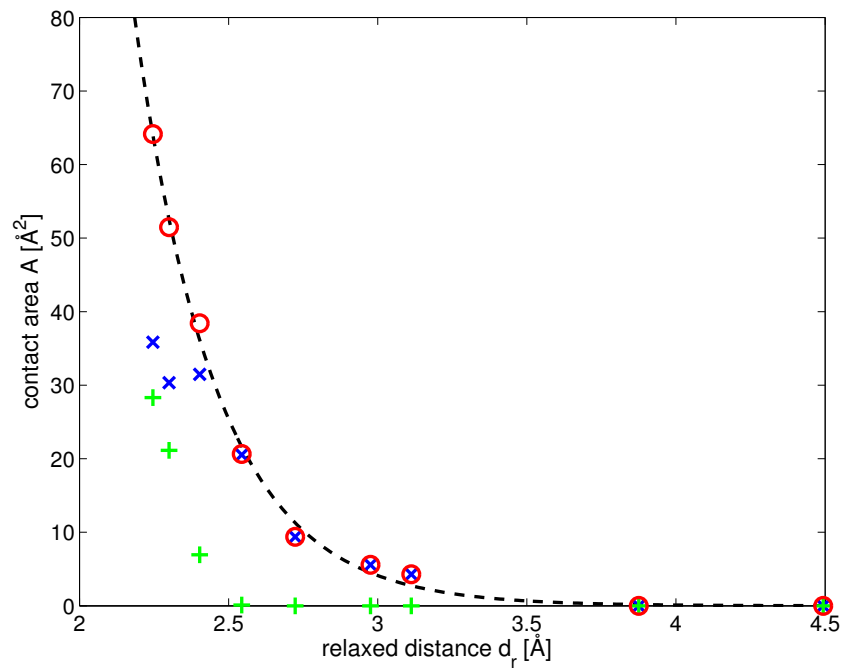
Figure 2.23: Real contact area A versus relaxed distance d_r for a tungsten tip lowered onto a Cu(111) surface. Blue crosses correspond to the contribution of the apex atom of the tip, green plus signs to the contribution of the other layers (nine atoms) to the total contact area which is plotted in red circles. The dashed line is an exponential fit to the total area (red circles). The contact area after the melting transition is not plotted.

(see figures 2.24a and 2.24b), a pronounced bowl shape is formed as the second layer of the tip starts to contribute (see figures 2.24d to 2.24f). While the edges of the bowl show the fourfold symmetry of the tip, the bottom is shaped according to the sixfold symmetry of the copper surface. The contact area after the surface melting transition is predictably not perfectly symmetric, the bowl is significantly deeper and the edges curve not strictly outward any more (figure 2.24f). The contact area after melting is shown together with the tip and the melted surface in figure 2.25. Here the unit cell is at its limit, as it is just large enough laterally to keep the surface area inside the borders and the four layers of copper are barely enough to describe the melting.

2.6   Summary and conclusion

In this chapter we proposed a new way of calculating the true contact area between a tip and an arbitrary surface. We use an "atoms in molecules" approach to calculate the volumes and shapes of the atoms that might be in contact, which leads to a straightforward way of determining the contact area at each given distance, as the magnitude of the contact area can be easily calculated by triangulation if the shapes of the contacting atoms are known. The method of choice for the partitioning of the charge density into the atoms is Bader's approach, as it results in non-overlapping atoms with sharp borders (see section 2.2). However, we need to define a specific density cutoff ρ_{cut} for this partitioning as the surface Bader-atoms have infinite size otherwise and contact would be established for all distances.To calculate this cutoff density we use the discontinuity in the d_r versus d_s curve, which occurs in the examined systems due to a jump to contact, which is commonly observed in AFM experiments. The correct value is the lowest possible ρ_{cut}, to have the maximum number of electrons accounted for in the partitioning, which gives non-zero contact area only for distances below the jump to contact. Thus our approach is an *ab-initio* method, as the only parameter needed can be calculated from properties of the system. We believe that the jump to contact is a less ambiguous way to define the onset of contact than using a division of the interaction in long- and short-range parts [110], or equating contact with repulsive interactions [111, 113].

We tested our model on two systems, both involving the same model of a tungsten AFM tip using a ten atom pyramid. We chose different counter surfaces that differ significantly in their interaction with the tip. The first system, which is described in detail in section 2.4, is a graphene layer forming a moiré pattern on an fcc Ir(111) surface. In this system van der Waals interactions are an important part of the tip-surface interaction which is of moderate strength (the potential depth is $\sim 2.25\,\mathrm{eV}$). Of course graphene is the strongest material ever measured, so the tip is unlikely to damage it even in close

(a) $d_r = 3.11\,\text{Å}$
$A = 4.3\,\text{Å}^2$

(b) $d_r = 2.72\,\text{Å}$
$A = 9.4\,\text{Å}^2$

(c) $d_r = 2.54\,\text{Å}$
$A = 20.6\,\text{Å}^2$

(d) $d_r = 2.30\,\text{Å}$
$A = 51.5\,\text{Å}^2$

(e) $d_r = 2.25\,\text{Å}$
$A = 64.2\,\text{Å}^2$

(f) $d_r = 2.41\,\text{Å}$
$A = 153.8\,\text{Å}^2$
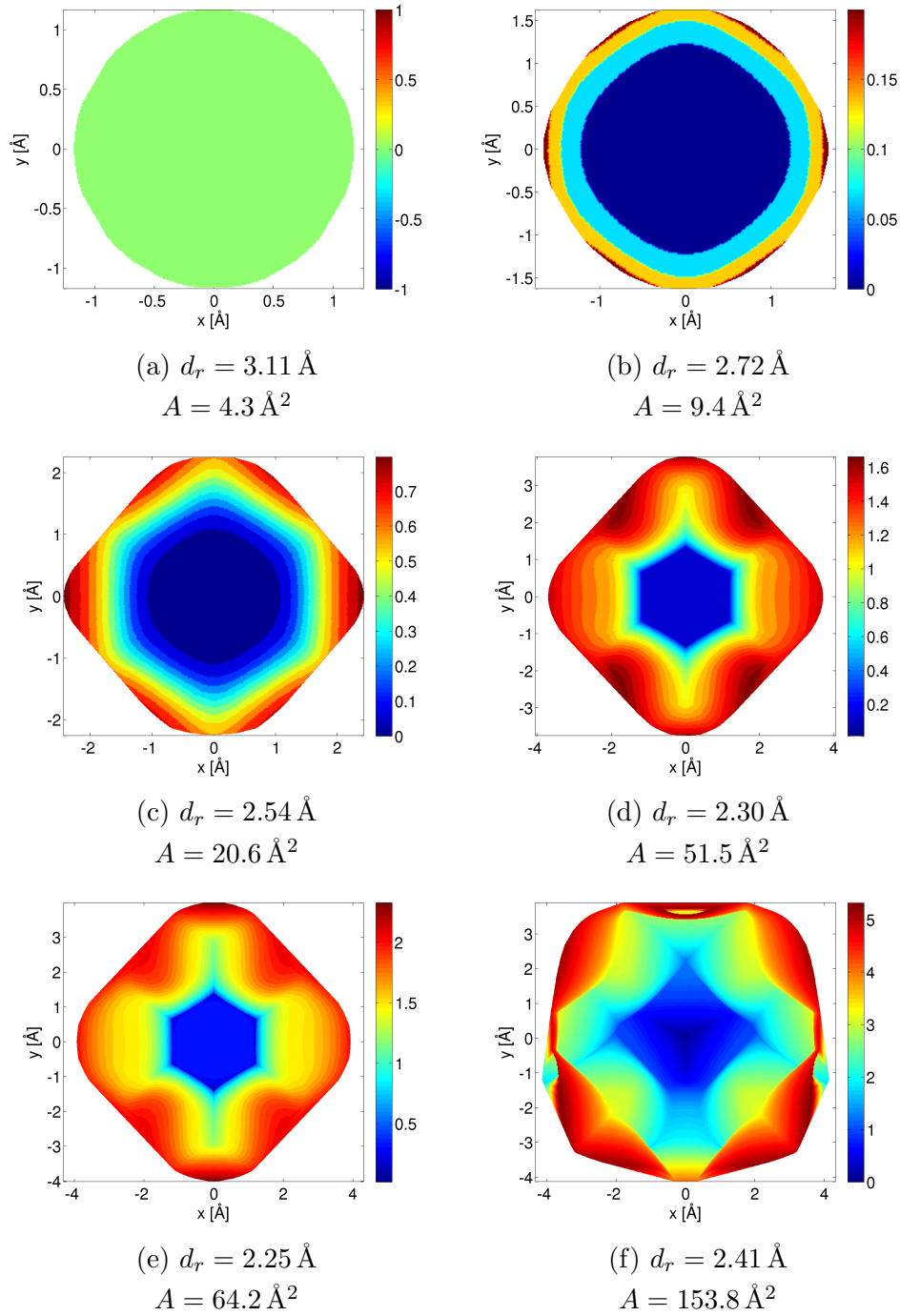
Figure 2.24: Top view of the contact area formed by lowering a tungsten tip onto a Cu(111) surface. At first (a–c) only the tip apex atom is involved in forming the contact to the surface, while the second layer begins to interact in panel (d). The surface has melted and formed an additional layer, more than doubling the contact area in the last panel (f). Different heights are coded by color. Please note the different color bars and axes scaling in each panel.
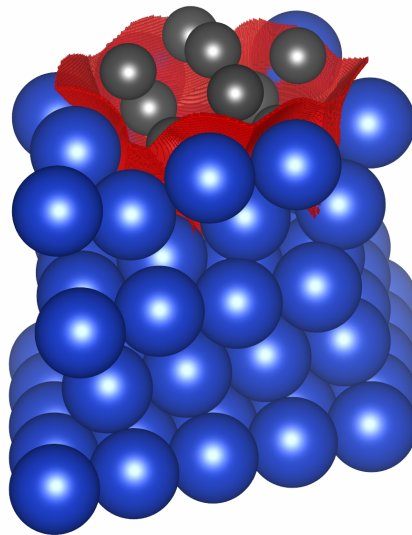
Figure 2.25: The tungsten tip (grey spheres) has penetrated the copper surface (blue spheres) far enough to cause it to melt. The contact area is plotted as a red surface. Clearly the whole tip is in contact with the surface. This figure was created using the VESTA program [119].

contact [150]. This system was chosen because of the models realism which was previously tested by its ability to explain contrast inversion in AFM/STM experiments [138, 139]. The second system, a fcc copper (111) surface (see section 2.5), was chosen for its differences to the graphene/Ir(111) surface, as copper is very soft and vdW interactions are expected to be small. The interaction between the tungsten tip and the copper surface, however, is very strong and we observe melting of the copper surface with an energy gain of about $4\,\mathrm{eV}$ to a total interaction energy of $\sim 12\,\mathrm{eV}$.

We observe a exponential dependency of the real contact area A depending on the relaxed distance d_r for both systems. Using the relation between the relaxed distance d_r (corresponding to the position of the tip support) and the static distance d_s, which is linear after the jump to contact, we are able to calculate the parameters defining $A(d_s)$ directly from the fitting parameters of $A(d_r)$. Since d_s might be easier to obtain from experiment, the linear relation between d_r and d_s is an important result, allowing the conversion of $A(d_s)$ to $A(d_r)$ and vice versa.

Perhaps the most important result of this work is the very similar ideal cutoff density for both systems which differs by only 6% at $\rho_{\mathrm{cut}}^{\mathrm{Gr}} = 5.0 \times 10^{-2}$ electrons per Å^3 for the graphene layer on Ir(111) and $\rho_{\mathrm{cut}}^{\mathrm{Cu}} = 5.3 \times 10^{-2}$ electrons per Å^3 for the copper (111) surface, which have distinctively different properties. This might be a sign that ρ_{cut} is a rather universal constant of about $5 \pm 0.5 \times 10^{-2}\,\mathrm{e}/\text{Å}^3$, which would make at least an estimation of the real contact area possible for systems which do not show a pronounced jump to contact and thus impede the calculation of the exact density cutoff. However, further systems, especially with different tips, have to be investigated before this claim can be made with confidence.

While we believe that our *ab-initio* method of calculating the real contact area is a intuitive and accurate approach, the limitations have to be discussed. As the charge density is needed to perform the Bader partitioning the technique is limited to system sizes where DFT calculations are still possible. With the ever increasing power of modern computers and better scaling codes, however, it might soon be feasible to push this limit to several thousand, if not a million, atoms and use our approach during *ab-initio*-MD calculations to directly investigate the influence of the true contact area on frictional forces. While the application to huge, rough systems with multiple asperities, where the accurate calculation of the real contact area is arguably most interesting, is at present unrealistic, insights can be gained for smaller prototype models, which can be calculated with *ab-initio* methods. Once knowledge about the behavior of the contact area for several geometries is known from this prototype systems, an empirical fitting scheme for large scale models might be developed.

The most important results of this chapter are currently prepared for publication.

Chapter 3

An ab-initio model for calculating nanofriction forces in dry sliding systems

> *"If there's a buzzing-noise, somebody's making a buzzing-noise, and the only reason for making a buzzing-noise that I know of is because you're a bee." Then he thought another long time, and said: "And the only reason for being a bee that I know of is making honey." And then he got up, and said: "And the only reason for making honey is so as I can eat it." So he began to climb the tree.*

<div align="right">A. A. Milne, "Winnie-the-Pooh", 1926</div>

3.1   Introduction

In the 17th and 18th century Amontons and Coulomb formulated the basic laws of friction, which state that the macroscopic friction force is independent of the apparent contact area and varies linearly with the external load at moderate constant sliding velocities [5, 6]. These friction laws have been further extended by Derjaguin for adhesive surfaces, so that a non-vanishing friction force can occur even for zero load [7]. Although generally very successful, on the nano-scale deviations from this classical behavior have sometimes been observed depending on the sliding conditions. If the contacting surfaces are aligned incommensurately, friction can be reduced by several orders of magnitude and structural superlubricity may occur [151–155], though this phenomenon is suspected to be unstable at least for graphene flakes on graphite [156, 157]. It also has been proposed that the drastic reduction of frictional forces may not stem from incommensurability but from

thermal effects and the low effective mass of the nanocontact [158, 159]. Inclusion of third bodies between incommensurate contacts hinders structual superlubricity and leads to a linear behaviour of friction on load [160, 161], which is also recovered from thermodynamic considerations [162]. Other studies report a greater than linear [163], or sublinear dependence of the friction force on load [109, 110, 164] where the latter is consistent with classic Hertzian contact mechanics [98]. Also even more complex dependencies of the friction force on the load have been reported [112, 165]. A more general overview on friction simulations on the nanoscale may be found in two recent reviews [15, 20]. Friction forces can also depend on the sliding direction as shown in experiments on rather complex geometries [166, 167], and recently by Weymouth et al. for a single atom asperity [168].

While the conventional method of choice for simulating atomic scale friction is classical molecular dynamics (MD), see Ref. 20 and references therein, *ab-initio* density-functional-theory (DFT) approaches [39, 40] have become more common during recent years [21–28]. This is due to advantages in accuracy and the increasing power of computers which retain the simulation time manageable. In classical MD simulations, energy becomes dissipated to a heat bath via a thermostat, a method which is in principle also possible for DFT calculations. As simulation times for *ab-initio* MD are very short and thermostating is difficult due to a rapid heating of the electronic system, it is desirable to formulate a different way to describe dissipative sliding and to predict coefficients of friction within DFT. This may be done by computing potential energy landscapes and fitting the resulting energy barriers to mechanical models, for example the well known Prandtl-Tomlinson model [16, 17]. Another approach was suggested by Zhong and Tománek, who, in their "maximum-friction microscope" model, assume a complete dissipation of the potential energy into phonons and electronic excitations for each slip [18, 19] (see also section 1.2.1).

3.2 Basic model

Considering all the different concepts and methods introduced in the last section, we attempt to formulate the problem of dry sliding friction on the basis of parameter-free (*ab-initio*) calculations. We rely only on the quantum-mechanical interactions to describe the stick-slip processes taking place between the sliding bodies. To this end we propose energy dissipation via the relaxations in the sliding materials themselves as calculated *ab-initio*. We will show that the concept allows to analyses arbitrary sliding directions and sliding paths up to μm scale in length with a single initial set of DFT calculations. This permits us to gain insight into the different behavior of periodic and aperiodic (defined below) sliding directions by bridging four orders of magnitude in length scale.

3.2.1 Unit cells

The surfaces themselves are modeled by six atomic layer thick slabs, free to relax at the side of contact and terminated by two fixed bulk-like layers at the opposite sides. An example of the geometry is given in figure 3.1. To make sure that six layers in each
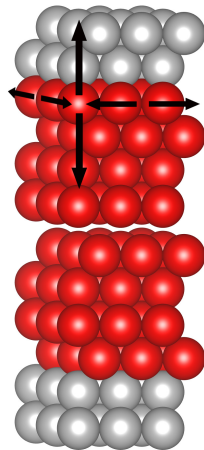
Figure 3.1: Sketch of a simulation cell containing 12 Cu atoms, tripled in the x and y direction for clarity. The top slab is displaced in the x and y direction to collect data on energies and forces and in this case also vertically to simulate several load conditions. Red atoms are allowed to relax, while grey atoms are kept rigid at their bulk-like positions. This figure was created using the VESTA program [119].

slab are sufficient to model the tribological contact we analyzed the lateral and vertical displacements of atoms in each layer for every grid point in the prototype system of fcc Al(111) on fcc Al(111) in constant distance sliding (the results of the friction calculations can be found in section 3.3). We calculate the lateral distance from the ideal hollow position between the three nearest neighbors above and below each layer and scale the distance as follows: A perfect fcc or hcp position is counted as zero and the worst possible on top position is counted as one. The energetically worst configuration of a layer is therefore 2, if both the layer above and below are aligned in the worst possible way. In the static case, all but the middle two layers are aligned perfectly, so only the middle four layers are shown in figure 3.2. The relaxed case is shown in figure 3.3. Note that the out of plane relaxations are increased five times for better visibility and that the color scales for figures 3.2 and 3.3 are different. Both the lateral as well as the vertical misalignment is reduced to very small values only a few layers away from the slip plane (between layer 6 and 7).
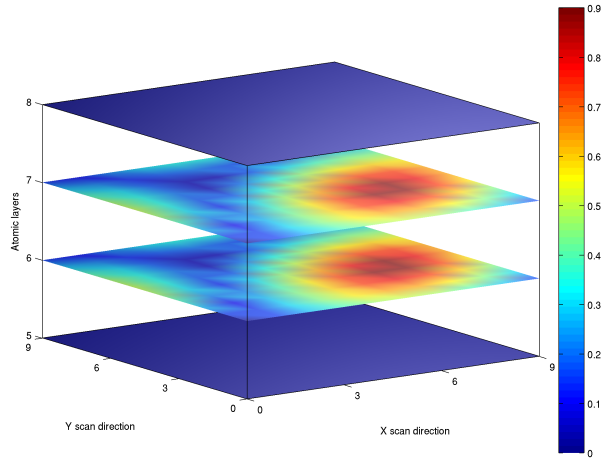
Figure 3.2: fcc lattice mismatch before the structure was relaxed. Only the middle 4 layers are shown
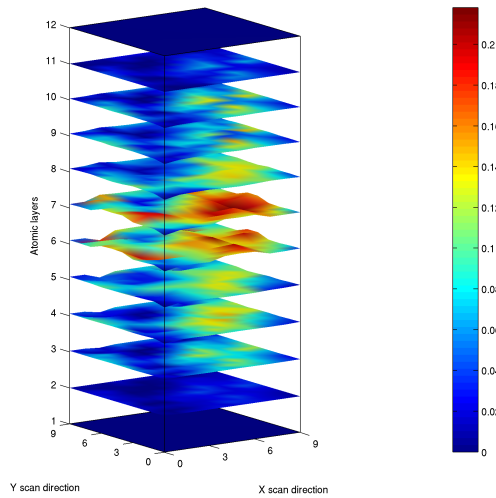
Figure 3.3: Mismatch of the atomic layers after relaxation for all 100 positions of the scan for fcc Al. The maximum stacking error is about 10 % of the maximum value 2; variations in the z-direction due to relaxation are increased five times.

To check if the slab thickness, with six layers each, is wide enough, an additional layer was placed on top of the upper slab at the ideal interlayer distance and perfect lateral stacking position. During the following relaxations, the lower of the two former fixed layers was released, so that the bottom slab now consisted of the usual six layers, two of them fixed and four free, but the upper slab now had seven layers, five of them free.

As can be seen in figure 3.4, the additional layer reduces the average displacement of the atoms in the upper slab as was to be expected. However, both the slip plane itself as well as the next layers give qualitatively the same results, thus justifying the originally chosen geometry of the six layer slab.
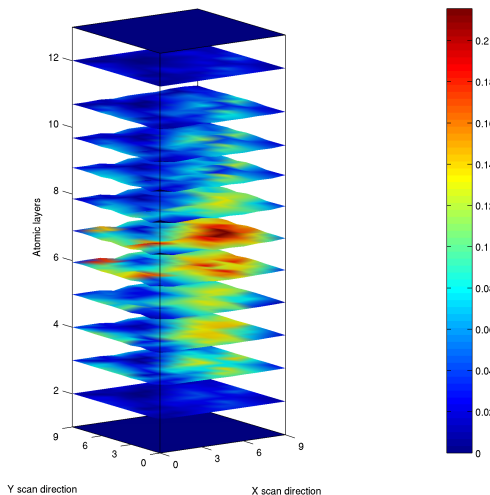
Figure 3.4: Mismatch of the atomic layers after relaxation for all 100 positions of the scan for fcc Al with an additional relaxed layer. The maximum error in stacking is still about 10 % of the maximum value 2, and the fault introduced by the misalignment in the middle is only marginally felt by the now free 11th layer. Variations in the z-direction due to relaxation are increased five times.

3.2.2   Grid method

It is possible to map all energies and forces that result from arbitrary lateral positions of the two slabs in contact onto the relatively small unit cell. This allows to use DFT with all the advantages that this *ab-initio* method provides as mentioned in section 1.3. The main advantage of the grid method is that once all the points in the unit cell are sampled it is possible to lay paths of arbitrary lengths in every direction without any additional computational cost. This is possible as all lateral configurations of the slabs are represented in the unit cell and if the sliding distance is greater than the length of the unit cell, the periodic boundary conditions dictate that the appropriate sliding path re-enters the cell on the opposing site of the exit point. The lateral moving process of two surfaces in contact is reduced to the movement of a single point on energy and force surfaces in a single unit cell. This is visualized in figure 3.5 for three different sliding directions. Two of those paths (red and blue) are periodic, and could also be quite

59

easily described with another method which does not rely on a grid and the periodicity of the unit cell. The third direction, however, leads to an aperiodic sliding path which gradually fills up the whole unit cell. (We note that due to the inevitable representation of irrational numbers by rational fractions in a computer these paths are essentially also periodic, however, with very long periods.) It is to be expected that the frictional response will therefore strongly depend on the section of the unit cell that is currently traversed and that the average of the friction force will only converge if the sliding path is rather long (a couple of hundred Ångstroms) to allow the whole unit cell to become sampled. It would be very time demanding to simulate such long sliding paths with anything other than a grid method.

(a) 0.5 Å

(b) 2.5 Å

(c) 5 Å

(d) 50 Å
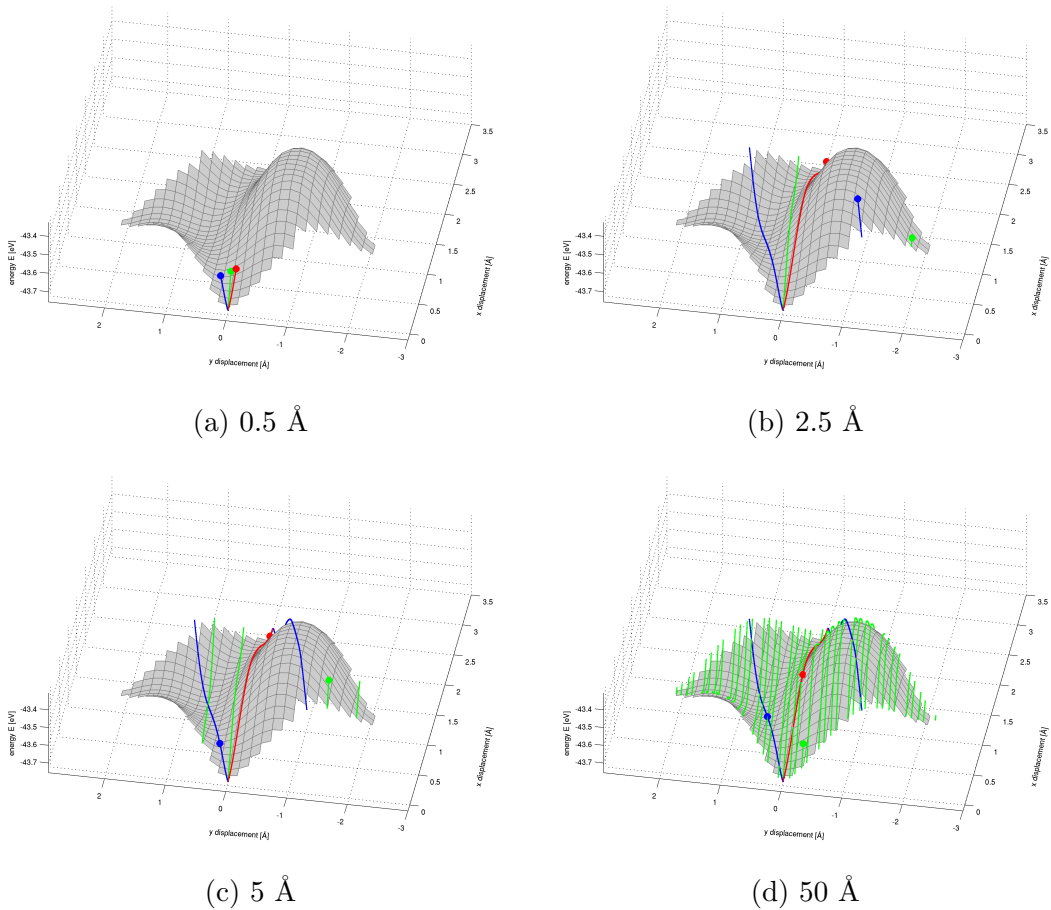
Figure 3.5: A visualization of three sliding paths of equal length and different directions in an static energy landscape of two Cu(111) surfaces sliding against each other. The red (0°) and the blue (30°) paths are periodic whereas the green one (10°) is aperiodic and never reaches the starting point again while gradually sampling the whole unit cell.

However, such a grid approach has the drawback of being quasi static and therefore

being incapable of producing all dynamic properties of the system as every point is calculated independently of all others. However, since we are investigating only wearless sliding this is a reasonable restriction. In the development of the method and the first applications we restricted ourselves to a 1×1 unit cell in the lateral direction. This further limits the describable frictional response of the system as the periodic boundary conditions in the x and y direction in combination with the 1×1 unit cell describes infinite and perfectly flat surfaces. Thus, surface defects or reconstructions can not be modeled. The advantages of such a small cell are apparent: The total computation time is reduced to a manageable value without compromising any accuracy by selecting for example a lower plane wave cut off energy or a less dense grid in k-space. In sections 3.3 to 3.7 we demonstrate that these restricted systems yield a multitude of interesting results and are sufficient to prove the applicability of the method, however, while the grid method restrains some dynamic aspects of the sliding system and prohibits wear formation in the present form there is no principal need for the restriction to small unit cells and flat surfaces.

All forces and energies which are calculated on a regular grid in the unit cell of the sliding system are interpolated with cubic splines to construct smooth energy and force surfaces. This alone is insufficient to describe non trivial sliding, as there is no mechanism for the dissipation of energy yet. Looking at figure 3.5 one quickly realizes that frictional forces for periodic sliding directions will exactly cancel out if the path length is an integer number of multiples of the period length. The same is true for a sufficiently long aperiodic path, which will come arbitrary close to the starting point again. In a more generalized view the calculated energy maps are conservative potentials and all closed paths in conservative potentials lead to zero net work. An example of this is given in figure 3.6. This problem is present for all *ab-initio* calculations and also for MD, although there it can be avoided by thermostating the system accordingly.

3.2.3   Our dissipation model

In order to have a truly *ab-initio* approach, an inclusion of any additional forces in terms of "springs" into our model has been avoided. In this sense the concept of complete dissipation as in the "maximum friction microscope" (see section 1.2.1) does seem a little too simplified to capture essential features of atomic stick-slip motion. In particular we aim to include the possibility of transferring some of the kinetic energy of the tip during a slip back into potential energy. This means that some of the kinetic energy should be used to climb the next maximum in the potential instead of being completely dissipated into phonons and ultimately heat. We also wanted to model the relaxations during a
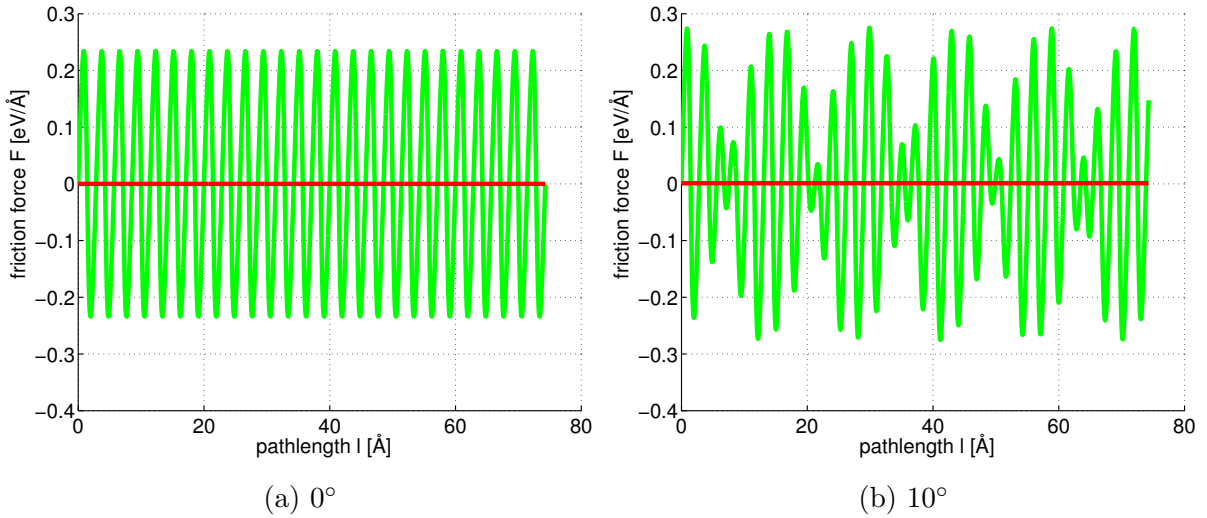
Figure 3.6: An example for conservative movement for a closed path (a) and a sufficiently long aperiodic path (b). The friction force F is plotted over the sliding distance l (green) and the average of this force over the whole path is also shown (red).

slip by actually relaxing the sliding system using the correct forces arising from the ionic configuration and the electronic band structure. To this end we calculated all forces and energies for both static shearing of the slabs in contact as well as a relaxation at each of the grid points. After we choose a sliding direction and a path length we then cut through both the relaxed and the unrelaxed energy surfaces along that direction and calculate the friction force in the following way:

Along each path we identify the local minima and maxima on the energy curve of the unrelaxed system. We assume static sliding without relaxations until a maximum in the energy is encountered. At this point we allow the built up strain to be released by relaxing the tribologically active zone. The resulting energy difference is now assumed to be dissipated into the bulk crystal via phononic excitations and is ultimately lost as heat. As the relaxed energy surface is also corrugated, the movement to the next minimum may result in small gains or losses in the energy leading to small negative or positive friction forces along this portion of the path. When the next minimum in the unrelaxed surface is encountered the cycle is repeated until the desired path length is reached. If the local minimum of the unrelaxed energy curve is not at the same energy as the relaxed curve, an appropriate portion of the dissipated energy from the last slip is used to bring the system back to the unrelaxed sliding position. The process is visualized in figure 3.7.

For the data containing the relaxed and the unrelaxed energy curves as well as the positions of the minima and maxima we propose two distinctively different ways to calculate the mean friction force denoted by $F^{(1)}$ and $F^{(2)}$. To calculate $F^{(1)}$ we determine
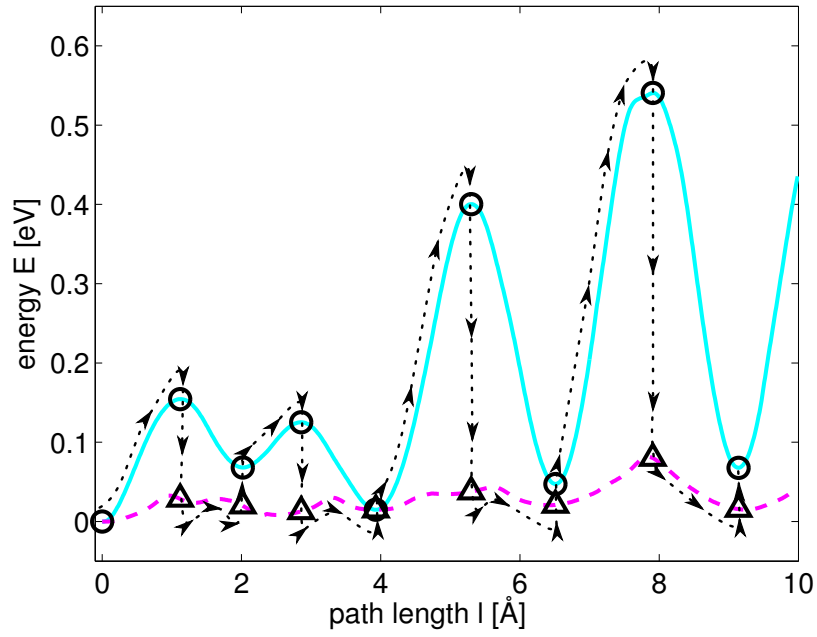
Figure 3.7: Illustration of the energy dissipation model along a 50° sliding path of a Cu(111) on Cu(111) sliding system. The solid (cyan) line gives the energy for the unrelaxed slabs with the open (black) circles denoting local minima and maxima. The dashed (magenta) line shows the energy for the relaxed slabs with open (black) triangles marking the positions of the extrema of the unrelaxed slabs. The dotted (black) line is a schematic route for the calculation of the energy differences between the open circles and triangles, see equation (3.2).

the Hellmann-Feynman forces acting on the individual atoms in our *ab-initio* calculation [169]. We perform an arithmetic average of all force components of the upper slab parallel to the sliding direction following the path described above, e.g., as indicated in Fig. 3.7 by the dotted line. The contributions of the unrelaxed and the relaxed forces to $F^{(1)}$ are marked by the superscripts U and R while N_{U} and N_{R} are the total numbers of sampling points on the unrelaxed and relaxed energy curves yielding

$$F^{(1)} = \frac{1}{N_{\mathrm{U}}} \sum_{i=1}^{N_{\mathrm{U}}} F_i^{\mathrm{U}} + \frac{1}{N_{\mathrm{R}}} \sum_{j=1}^{N_{\mathrm{R}}} F_j^{\mathrm{R}} \quad . \tag{3.1}$$

In contrast, $F^{(2)}$ is defined via the sum over the gains and losses of energy along the sliding path divided by the path length l,

$$\begin{aligned} F^{(2)} &= \frac{1}{l} \left[\sum_{i'=1}^{N_{\max}} \left(E_{i'}^{\mathrm{U}} - E_{i'}^{\mathrm{R}} \right) - \sum_{j'=2}^{N_{\min}} \left(E_{j'}^{\mathrm{U}} - E_{j'}^{\mathrm{R}} \right) - \right. \\ &\quad \left. - \sum_{i'=1}^{N_{\max}} \sum_{j'=2}^{N_{\max}} \left(E_{i'}^{\mathrm{R}} - E_{j'}^{\mathrm{R}} \right) \right] \quad . \end{aligned} \tag{3.2}$$

The index i' runs over all maxima in the unrelaxed energy curve and j' covers the minima while the energies are denoted by E^{U} (unrelaxed) and E^{R} (relaxed). $N_{\min}$ ($N_{\max}$) is the number of minima (maxima) encountered along the chosen sliding path such that $N_{\max} = N_{\min} - 1$, as we always start and terminate our path in a minimum of the unrelaxed energy curve for both approaches.

The use of unrelaxed energy curves, where the two bodies slide over each other statically, only adjusting their vertical distance to keep the load constant, is of course a rather crude assumption. However, for the two periodic sliding directions at 0° and 30° of the Cu(111) on Cu(111) sliding system (see also section 3.5) we also carried out more realistic shearing calculations that support our approach. In these calculations we use the same unit cell and drag the uppermost two (fixed) layers in small (~ 0.1 Å) steps in the chosen sliding direction while holding the two bottom-most layers still. At each step the 8 free layers in the middle are allowed to relax and, in contrast to the quasi-static approach, the resulting relaxed configuration is used as input for the next step. This method is only computationally reasonable for short periodic paths and is ill-suited for aperiodic ones, which need very long paths to be considered (see the following sections). The vertical distance between the two fixed regions of the slab was kept constant during these calculations and at the equilibrium distance of the non-sheared slab, i.e. corresponding roughly to zero load. The results for the 0° path are shown in figure 3.8.

In the beginning the energy of the sheared slabs follows the relaxed energy curve from our proposed quasi-static model, but deviates in the vicinity of its first maximum at
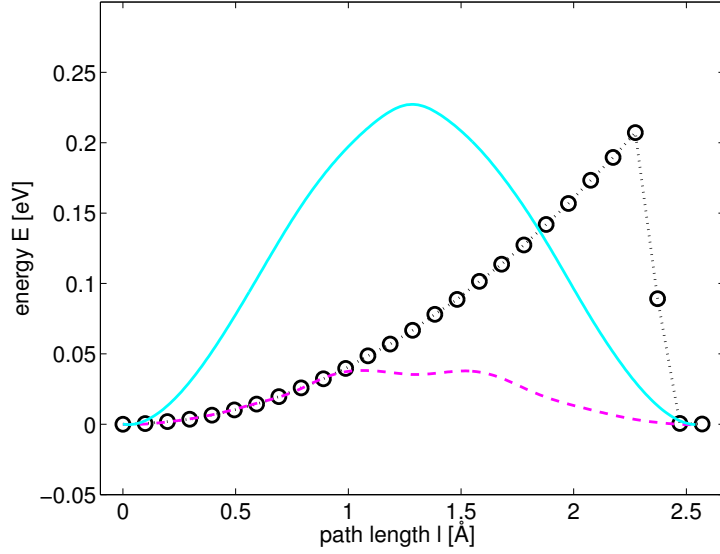
Figure 3.8: A comparison between our friction model and a shearing simulation for the periodic 0° sliding path at zero load for a Cu(111) on Cu(111) sliding system. The entire period is shown. The solid (cyan) line and the dashed (magenta) line give the unrelaxed and relaxed energy curves for the quasi-static model, as seen also in figure 3.7. The black circles are fully relaxed data points of the shearing calculation.

about $l = 1$ Å. The sheared system is not fully relaxing in the total energy minimum but is still pinned in the potential well of the starting position, a common feature in stick-slip sliding. The slip is initiated only at the end of the period, where the built up stain energy of $E_{\text{shear}}(0°) = 207$ meV is dissipated and the system slips into the next minimum. This energy is actually underestimated by $\sim 25\%$ within our proposed quasi-static friction model at $E_{\text{qs}}(0°) = 156$ meV although we include contributions of the unrelaxed energy curve (see figure 3.7 and equation (3.2)). In contrast, applying the model by Zhong and Tománek (see section 1.2.1) to the relaxed energy curve underestimates the dissipated energy while shearing by more than 80% at $E_{\text{ZT}}(0°) = 38$ meV.

For the 30° (see figure 3.9) sliding direction the situation is different, as the shearing appears to become periodic only after the first slip with a much shorter period than in our quasi static model. Three small slips of roughly equal size happen during a sliding distance of ~ 4.2 Å (from $l \sim 2.0$ Å to $l \sim 6.2$ Å in figure 3.9), which is comparable to one period in our quasi-static model of ~ 4.4 Å where one small and one large slip occur. While the predicted slipping process is different the energetics are in excellent agreement, with $E_{\text{qs}}(30°) = 286$ meV being lost per period in our model and $E_{\text{shear}}(30°) = 287$ meV dissipated in three slips during shearing. Using the model of Zhong and Tománek underestimates the energy severely again at $E_{\text{ZT}}(30°) = 104$ meV.
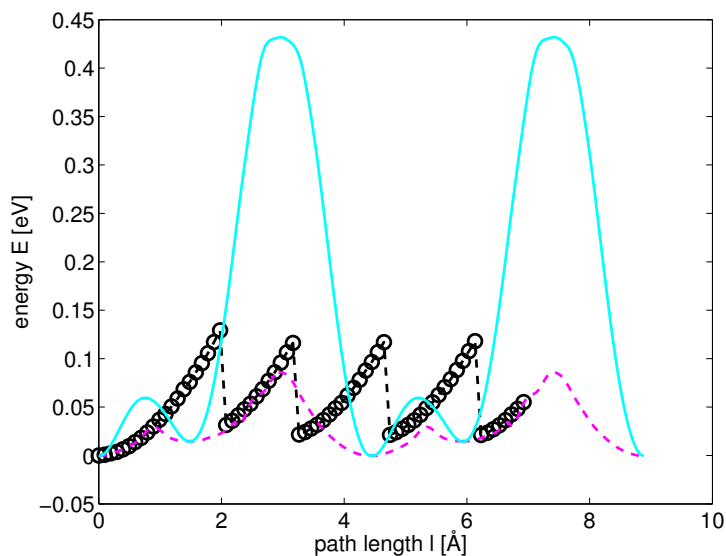
Figure 3.9: A comparison between our friction model and a shearing simulation for the periodic 30° sliding path at zero load for a Cu(111) on Cu(111) sliding system. Clearly the initial state is not reached again by the shearing calculation (black circles). The solid (cyan) line and the dashed (magenta) line give the unrelaxed and relaxed energy curves for the quasi-static model, as seen also in figure 3.7.

This good agreement of our quasi-static results with the shearing calculations adds a convincing argument in favor of our model and justifies the seemingly *ad-hoc* application of unrelaxed energy surfaces. As the periodic paths that were tested in this way turn out to bound the friction force from below and above (see sections 3.5 to 3.7), it is reasonable to assume that the method will also yield plausible results for aperiodic paths for which the shearing calculations become extremely time consuming. The shearing was carried out at constant distance and not constant load, which would allow to adjust their distance. This would decrease the pinning and lower the energy barrier, bringing E_{shear} even closer to the values obtained with our quasi-static model. We want to mention that our energies are calculated at $0\,\mathrm{K}$; finite temperature would of course reduce the effective potential corrugation so that a slip process could occur earlier, but this is equally true for both the quasi-static and shear model.

3.3 Friction of a flat Aluminium and Titanium surfaces with constant distance.

The sliding of two aluminium slabs over each other where the first in the series of calculations carried out in the framework of our quasi-static friction model described in section 3.2. They served the purpose of getting a feeling for the feasibility of the model and to determine if reasonable results could be computed with 6 layer thick 1×1 slabs. The first calculations on titanium followed shortly after with the same methods. Since the spline interpolation between the data points was not implemented at this point, the force curves where more choppy than desired and the method lacked another important aspect at this point. This was the notion of keeping the loading force constant during sliding, meaning that the distance between the slabs needs to vary according to the lateral position. The problem was solved subsequently and is discussed in section 3.4. As this solution was found after the initial calculations on aluminium and titanium where finished, the results presented in this section where computed not for sliding under constant load but with constant distance between the outermost layers of both slabs.

An initial idea was to investigate the possibility to model incommensurate contacts with the quasi-static grid method, inspired by the work of Hirano, Shinjo, Dienwiebel and others on superlubricity [151–153, 155–157]. So we did not only investigate the equilibrium crystal structures (fcc Al on fcc Al and hcp Ti on hcp Ti) but also looked at hcp Al(0001) on hcp Al(0001) as well as hcp Ti(0001) on bcc Ti(110). This was done to probe the influence of sliding between imperfectly aligned crystal structures, but as we still used a 1×1 unit cell, the surfaces where still strictly commensurate. This endeavor was later deemed of secondary importance to the further development of the quasi-static grid model, as the modeling of incommensurate contacts was thought to be only reasonable for large unit cells and using some sort of flakes, given the periodic boundary conditions in *VASP*.

Results that could be obtained with the limited model include the vanishing net reaction forces for aperiodic paths and the ordering of friction forces depending on sliding direction as seen in figure 3.10. For sliding of hcp Ti(0001) over bcc Ti(110), the bcc slab had to be completely frozen to prevent relaxation into a hcp configuration. This results in less relaxations and is responsible for much of the reduction in friction observed here. The 30° periodic sliding direction leads to the highest friction in all cases, a trend that we will see repeated in the following more advanced calculations. The aperiodic directions 10° and 45° give intermediate values, while the periodic 0° path shows the lowest friction forces except for sliding of hcp Ti(0001) on hcp Ti (0001).

For subsequent calculations it was decided to substitute copper for aluminium, as it
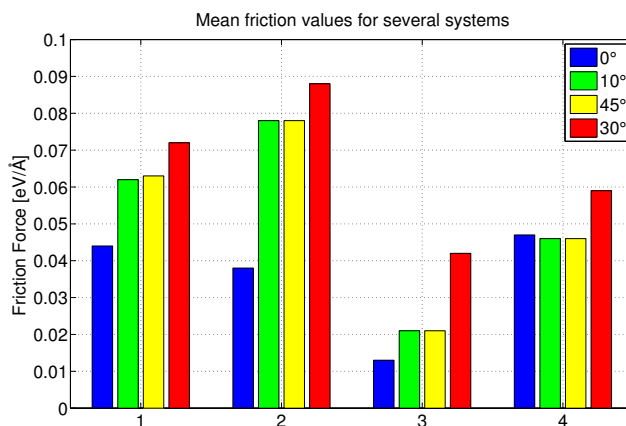
Figure 3.10: A comparison of the mean friction force for (1) fcc Al(111) on fcc Al(111), (2) hcp Al(0001) on hcp Al(0001), (3) hcp Ti(0001) on bcc Ti(110), and (4) hcp Ti(0001) on hcp Ti (0001). Results are calculated for constant distance sliding using equation 3.1.

has more use in tribological applications.

3.4   Keeping the load constant

After the initial calculations presented in section 3.3, we extended our model (see section 3.2) to allow for sliding under a constant loading force. This is necessary to model experimental conditions, investigate the dependence of the friction force on load and to ultimately calculate a coefficient of friction.

Keeping the load constant means that the distance between the slabs needs to adapt, as the repulsive forces between the slabs depend on the lateral positions. To this end the distance between the slabs is varied in several steps (6–10, depending on the material) for each of the 100 grid-points, recording the respective volume V and the total energy of the relaxed cell E^{R} which are fitted to a second order polynomial. The uniaxial pressure on the cell can now be evaluated by calculating the first derivative of E^{R} with respect to V at each lateral position, namely $p = -\partial E^{\mathrm{R}} / \partial V$. The corresponding loading force L is then obtained by multiplying the pressure with the cross-section area A of the unit cell, $L = p A$. Choosing a load (given derivative of the energy vs. volume functions) we recalculate the respective energies and forces at each of the 100 grid points and obtain energy surfaces at that given constant load. The method is visualized for one lateral point in figure 3.11. Employing this process, which was also used in a very similar way by Cahangirov et al. [25], we construct quantum mechanical energy- and force-maps for the quasi-static sliding system under constant load, both with and without relaxation of

atoms.
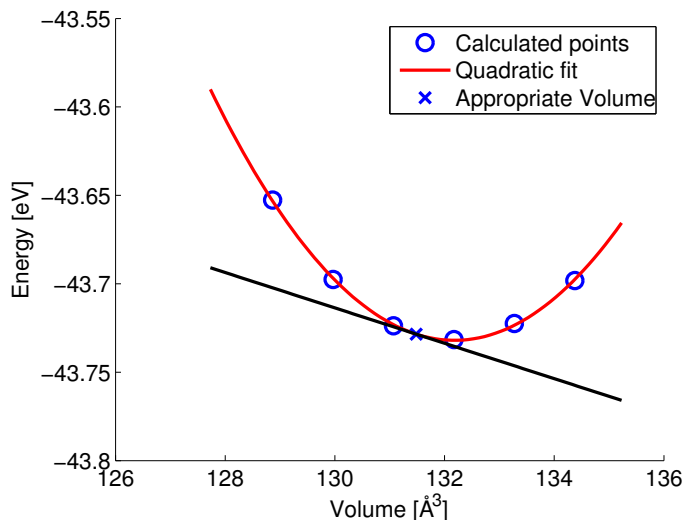
Figure 3.11: Visualization of the process that keeps the load constant for each of the 100 lateral grid points. The black line represents the chosen pressure (derivative of the energy with respect to the volume) for the next calculations.

3.5 Copper

The fcc Cu(111) on fcc Cu(111) cell described in this section was the first sliding system to be investigated with the full method presented in section 3.2 using sliding under constant load as described in section 3.4 and utilizing both equations 3.1 and 3.2 to calculate the frictional response. Copper was chosen for the following reasons: i) commensurate sliding of a Cu(111) tip on Cu(111) was previously found to exhibit wearless atomic stick-slip motion, both in molecular dynamics simulations [170, 171], and experiments in ultra-high vacuum [172]. This is in contrast to results for Cu(100) on Cu(100) where both plastic deformations and wear play an important role [170, 173]. ii) Garvey et al. showed in a recent series of papers on KCl sliding on Fe(100) that the investigation of shearing interfaces and the prediction of friction coefficients for such systems require very high accuracy in the calculated energies [21–23]. The Vienna Ab-Initio Simulation Package *VASP* [45, 82–84] applied to the copper system seems to be ideally suited for our study. The Projector Augmented Wave (PAW) code [87, 140] is much more accurate as for example embedded atom potentials but not as computationally expensive as highly accurate full-potential linearized augmented plane-wave (FLAPW) method which is needed sometimes for systems where the local bonding environment changes significantly [21]. We found that, while the

69

considered system is small enough that the large number of calculations needed for the construction of accurate energy surfaces for various loads is still feasible, it is also realistic enough to work as a proof of concept for the proposed scheme to calculate friction forces on the nanoscale. It has to be pointed out, however, that this model is not intended to simulate a macroscopic copper on copper system which would feature multiple grains, oxidation, impurities, and other imperfections. The aim is rather to study a model for dissipative sliding under idealized and controlled conditions.

The full simulation box consists of 12 atoms using a bulk lattice constant $a = 3.634\,\text{Å}$ determined from DFT equilibration, cf. in experiments $a = 3.615\,\text{Å}$ [147]. Due to the inherent periodicity of our supercell, a vacuum layer of about $15\,\text{Å}$ is included on top of the upper slab to decouple the periodically repeated simulation cell in the z direction. This 12 layer thick arrangement is comparable to a number of previous studies using *ab-initio* methods [21–23, 25, 27, 32, 35, 174–176], and is sufficiently thick to approximate the elastic properties of copper while retaining computational efficiency. As already mentioned all energies and forces are calculated with the DFT package *VASP* using the PAW method with an energy cut-off of $341.5\,\text{eV}$. For the exchange and correlation potential, the Generalized Gradient Approximation (GGA) in the version devised by Perdew, Burke and Ernzerhof (PBE) is applied [58]. As the strong chemical bonds in copper are well described with PBE and our results rely on the calculation of total energies, there is no need to explicitly consider van der Waals forces or meta-GGA. The Brillouin zone sampling is performed on a Γ-centered $24 \times 24 \times 1$ k-grid ensuring a total energy convergence better than $1\,\text{meV}$ per simulation cell. Atomic relaxations were converged to $0.1\,\text{meV}$ in total energy, with each electronic calculation being converged to $0.01\,\text{meV}$.

3.5.1 Friction versus load

All averages presented in this section where calculated from sliding paths of $1\,\mu\text{m}$ length to get reliable values for the constitutive system parameters and to make sure that in the case of quasi aperiodic paths the whole unit cell becomes sampled.

For both definitions of the mean friction force, $F^{(1)}$ and $F^{(2)}$, we observe an exponential friction law along all path directions, see Fig. 3.12, given by

$$F(L) = F_0 \exp\left(\frac{\mu}{F_0}L\right) \quad . \tag{3.3}$$

This result can be traced back to the exponential form for the binding energy in transition metals e.g. as given by Pettifor [177]. In a very general way the energy of bond breaking follows the *universal binding energy relation* (UBER) which also shows an exponential dependence on distance [178] which in our case depends linearly on load.
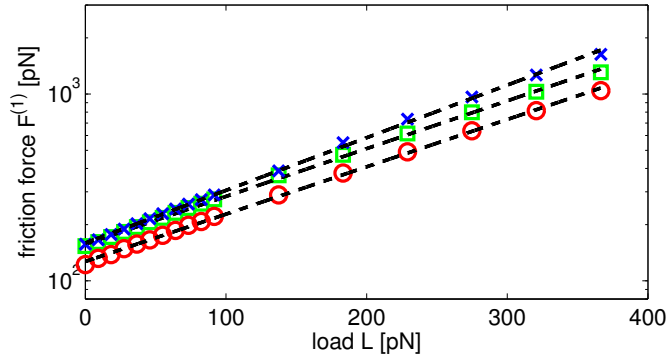
Figure 3.12: Semi-logarithmic plot of the friction force $F^{(1)}$ versus load L for the slip plane of fcc Cu(111). Both periodic paths 0° (red circles) and 30° (blue crosses) are shown alongside the quasi aperiodic 10° path (green squares) which serves as a prototype for all other quasi aperiodic paths. The dashed black lines are linear fits.

The form of the exponent in equation (3.3) incorporates the coefficient of friction (COF) μ. Expanding equation (3.3) in a Taylor series around $L = 0$ we retrieve a kinetic friction law of Derjaguin-form [7, 165]: linear in load L plus the Derjaguin-offset F_0,

$$F(L) = F_0 + \mu L + \mathcal{O}\left(L^2\right) \quad . \tag{3.4}$$

This behaviour is well known in lubricated systems where the offset F_0 is attributed to adhesion resulting from the lubricant, see e.g. Refs. 112, 165. In our dry system the strength of the adhesion, which for frictional purposes acts like an internal load L_0, can be estimated by simply lowering one slab down onto the other and registering the forces on the surface atoms. The resulting internal load L_0 is the maximum in these force curves depending on the lateral positions of the slabs. It ranges between 0.8 nN and 1 nN which is of the same order of magnitude as the maximum applied external loads. Of course the approximation of the exponential law with this linear expansion is only valid in the low load regime. For averaged values of all aperiodic paths the relative error reaches 10% at a load of 90 pN which corresponds to a pressure of 1.6 GPa and should be regarded as the uttermost limit for the Taylor expansion. This low load regime is discussed in more detail in section 3.5.3.

While all quasi aperiodic paths investigated for sufficiently long path lengths converge to the same friction force, there is a clear difference with respect to periodic ones, see Figs. 3.12 and 3.14. As expected the 30° path exhibits the largest friction as for each period it traverses the global maximum of the unrelaxed energy surface created by the on-top position of the contact atoms. This is in contrast to the 0° path, which shows the least friction force at zero load and also the slowest increase with rising load.

Both $F^{(1)}$ and $F^{(2)}$ lead to an exponential friction law, however, the calculated values of the Derjaguin-offset F_0 and the COF μ, while showing the same trend, differ slightly (see Tab. 3.1). However, this is not surprising given the two different approaches, see equations (3.1) and (3.2). Plotting both friction forces versus load curves for a given sliding path, one finds that $F^{(1)}$ and $F^{(2)}$ do agree well in the low to medium load regime while for loads larger than $L = 150\,\mathrm{pN}$ higher deviations occur, as seen in Fig. 3.13. We attribute this discrepancy to the increasing influence of the reaction forces for large loads which are not considered in the calculation of $F^{(1)}$, but play a role in the dissipation mechanism and hence enter implicitly in $F^{(2)}$.
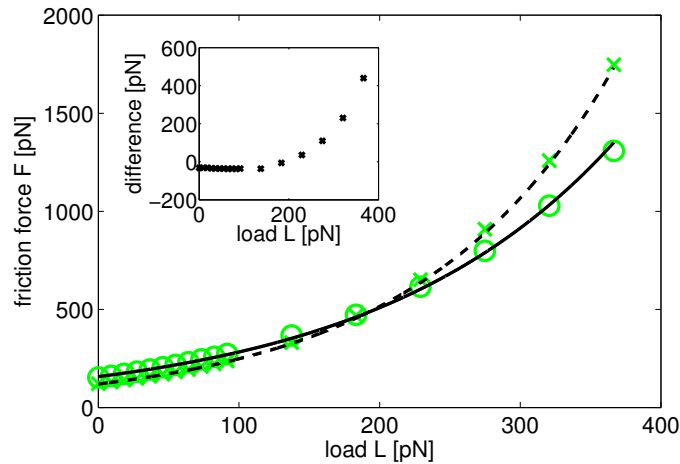
Figure 3.13: Friction forces $F^{(1)}$ (green circles) and $F^{(2)}$ (green crosses) versus load L for fcc Cu(111) slabs sliding along a 10° path. The insert (black crosses) shows the difference $F^{(2)} - F^{(1)}$. At low to medium loads the difference is constant and corresponds to the disparity of the friction at zero load F_0

3.5.2 Influence of path length

In Fig. 3.14 the reason why long paths are required ($\sim 1\,\mu\mathrm{m}$) becomes apparent. While the friction force for the 0° path (red circles) shows essentially no dependence on the length of the path, for the 30° one (blue crosses) the friction force oscillates in the beginning before converging to a constant value. This is due to the fact that the summation in equations (3.1) and (3.2) terminates at the last minimum encountered. For 0° this happens always after a full period, while along the 30° direction one has two minima per period (fcc and the hcp position), so that the total friction force average depends on the termination of the summation. It is obvious that with increasing path length the influence of the termination point becomes less and less important for the calculation of the average. In

the quasi aperiodic case, where a short path length would only sample fractions of the energy landscape, it is evident that the friction force only converges for sufficiently long paths.
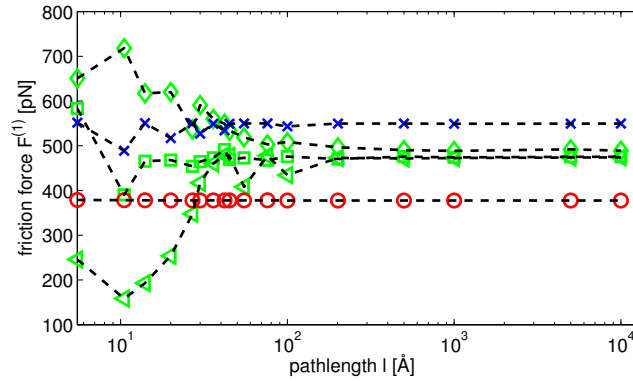
Figure 3.14: Plot of the mean friction force $F^{(1)}$ versus the path length l for a load $L = 183\,\text{pN}$. Both periodic paths $0°$ (red circles) and $30°$ (blue crosses) are shown alongside three quasi aperiodic ones (green diamonds for $-10°$, green triangles for $3°$ and green squares for $10°$). Dashed lines are plotted to guide the eye.

3.5.3 Low load regime

The largest load considered in our simulations is $367\,\text{pN}$, given the cross-section area of the unit cell $5.7\,\text{Å}^2$, this is equivalent to a static pressure of $6.4\,\text{GPa}$ which is well beyond any realistic technological applications. Thus, it is important to analyze the low load regime of up to $90\,\text{pN}$ ($1.6\,\text{GPa}$) separately. In this range the exponential law can be approximated reasonably well by a linear relation $F_{\text{lin}}(L) = F_0 + \mu_{\text{lin}}L$ so that the COF μ_{lin} is given by the slope, see Tab. 3.1 and figure 3.15. It should be noted that the μ_{lin} obtained in this manner are systematically larger than the values of μ, since the slope of a linear fit to a segment of an exponential function is always steeper than the tangent of the function at the beginning of the segment. Since the ultimate tensile strength for annealed copper is approximately $160\,\text{MPa}$ [179] an uniaxial pressure of more than $1.6\,\text{GPa}$ will already deform the sample. However, it remains computationally feasible to study extremely high loads because the periodic boundary conditions imposed on our simulations restrict the horizontal movement of the atoms and the fcc (111) symmetry of the sample is preserved at all times.
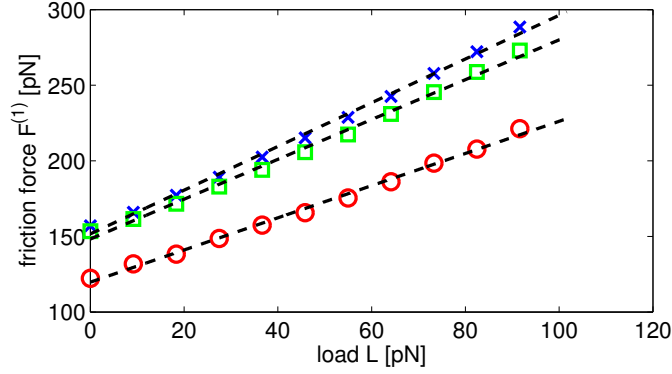
Figure 3.15: Plot of the friction force $F^{(1)}$ versus load L for the slip plane of fcc Cu(111). Both periodic paths 0° (red circles) and 30° (blue crosses) are shown alongside the quasi aperiodic 10° path (green squares) which serves as a prototype for all other quasi aperiodic paths. The dashed black lines are linear fits.

	$F_0^{(1)}$[pN]	$F_0^{(2)}$[pN]	$\mu^{(1)}$	$\mu^{(2)}$	$\mu_{\text{lin}}^{(1)}$	$\mu_{\text{lin}}^{(2)}$	μ_{exp}
0°	127	101	0.74	0.60	1.06	0.87	-
30°	159	109	1.03	0.91	1.45	1.46	-
aperiodic	157 ± 4.4	121 ± 2.7	0.94 ± 0.06	0.88 ± 0.05	1.33 ± 0.14	1.25 ± 0.04	$0.78^a, 0.92^b$

Table 3.1: Derjaguin-offset values F_0 and coefficients of friction μ corresponding to the friction forces $F^{(1)}$ and $F^{(2)}$, see equations (3.1) - (3.3). The constitutive system parameters for the aperiodic directions are given by the average over all examined quasi aperiodic paths. Experimental data for nanocrystalline (a) and annealed (b) copper are taken from Ref. 180.

3.5.4 Coefficients of friction

Depending on direction and method we obtain a COF between $0.6 - 1.46$ which is one order of magnitude larger compared to the MD study by Sørensen et al. [170]. This large difference can be explained at least in part by the small contact size in Sørensen's work that leads to slips mediated by a dislocation mechanism which is suppressed in our model due to the periodic boundary conditions. In 2006 Zhang et al. [180] experimentally determined the friction coefficient for dry copper to be $\mu_{\text{exp}}^{\text{nc}} = 0.78$ (nanocrystalline sample) and $\mu_{\text{exp}}^{\text{an}} = 0.92$ (annealed sample). These values were found in the zero wear regime for a load of $\sim 5\,\text{N}$. The obtained COFs in the low load regime agree fairly well with our values for aperiodic sliding ($\mu^{(1)} = 0.94 \pm 0.06$, $\mu^{(2)} = 0.88 \pm 0.05$).

3.6 Titanium

After investigating the sliding properties of a pair of dry fcc Cu(111) surfaces, hcp Ti(0001) was studied. The two close packed structures fcc and hcp are different only by layer stacking, with ABCABC. . . stacking for the cubic case and ABAB. . . stacking in the hexagonal phase. Of course the materials copper and titanium have more differences, including the significantly larger Vickers micro-hardness of titanium at 1.96 GPa [181], compared to the value of 0.7 GPa [180] for copper. The bulk lattice parameters of titanium were calculated as $a = b = 2.93$ Å and $c = 4.64$ Å, in good agreement with the experimental values $a_{exp} = b_{exp} = 2.95$ Å and $c_{exp} = 4.67$ Å [147]. The calculations where performed on a $24 \times 24 \times 1$ k-mesh, with a smearing of 0.4 eV using the first order method of Methfessel and Paxton [141]. This value is rather large, but benchmark calculations revealed that results are consistent with much lower values and the advantage of the larger smearing regarding convergence speed is considerable.

The initial calculations on a 10×10 lateral mesh produced puzzling results with rather strange dips in the unrelaxed energy landscape. This was thought to be an effect of imperfectly calculated pressures, as the initial energy versus volume curves where fitted to unevenly distributed data, used from calculations of sliding with constant distance (see section 3.3). After discovering that some calculations had not been converged fully, a decision was made to redo all calculations on a 16×16 lateral grid and to use new and evenly spaced points for the fitting of the energy versus volume curves to calculate the correct volumes to keep the load constant. This had the additional value of comparing the quality of the results on a 10×10 grid with those obtained for a 16×16 grid, which increases the computational effort by more than 150%. Interestingly, the characteristic dips in the shoulders of the main peak of the unrelaxed energy curves where still present for the new set of calculations (see figure 3.16) and where thus interpreted as physically correct features. In section 3.6.5 a more detailed analysis of the matter is given which hints to a lattice instability due to a Kohn anomaly. Unfortunately this also means that all of the following results for the titanium sliding system have to be considered as preliminary.

3.6.1 Friction versus load

As in the case of copper before, the presented results are averages over 1 μm long sliding paths and have been fitted with the exponential friction law presented in equation 3.3 as well as with the linear Taylor expansion (see equation 3.4).

It is evident that the exponential fit is much less accurate in the case of titanium compared to copper (see figure 3.17). Also, even though higher loads have been examined,
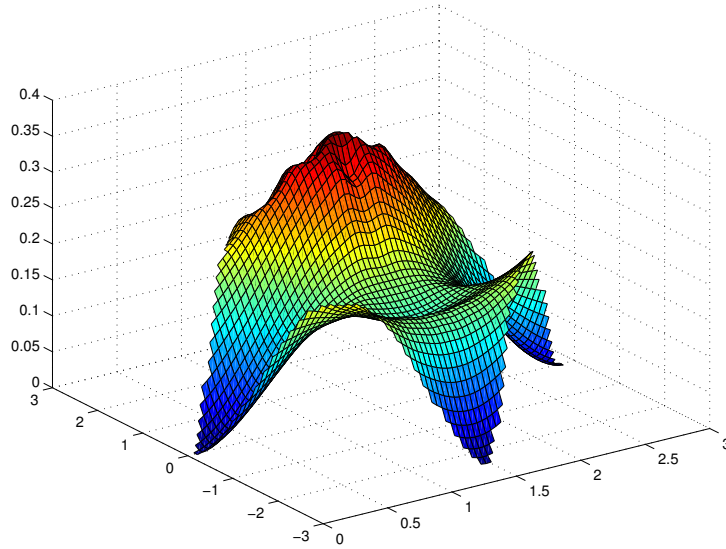
Figure 3.16: Static energy landscape of the hcp(0001) on hcp(0001) Ti sliding system at zero load. Note the depressions in the shoulders of the main peak.
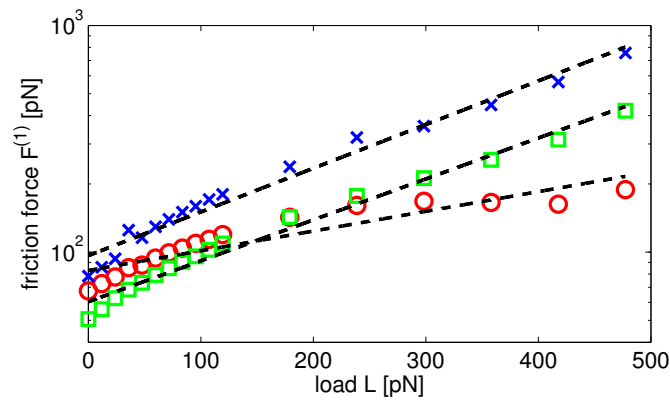
Figure 3.17: Semi-logarithmic plot of the friction force $F^{(1)}$ versus load L for the slip plane of hcp Ti(0001). Both periodic paths 0° (red circles) and 30° (blue crosses) are shown alongside the quasi aperiodic 10° path (green squares) which serves as a prototype for all other quasi aperiodic paths. The dashed black lines are linear fits.

the overall friction force ($F_{\max}^{(1)}$(Ti) $\simeq 757\,\mathrm{pN}$, $F_{\max}^{(2)}$(Ti) $\simeq 820\,\mathrm{pN}$) is much lower than for copper ($F_{\max}^{(1)}$(Cu) $\simeq 1633\,\mathrm{pN}$, $F_{\max}^{(2)}$(Cu) $\simeq 2162\,\mathrm{pN}$), as was to be expected from the much harder and stiffer contact. It is also interesting to note that the friciton force at zero load, F_0, is actually higher for the $0°$ path than for the $10°$ path, although the expected hierarchy is restored for higher loads, as seen in figure 3.17.
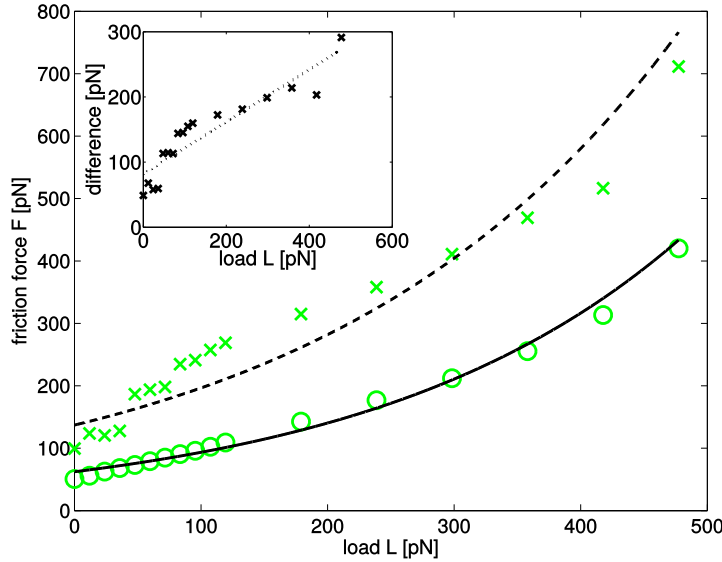
Figure 3.18: Friction forces $F^{(1)}$ (green circles) and $F^{(2)}$ (green crosses) versus load L for hcp Ti(0001) slabs sliding along a $10°$ path. The insert (black crosses) shows the difference $F^{(2)} - F^{(1)}$. The discrepance is rising rather unpredictably but linearly overall.

In figure 3.18 we see that the friction force $F^{(2)}$ oscillates a lot around the fitted exponential function. Contrarily to copper, where the difference between $F^{(1)}$ and $F^{(2)}$ was constant for low loads, in the case of titanium it grows irregularly but overall linearly. While the absolute difference is lower for the maximal load on the $10°$ path, the relative difference, with 41%, is considerably larger than for copper with 25%.

3.6.2 Influence of path lenght

Analyzing the path length dependence once again emphasizes the need for long path lengths to ensure convergence. However, the differences between $F^{(1)}$, see figure 3.19a, and $F^{(2)}$, see figure 3.19b, are also clearly revealed. While the overall ordering of the friction forces from low ($0°$) over intermediated (aperiodic) to high ($30°$) are consistent for the selected load, the incommensurate sliding directions show approximately the same friction force as the $0°$ path for $F^{(1)}$ but they give the same result as the $30°$ path for $F^{(2)}$.
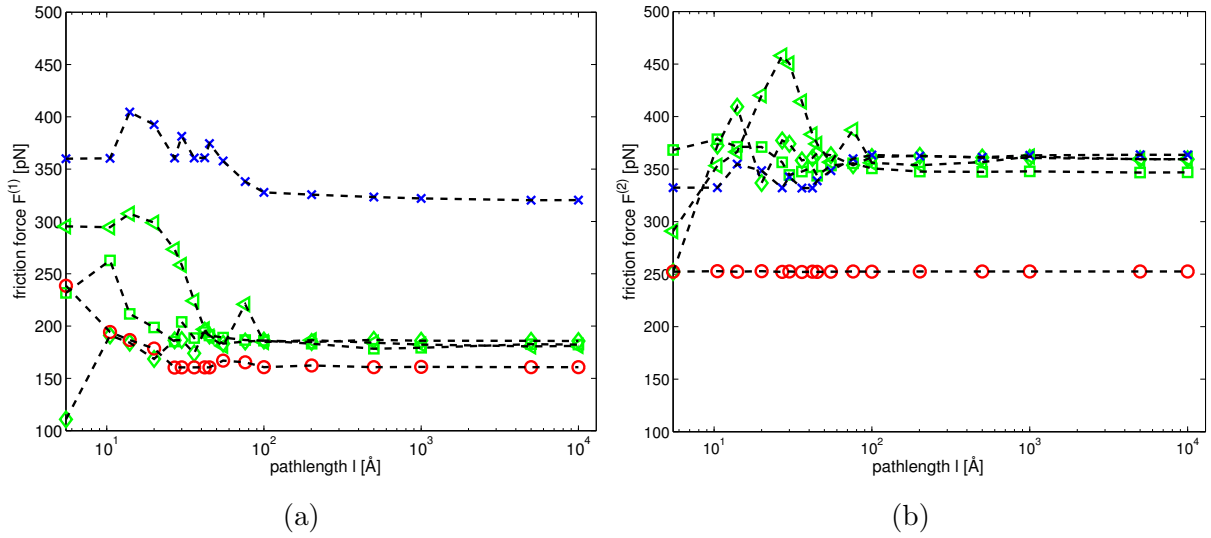
Figure 3.19: Plot of the mean friction force $F^{(1)}$ (a) and $F^{(2)}$ (b) versus the path length l for a load $L = 239\,\text{pN}$. Both periodic paths $0°$ (red circles) and $30°$ (blue crosses) are shown alongside three quasi aperiodic ones (green diamonds for $-10°$, green triangles for $3°$ and green squares for $10°$). Dashed lines are plotted to guide the eye.

3.6.3 Low load regime

In contrast to the exponential fits in section 3.6.1, the linear fits of the low load regime are excellent in the case of $F^{(1)}$ as seen in figure 3.20a. It is worth noting, that in this regime the aperiodic paths show lower frictional forces than the $0°$ path, although the slope of the $0°$ direction is lower, corresponding to a lower coefficient of friction. The data of $F^{(2)}$, as seen in figure 3.20b, are much more scattered than for $F^{(1)}$, but the friction forces for the periodic $0°$ path are lowest again.

3.6.4 Coefficients of friction

Considering the rather scattered data and mediocre fits, it is not surprising that the resulting coefficients of friction are not as internally consistent as in the case of copper (see table 3.1). However, with $\mu(0°) < \mu(\text{ap}) < \mu(30°)$ for all calculation variants, the expected trend is generally observed. This is not the case for the absolute friction force, as seen in figures 3.17 and 3.20a, because the low Derjaguin offset $F_0^{(1)}$ for aperiodic paths leads to lower friction compared to the $0°$ direction. Furthermore, the linear fits to the low load data lead to larger coefficients of friction than the values extracted from the Taylor expansion of the exponential fits, indicating that the exponential law is not reproduced well in the low load case.
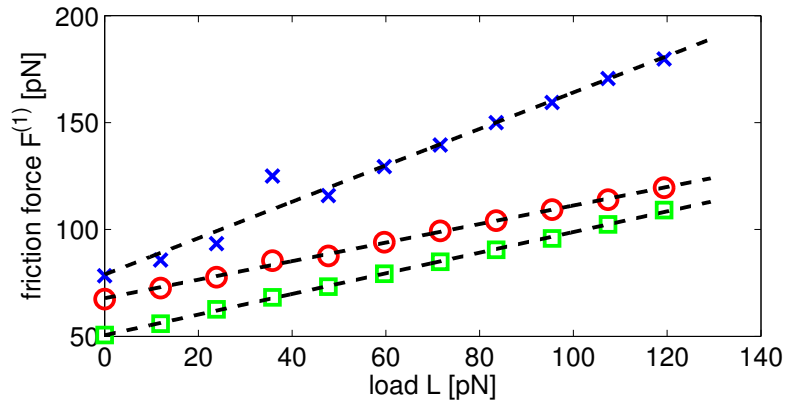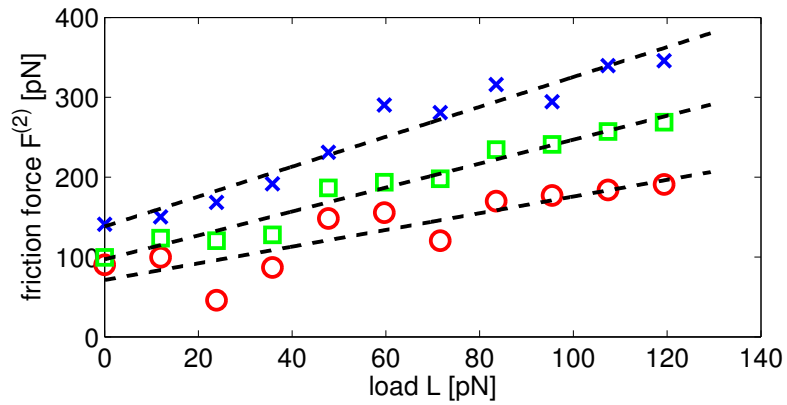
Figure 3.20: Plot of the friction force $F^{(1)}$ (a) and $F^{(2)}$ (b) versus load L for the slip plane of hcp Ti(0001). Both periodic paths 0° (red circles) and 30° (blue crosses) are shown alongside the quasi aperiodic 10° path (green squares) which serves as a prototype for all other quasi aperiodic paths. The dashed black lines are linear fits.

	$F_0^{(1)}$[pN]	$F_0^{(2)}$[pN]	$\mu^{(1)}$	$\mu^{(2)}$	$\mu_{\text{lin}}^{(1)}$	$\mu_{\text{lin}}^{(2)}$	μ_{exp}
0°	83	103	0.17	0.32	0.43	1.05	-
30°	96	196	0.43	0.59	0.85	1.87	-
aperiodic	62 ± 4.5	134 ± 37.6	0.26 ± 0.02	0.48 ± 0.08	0.49 ± 0.02	1.41 ± 0.28	-
Ref. [182][a]	-	-	-	-	-	-	0.65–0.68
Ref. [183][b]	-	-	-	-	-	-	0.4–0.8
Ref. [184][c]	-	-	-	-	-	-	0.3–0.6

Table 3.2: Derjaguin-offset values F_0 and coefficients of friction μ corresponding to the friction forces $F^{(1)}$ and $F^{(2)}$, see equations (3.1) - (3.3). The constitutive system parameters for the aperiodic directions are given by the average over all examined quasi aperiodic paths. Experimental data include sliding of fine grained titanium in air or argon (a), of the (0001) basal plane of single crystal titanium in vacuum (b), and of coarse and fine grained titanium under multiple conditions (c).

Several experimental studies on the friction of pure titanium could be found in the literature [182–184], with the work of Buckley (Ref. 183) matching our simulation conditions best. They examined the sliding of a titanium single crystal, orientated in the (0001) and (10$\bar{1}$0) plane, against a poly crystalline titanium disc in vacuum (10^{-9} Torr). They conclude that the primary slip plane for hcp titanium is the prismatic (10$\bar{1}$0) plane, which shows lower shear stress and leads to a lower friction coefficient at low loads. At higher loads, μ of both the prismatic and the basal plane converge to a value of ~ 0.8, indicating recrystallization at the sliding interface. It is therefore prudent to compare our results to the results of Buckley at low loads, where the basal plane shows a coefficient of friction between 0.4 and 0.6. This is in reasonable agreement with our results presented in table 3.2.

3.6.5 Analyzing the unrelaxed energy surfaces

As mentioned previously, rather strange dips where found in the unrelaxed energy landscape which are not easily explained by physical intuition. Furthermore the large scattering of data and results described in the previous sections hint to problems in the computations. To analyses this behavior several additional points were examined with great care along a straight line across the main peak, recalculating every step of the process (see figure 3.21).

After seven initial calculations per point at different volumes to facilitate the load calculations the unrelaxed energy was calculated for zero load along the selected line at four times higher resolution than before on the 16×16 grid. Figure 3.22 clearly shows
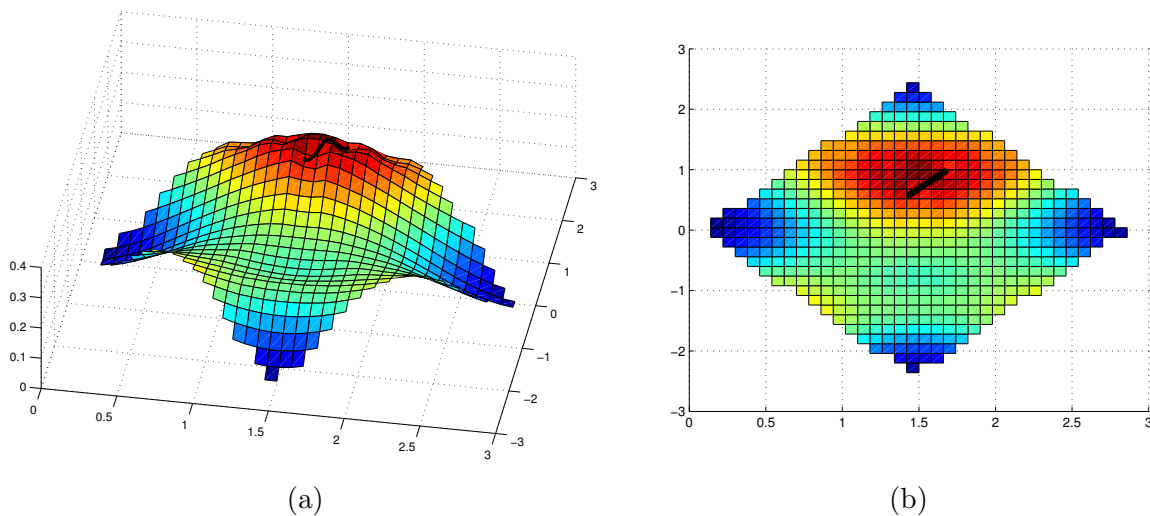
Figure 3.21: Side (a) and top (b) view of the static energy landscape of the hcp titanium sliding system at zero load. Along the black line 13 additional points where recalculated from scratch to analyse the depressions in the main peak of the energy landscape.

that the depressions are very localized and form discontinuities in the otherwise smooth energy curve. Substituting the two disruptive points by the average between the both neighboring points (green squares in figure 3.22) leads to a near perfect polynomial shape of second order as indicated by the dashed line.

The occurrence for the non-physical depressions in the energy surface becomes apparent when looking at the energy versus volume plots for the 13 points along the investigated line (see figure 3.23). In contrast to the energy surfaces described before in this section these data are relaxed under the constraint of fixed volume. The fitted quadratic functions for the two critical points are about $0.1 \, \text{eV}$ higher in energy than the rest. The minima of these two parabolas are also shifted to the right to a higher volume. This is the reason for the significantly lower unrelaxed energies at this points, as the slabs are here in the vicinity of an energetically unfavorable on-top position so that a larger distance between them leads to lower energies.

Preliminary attempts to circumvent these possible convergence problems by using other computational parameters and algorithms proved to be unsuccessful, hinting to a deeper problem maybe rooted in symmetry. For the early transition metals there exists a competing phase called the ω phase, which is actually lower in energy for titanium than the investigated hcp configuration. Thus it becomes likely that for those points in space where these discontinuities happen a Fermi surface nesting occurs which leads to a dramatic softening of some elastic constants. This "static" Kohn anomaly [185], could be the reason for the observed discontinuities in the total energy.
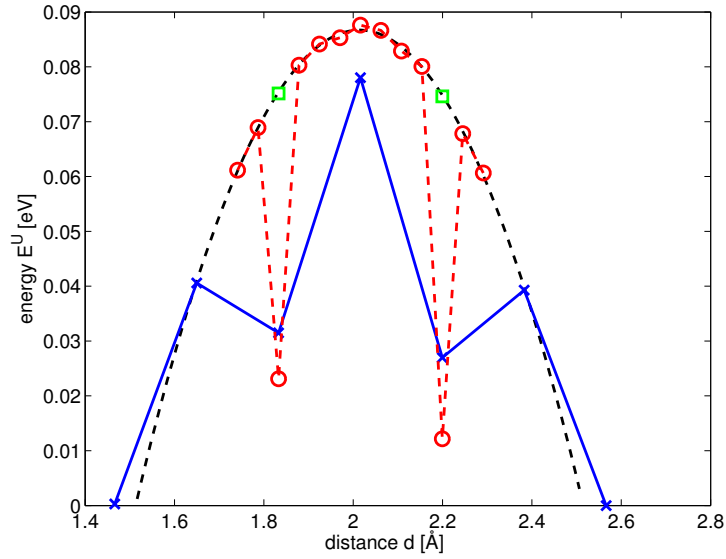
Figure 3.22: Unrelaxed energy E^U along a line traversing the main peak in energy. Blue crosses are data from the original 16×16 grid, red circles are the new calculations also clearly showing the discontinuity. The two green squares are linear interpolations between neighbouring red circles at the discontinuity while the dashed black line is a fitted quadratic function to the new data, substituting the green squares for the red circles at the disruptions.
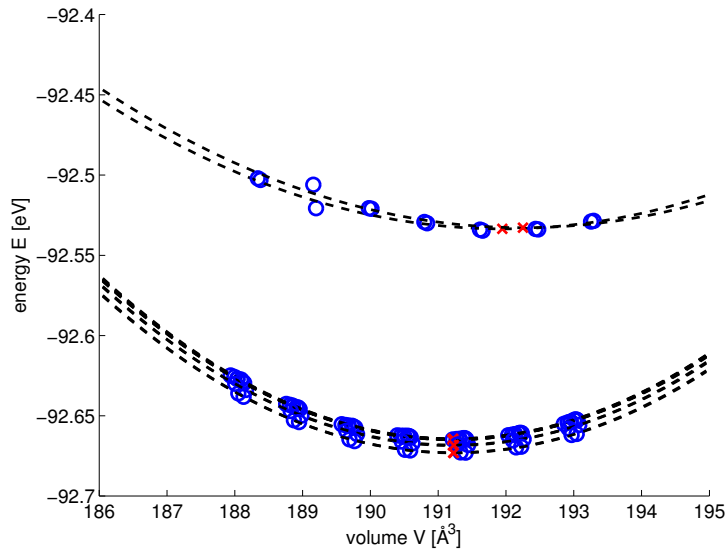
Figure 3.23: Energy versus volume plots (blue circles) for all 13 points along the investigated line. The parabolas (black dashed lines) for the two critical points are higher in energy by more than $0.1\,\text{eV}$ and the volumes corresponding to zero load (red crosses) are larger.

3.7 Zirconium

Zirconium was chosen as a sliding material because it is similar to titanium, where the above mentioned effects lead to inconsistent and unreliable results (see section 3.6.5). It is a 4d transition metal of the 4th group, which locates it directly below titanium in the periodic table. The electron configuration is $[Kr]5s^2 4d^2$, compared to $[Ar]3d^2 4s^2$ of titanium and the crystal structure is also hexagonal close packed. Although zirconium is softer than titanium and has a larger lattice constant, we expect similar results. Literature also suggests that the slip mechanism of zirconium and titanium are equivalent [186].

Bulk relaxations with *VASP* yielded lattice parameters of $a = b = 3.23\,\text{Å}$ and $c = 5.18\,\text{Å}$ which are in excellent agreement to experimental results ($a_{exp} = b_{exp} = 3.232\,\text{Å}$ and $c_{exp} = 5.147\,\text{Å}$ [147]). A $26 \times 26 \times 1$ mesh was used to sample the k-space, with a smearing of $0.2\,\text{eV}$ using the first order method of Methfessel and Paxton [141]. The results presented in this section where obtained on a 10×10 lateral grid for sliding paths of $1\,\mu\text{m}$ length and seven initial volumes where used to fit the parabolas needed to ensure constant load (see section 3.4).

3.7.1 Friction versus load

In contrast to titanium, the friction versus load behavior of zirconium is again well described by the exponential law presented in equation 3.3 as can be seen in figures 3.24 and 3.25. However, for the 0° path, $F_0^{(2)}$ is actually negative. This is obviously incorrect, and results from the fact that the peak in the unrelaxed energy curve for this path is less than twice as high as the relaxed peak for low loads which leads to negative values of $F^{(2)}$ according to equation 3.2. Thus it was necessary to shift all data for the 0° direction up by an arbitrary factor to allow for the fitting of the exponential law. After the fitting, both the data points and the fit where shifted down by the same amount, leading to figure 3.25.

For all directions other than 0°, where $F^{(2)}$ is negative for low loads, both methods to calculate the friction force are very consistent. In figure 3.26 the situation is depicted for the 10° path as an example. Similar to the situation for copper, $F^{(2)}$ initially shows lower friction because $F_0^{(2)}$ is lower, but with increasing load the situation is reversed as reaction forces implicitly contribute to $F^{(2)}$ and are not considered in $F^{(1)}$. As zirconium is considerably stiffer than copper this effect is less pronounced and both methods never differ by more than $\sim 50\,\text{pN}$.
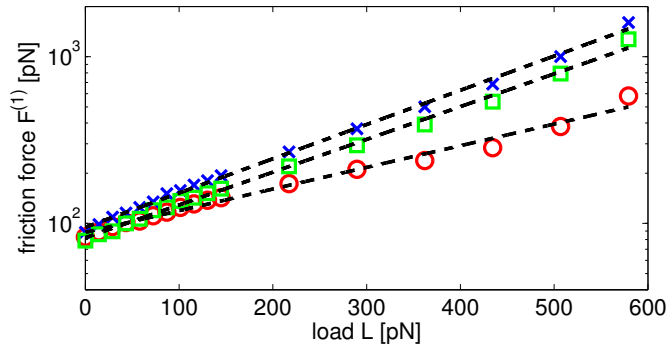
Figure 3.24: Semi-logarithmic plot of the friction force $F^{(1)}$ versus load L for the basal slip plane of hcp Zr. Both periodic paths 0° (red circles) and 30° (blue crosses) are shown alongside the quasi aperiodic 10° path (green squares) which serves as a prototype for all other quasi aperiodic paths. The dashed black lines are linear fits.
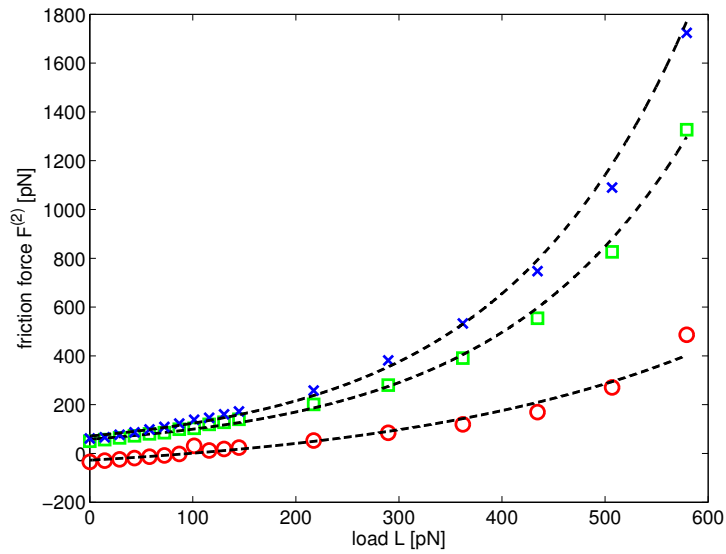
Figure 3.25: Plot of the friction force $F^{(2)}$ versus load L for the basal slip plane of hcp Zr. Both periodic paths 0° (red circles) and 30° (blue crosses) are shown alongside the quasi aperiodic 10° path (green squares) which serves as a prototype for all other quasi aperiodic paths. The dashed black lines are exponential fits. All data points for the 0° path (red circles) have been shifted to positive values before fitting to keep all coefficients real. The results have been shifted down again.
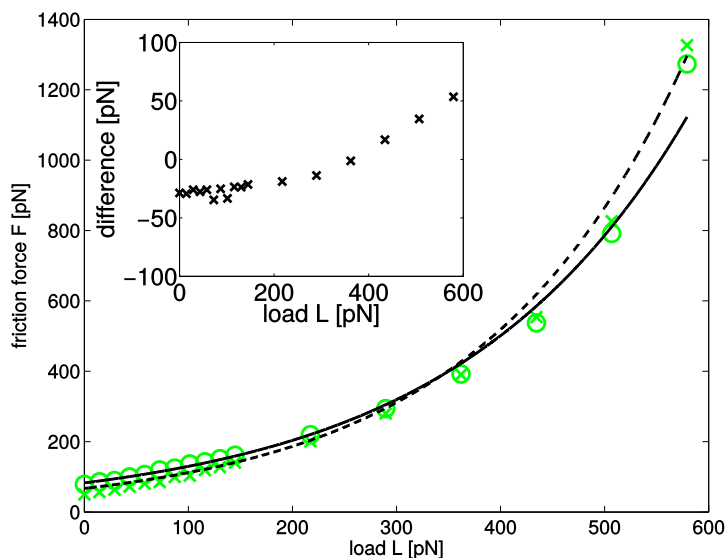
Figure 3.26: Friction forces $F^{(1)}$ (green circles) and $F^{(2)}$ (green crosses) versus load L for hcp Zr(0001) slabs sliding along a 10° path. The insert (black crosses) shows the difference $F^{(2)} - F^{(1)}$. The agreement of $F^{(1)}$ and $F^{(2)}$ is excellent over the whole range of loads with a maximum difference of $\sim 50\,\mathrm{pN}$.

3.7.2 Influence of path length

Generally good convergence of the friction forces is reached after about $500\,\text{Å}$ for the zirconium sliding system as can be seen in figure 3.27. The agreement of both methods is good, although for $F^{(2)}$ the spread for the aperiodic directions is higher and the friction force for the 0° direction is too low (see figure 3.27b), as was already discussed in section 3.7.1.

3.7.3 Low load regime

The linear fits to the low load regime shown in figure 3.28 are once again of good quality. Only one data point for the 0° direction of $F^{(2)}$ deviates significantly from the linear trend, but as $F^{(2)}(0°)$ is systematically too low anyway, this should not be of great concern. As $F_0^{(1)}(0°)$ is once again higher than $F_0^{(1)}(\mathrm{ap})$, the linear curves cross over at a load of about $45\,\mathrm{pN}$, but the slope, and thus the coefficient of friction, is lower for the 0° direction.

3.7.4 Coefficients of friction

The coefficients of friction given in table 3.3 show excellent agreement between $F^{(1)}$ and $F^{(2)}$. As previously mentioned, data for $F_0^{(2)}$ are untrustworthy, especially for the 0°
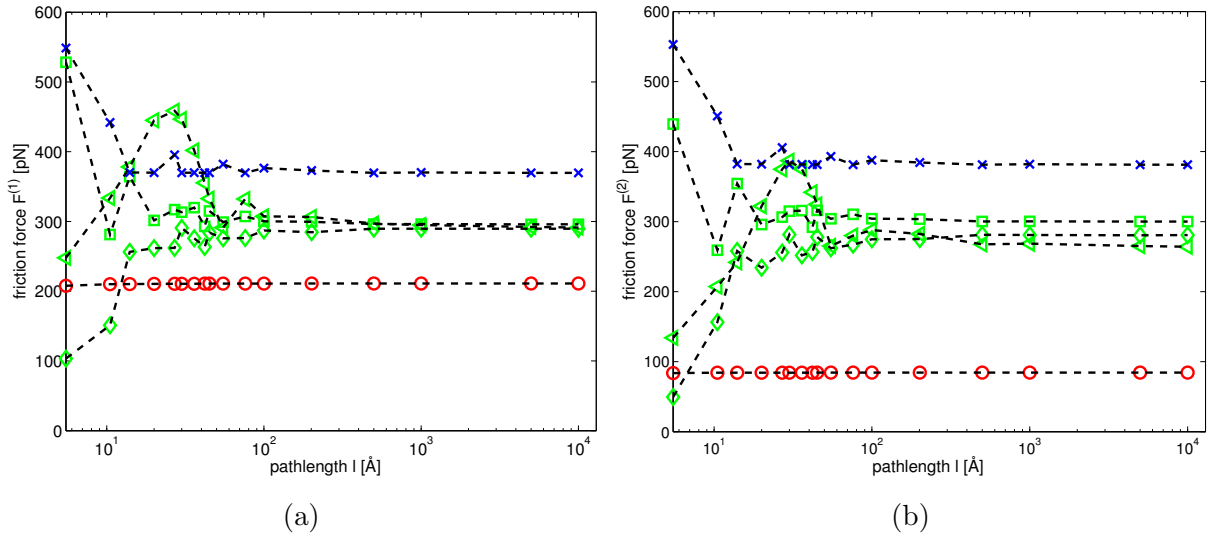
Figure 3.27: Plot of the mean friction force $F^{(1)}$ (a) and $F^{(2)}$ (b) versus the path length l for a load $L = 290\,\mathrm{pN}$. Both periodic paths $0°$ (red circles) and $30°$ (blue crosses) are shown alongside three quasi aperiodic ones (green diamonds for $-10°$, green triangles for $3°$ and green squares for $10°$). Dashed lines are plotted to guide the eye.

direction where the value is negative. This can also be seen by the large spread in the $F_0^{(2)}$ data for aperiodic paths. Linear fitting leads to higher values for μ, as is to be expected by the method (see section 3.5.3). Experimental data for zirconium on zirconium sliding in vacuum have been found for a macroscopic pin on disc experiment [187], however, wear was recorded during the sliding and so the reported values of $\mu_{\mathrm{exp}} = 0.6 - 0.8$ are not ideally comparable to our results where wear is prohibited by the method. The coefficients computed with our approach, 0.26 to 0.80, depending on direction and method, compare well to the values $(0.4 - 0.6)$ reported by Buckley for basal plane sliding of single crystal titanium [183], as is to be expected for such similar materials. Nevertheless, our results for zirconium are systematically lower than for titanium which is surprising considering that titanium is harder. For reasons stated in section 3.6.5, however, the data on titanium have to be considered with care.

3.8 Using the true contact area

In section 3.4 we described the method we use to keep the load constant during our sliding calculations. The load is computed there as $L = p\,A_{\mathrm{C}}$, with the pressure p and the cross section of the unit cell A_{C}. The cross section, however, is only an approximation of the true contact area between the two slabs, even if they are atomically flat. The true contact
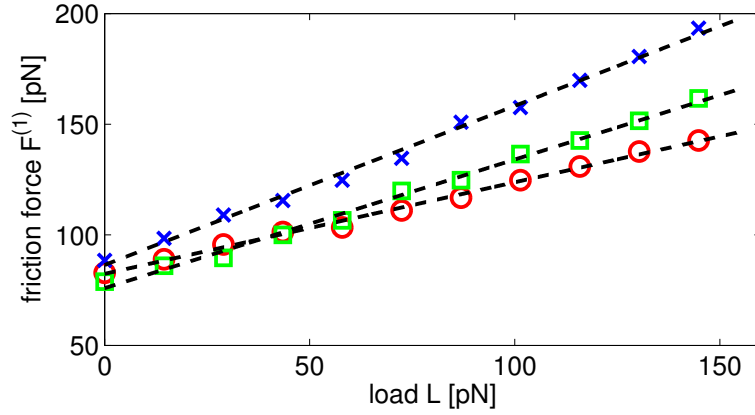
(a)
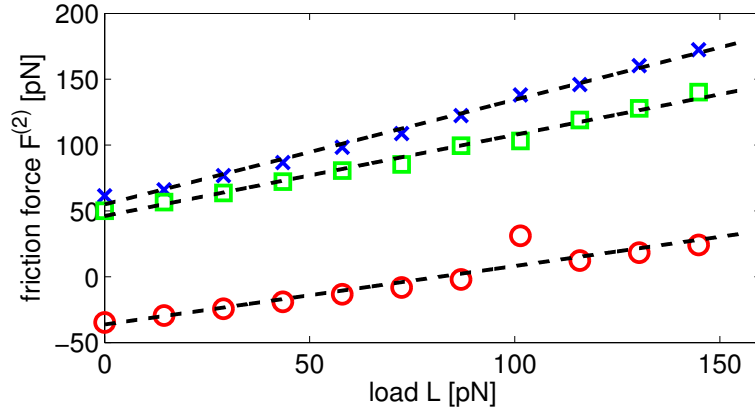
(b)

Figure 3.28: Plot of the friction force $F^{(1)}$ (a) and $F^{(2)}$ (b) versus load L for the slip plane of hcp Zr(0001). Both periodic paths 0° (red circles) and 30° (blue crosses) are shown alongside the quasi aperiodic 10° path (green squares) which serves as a prototype for all other quasi aperiodic paths. The dashed black lines are linear fits.

	$F_0^{(1)}$[pN]	$F_0^{(2)}$[pN]	$\mu^{(1)}$	$\mu^{(2)}$	$\mu_{\text{lin}}^{(1)}$	$\mu_{\text{lin}}^{(2)}$	μ_{exp}
0°	88	-28	0.26	0.24	0.41	0.44	-
30°	95	71	0.45	0.39	0.72	0.80	-
aperiodic	82 ± 3.2	61 ± 20.7	0.37 ± 0.01	0.32 ± 0.07	0.57 ± 0.02	0.64 ± 0.09	$0.6 - 0.8$

Table 3.3: Derjaguin-offset values F_0 and coefficients of friction μ corresponding to the friction forces $F^{(1)}$ and $F^{(2)}$, see equations (3.1) - (3.3). The constitutive system parameters for the aperiodic directions are given by the average over all examined quasi aperiodic paths. Experimental data are from a pin on disc experiment in vacuum under wear inducing load taken from Ref. 187.

area should depend on the lateral position of the slabs with respect to each other and, more importantly, on the applied pressure.

In chapter 2 we developed a formalism that defines the true contact area on the basis of Bader partitioning. Applying this approach to the sliding systems discussed in chapter 3 is quite straightforward. The most critical step, selecting a density cutoff ρ_{cut}, can be omitted as all systems are either at, or compressed beyond, their equilibrium distance and thus definitely in contact at all selected pressure values. Therefore, the contact area was calculated with the density cutoff parameter set to zero in the code by Henkelman, Sanville, and Tang [120–122].

Calculating the contact area depending on the lateral position of the slabs and on the external pressure allows us to define a mean contact area A for each pressure value and sliding direction. To this end we interpolate between the grid points and construct smooth area-surfaces for each pressure, much as we do for the forces and energies (see section 3.2). The contact area for each sliding direction can then be calculated as an average over the whole path length for each specific external pressure.

3.8.1 True contact area versus pressure

In figure 3.29 the true contact area A is plotted with respect to the external pressure p for the copper, titanium, and zirconium sliding systems. In all three cases the behavior is linear, which is in accordance with the law of Greenwood and Williamson for nominally flat surfaces [105]. Of course Greenwood and Williamson assume ideally elastic surfaces with spherical asperity of equal radius and normal distributed height, but the linear law apparently is still valid on the nano scale when the only roughness is formed by atomic undulations.

Due to atomic roughness, even at zero pressure, all contact areas are larger than the cross sections of the corresponding unit cells which are $A_C(\text{Cu}) = 5.72\,\text{Å}^2$, $A_C(\text{Ti}) = 7.45\,\text{Å}^2$, and $A_C(\text{Zr}) = 9.04\,\text{Å}^2$. Comparing the (111) surface of fcc copper (figure 3.29a) with the (0001) surfaces of hcp titanium (figure 3.29b) and zirconium (figure 3.29c) it is of great importance to notice the different scales on the y axes. Both hcp systems show a considerably larger contact area for zero pressure ($\sim 70\%$ for titanium and $\sim 50\%$ for zirconium) compared to the fcc copper system and they vary strongly with load. While the area of the copper system is nearly constant and has increased by only by 2% at the maximum pressure of $6.5\,\text{GPa}$ compared to zero pressure, the hcp systems show an increase of about 9% for titanium and 12% for zirconium. Also, the difference between sliding directions is negligible for copper while it is about $1\,\text{Å}^2$ between $0°$ and $30°$ for the hcp metals. An explanation for this effect could be that the c/a ratio of titanium

and zirconium is smaller by 2% (Zr) and 3% (Ti) than the ideal ratio for close packing of $2\sqrt{6}/3$, making the (0001) hcp surface more open than the (111) fcc surface.

3.8.2 The impact of the true contact area on the results

As the load is computed as $L = p\,A_{\mathrm{C}}$ in our model, an increased contact area A compared to the cross section of the unit cell A_C leads to an increased load for a fixed pressure. As the calculated friction force for each pressure remains the same, an increase in load leads to flatter friction versus load curves and ultimately lower coefficients of friction (see table 3.4). For titanium and zirconium, contact areas for the $0°$ direction are substantially smaller than for the aperiodic directions with the $30°$ path leading to the largest areas. This means that the load is increased the most for the high friction paths and the least for the low friction direction. Thus the friction curves are stretched out to higher loads while the different sliding directions are pushed closer together (see figure 3.30). For copper, the second effect is marginal, as the true contact area is nearly constant over the entire range of pressures (see figure 3.29a)

The friction coefficients presented in table 3.4 are systematically lower than the numbers calculated without the Bader partitioning scheme in tables 3.1, 3.2, and 3.3. As mentioned before, this is an effect of the increased true contact area compared to the cross section of the unit cell which results in reduced load at each given pressure. For copper the coefficients of friction calculated without the true contact area range from $\mu^{(2)}(0°) = 0.60$ to $\mu_{\mathrm{lin}}^{(2)}(0°) = 1.46$. These values are reduced by $\sim 25\%$ when using the real contact area (see table 3.4). In the case of titanium, the spread in the calculated friction coefficients is much larger, ranging from $\mu^{(1)}(0°) = 0.17$ to $\mu_{\mathrm{lin}}^{(2)}(0°) = 1.87$ without using Bader partitioning and, as can be seen in table 3.4, the values are reduced by $\sim 60\%$ if the true contact area is used. In the case of zirconium the usage of Bader partitioning is reducing the lowest friction coefficient, $\mu^{(2)}(0°) = 0.24$, by 30%, and the highest value, $\mu_{\mathrm{lin}}^{(2)}(0°) = 0.80$, by 35%, slightly decreasing the relative spread of the values.

Comparing the friction coefficients for aperiodic sliding directions of the three examined materials in table 3.4 with the experimental values leads to excellent agreement for copper, fair agreement for titanium and an underestimation for zirconium. However, the data for zirconium is from a macro scale experiment, as mentioned in section 3.7.4, which makes it difficult to compare to our values.
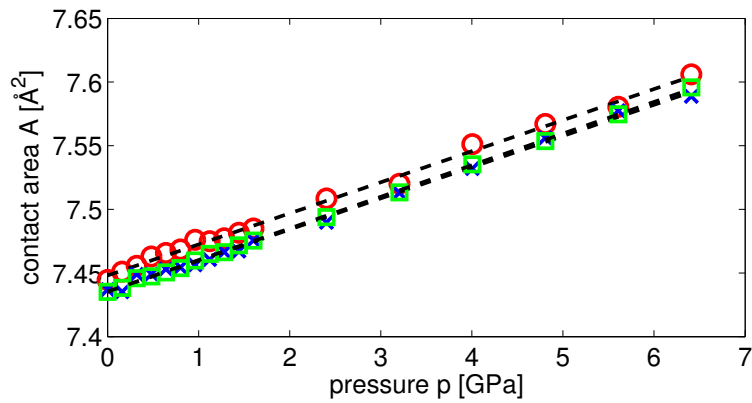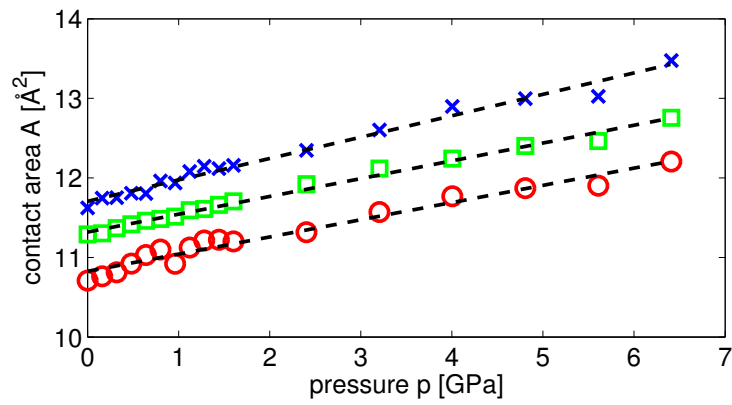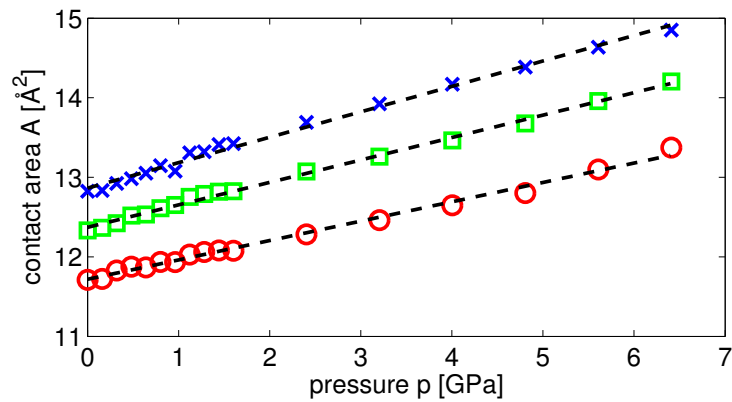
Figure 3.29: contact area A versus pressure p for (a) Cu(111), (b) Ti(0001), and (c) Zr(0001). Depicted are 0° (red circles), 10° (green squares), and 30° (blue crosses) paths. Notice the different y axes.

(a) Using the cross section A_C

(b) Using Bader partitioning
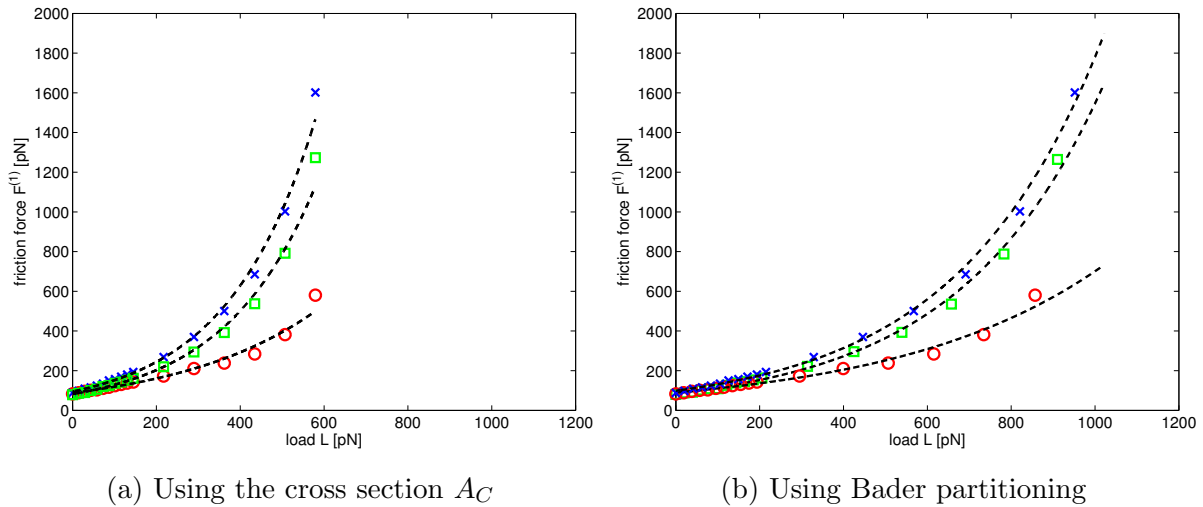
Figure 3.30: Friction force $F^{(1)}$ versus load L for the basal slip plane of hcp Zr. Both periodic paths 0° (red circles) and 30° (blue crosses) are shown alongside the quasi aperiodic 10° path (green squares) which serves as a prototype for all other quasi aperiodic paths. In panel (a) the cross section of the unit cell is used to calculate the load, in panel (b) the Bader partitioning scheme detailed in chapter 2 is used.

	$F_0^{(1)}$[pN]	$F_0^{(2)}$[pN]	$\mu^{(1)}$	$\mu^{(2)}$	$\mu_{\text{lin}}^{(1)}$	$\mu_{\text{lin}}^{(2)}$	μ_{exp}
				copper			
0°	128	101	0.56	0.46	0.81	0.67	-
30°	160	110	0.78	0.69	1.11	1.12	-
aperiodic	158 ± 4.4	122 ± 2.7	0.71 ± 0.05	0.66 ± 0.04	1.02 ± 0.11	0.96 ± 0.03	$0.78 - 0.92$ [a]
				titanium			
0°	84	105	0.10	0.20	0.29	0.70	-
30°	100	200	0.25	0.34	0.52	1.14	-
aperiodic	64 ± 4.6	137 ± 38	0.16 ± 0.01	0.29 ± 0.05	0.31 ± 0.01	0.90 ± 0.18	$0.3 - 0.68$ [b]
				zirconium			
0°	90	-26	0.19	0.17	0.31	0.33	-
30°	99	75	0.29	0.25	0.48	0.53	-
aperiodic	85 ± 3.2	64 ± 21.3	0.25 ± 0.01	0.21 ± 0.05	0.40 ± 0.02	0.45 ± 0.06	$0.6 - 0.8$ [c]

Table 3.4: Derjaguin-offset values F_0 and coefficients of friction μ corresponding to the friction forces $F^{(1)}$ and $F^{(2)}$, see equations (3.1) - (3.3). The constitutive system parameters for the aperiodic directions are given by the average over all examined quasi aperiodic paths. Ranges of experimental values are taken from references 180 [a], 182–184 [b], and 187 [c]

3.9   Summary and conclusion

In this chapter we presented a novel approach to construct nanofriction vs. load curves from total energy landscapes generated by DFT calculations. The method is parameter-free as no external input is needed to compute the friction force since internal relaxations of the system are assumed to dissipate the energy. A quasi static grid approach allows us to study very long sliding paths during constant load conditions. We find that the friction forces on the nanoscale converge for all aperiodic paths to a value between the limits set by two paths along high symmetry directions. The method was tested on three different close packed systems, (111) fcc copper, (0001) hcp titanium, and (0001) hcp zirconium rubbing against an equal counterpart.

We define two distinct ways to calculate the mean friction force which both lead to comparable results and yield an exponential friction law which in the low load regime can be expanded to a linear relation of Derjaguin form. To avoid moving on conservative energy landscapes is an important part of our approach. To this end we assume static sliding without relaxations until we reach a maximum in energy, at which point the system is relaxed and slides to the next minimum (see section 3.2.3 and especially figure 3.7). This cycle is repeated until the desired path length is reached. While the choice of using also unrelaxed contributions in our approach may seem unorthodox, the results are in excellent agreement with more realistic but computationally more demanding shearing calculations. These where carried out only for the limiting cases of low and high friction in the fcc Cu(111) on fcc Cu(111) system, but support our quasi-static method, especially when compared to the established model by Zhong and Tománek [18, 19].

The two methods we proposed to calculate the friction force serve primarily as an internal test of consistency of our model, however, since total energies can be calculated with a higher accuracy than forces, we would give preference to $F^{(2)}$ (as given by equation 3.2). The exponential increase of friction with applied load is comparable to the experimental findings of Gosvami et al. [163] where a strong increase of friction at high loads was found for Au(111) and Cu(100). A similar behavior is found in Fig. 12 of Ref. 20 by performing classical MD simulations. However, both groups attribute this strong increase in friction to the onset of wear at high loads, which is not considered in our work. We show that we can obtain a good linear dependency of the friction force on the load in the low load regime (which is still under a high internal load due to adhesion) reminiscent of the Amontons–Coulomb law and also often found on the nanoscale [160–162]. The calculated coefficients of friction fit well to the measured values in macroscopic experiments, but there remains the possibility of a coincidental agreement which would require further studies, both theoretically and experimentally, to be ruled out.

Results for the titanium sliding system detailed in section 3.6 are affected by structural instabilities as discussed in subsection 3.6.5. The efforts employed to correct or at least reduce the errors unfortunately are still unsuccessful up to date and so the findings had to be presented in the current form. We believe that the errors in the static energy curves to some extend effect the method $F^{(2)}$ less than $F^{(1)}$, since the forces which are relevant in the latter approach are small in the problematic regions. Thus we recommend to use the friction data obtained by method $F^{(1)}$ for comparisons with other work and experimental data in the case of titanium, regardless of our general preference of $F^{(2)}$.

Incorporating our approach to determine the true area of contact, as introduced in chapter 2, into the evaluation of the loading force leads to higher loads for each selected pressure. This influences the friction versus load curves by stretching them laterally and thus reducing the coefficients of friction by about 25%–35%.

Our results are in fair agreement with experimental data in the cases where these are available from a similar setting (ultra high vacuum, clean and preferably single crystal surfaces of the same orientation, wearless sliding conditions,...). However, the main message we want to convey is the importance of sliding direction and the fact that relaxed data alone are unable to capture the correct energetics of a sliding system, if the calculations are not taking the full history of the sliding system into account (i.e. shearing).

A paper including the most important results of this chapter is currently under consideration at Physical Review B with a preprint published on the arXiv.org server [188].

Bibliography

[1] H. P. Jost and G. B. M. of Technology, *Committee on Tribology Report*. H.M. Stationery Office, 1966.

[2] B. Bhushan, *Introduction to Tribology*. John Wiley & Sons, Ltd, second ed., 2013.

[3] P. Newberry, *El Bersheh: The Tomb of Tehuti-Hetep*, vol. 1. London: Egypt Exploration Fund, 1895.

[4] A. Fall, B. Weber, M. Pakpour, N. Lenoir, N. Shahidzadeh, J. Fiscina, C. Wagner, and D. Bonn, "Sliding friction on wet and dry sand," *Phys. Rev. Lett.*, vol. 112, p. 175502, Apr 2014.

[5] G. Amontons, "De la resistance causee dans les machines," *Mem. Acad. R. A*, pp. 275–282, 1699.

[6] C.-A. Coulomb *Mem Acad. Sci. Savants Etrangers*, vol. 7, pp. 343–382, 1773.

[7] B. Derjaguin, "Molekulartheorie der äußeren Reibung," *Zeitschrift für Physik*, vol. 88, no. 9-10, pp. 661–675, 1934.

[8] F. P. Bowden and D. Tabor, "The Area of Contact between Stationary and between Moving Surfaces," *Royal Society of London Proceedings Series A*, vol. 169, pp. 391–413, Feb. 1939.

[9] F. P. Bowden and D. Tabor, *The Friction and Lubrication of Solids*. Oxford University Press, 1950.

[10] D. Tabor and R. H. S. Winterton, "The direct measurement of normal and retarded van der waals forces," *Proceedings of the Royal Society of London. A. Mathematical and Physical Sciences*, vol. 312, no. 1511, pp. 435–450, 1969.

[11] J. N. Israelachvili and G. E. Adams, "Measurement of forces between two mica surfaces in aqueous electrolyte solutions in the range 0-100 nm," *J. Chem. Soc., Faraday Trans. 1*, vol. 74, pp. 975–1001, 1978.

[12] G. Binnig, H. Rohrer, C. Gerber, and E. Weibel, "Surface studies by scanning tunneling microscopy," *Phys. Rev. Lett.*, vol. 49, pp. 57–61, Jul 1982.

[13] G. Binnig, C. F. Quate, and C. Gerber, "Atomic force microscope," *Phys. Rev. Lett.*, vol. 56, pp. 930–933, Mar 1986.

[14] R. Bennewitz, "Friction force microscopy," *Materials Today*, vol. 8, no. 5, pp. 42 – 48, 2005.

[15] A. Vanossi, N. Manini, M. Urbakh, S. Zapperi, and E. Tosatti, "*Colloquium*: Modeling friction: From nanoscale to mesoscale," *Rev. Mod. Phys.*, vol. 85, pp. 529–552, Apr 2013.

[16] L. Prandtl, "Ein Gedankenmodell zur kinetischen Theorie der festen Körper," *Zeitschrift für Angewandte Mathematik und Mechanik*, vol. 8, no. 2, pp. 85–106, 1928.

[17] G. Tomlinson, "CVI. a molecular theory of friction," *Philosophical Magazine Series 7*, vol. 7, no. 46, pp. 905–939, 1929.

[18] W. Zhong and D. Tománek, "First-principles theory of atomic-scale friction," *Phys. Rev. Lett.*, vol. 64, pp. 3054–3057, Jun 1990.

[19] D. Tománek, W. Zhong, and H. Thomas, "Calculation of an atomically modulated friction force in atomic-force microscopy," *Europhys. Lett.*, vol. 15, no. 8, pp. 887–892, 1991.

[20] Y. Dong, Q. Li, and A. Martini, "Molecular dynamics simulation of atomic friction: A review and guide," *Journal of Vacuum Science and Technology A: Vacuum, Surfaces, and Films*, vol. 31, no. 3, p. 030801, 2013.

[21] M. Garvey, O. J. Furlong, M. Weinert, and W. T. Tysoe, "Shear properties of potassium chloride films on iron obtained using density functional theory," *Journal of Physics: Condensed Matter*, vol. 23, no. 26, p. 265003, 2011.

[22] M. Garvey, M. Weinert, and W. Tysoe, "On the pressure dependence of shear strengths in sliding, boundary-layer friction," *Tribology Letters*, vol. 44, no. 1, pp. 67–73, 2011.

[23] M. Garvey, M. Weinert, and W. T. Tysoe, "On the film thickness dependence of shear strengths in sliding, boundary-layer friction," *Wear*, vol. 274 - 275, no. 0, pp. 281 – 285, 2012.

[24] G. Zilibotti and M. C. Righi, "Ab initio calculation of the adhesion and ideal shear strength of planar diamond interfaces with different atomic structure and hydrogen coverage," *Langmuir*, vol. 27, no. 11, pp. 6862–6867, 2011.

[25] S. Cahangirov, C. Ataca, M. Topsakal, H. Sahin, and S. Ciraci, "Frictional figures of merit for single layered nanostructures," *Phys. Rev. Lett.*, vol. 108, p. 126103, Mar 2012.

[26] L.-F. Wang, T.-B. Ma, Y.-Z. Hu, and H. Wang, "Atomic-scale friction in graphene oxide: An interfacial interaction perspective from first-principles calculations," *Phys. Rev. B*, vol. 86, p. 125436, Sep 2012.

[27] J. Wang, F. Wang, J. Li, S. Wang, Y. Song, Q. Sun, and Y. Jia, "Theoretical study of superlow friction between two single-side hydrogenated graphene sheets," *Tribology Letters*, vol. 48, no. 2, pp. 255–261, 2012.

[28] S. Kwon, J.-H. Ko, K.-J. Jeon, Y.-H. Kim, and J. Y. Park, "Enhanced nanoscale friction on fluorinated graphene," *Nano Letters*, vol. 12, no. 12, pp. 6043–6048, 2012.

[29] C. M. Mate, G. M. McClelland, R. Erlandsson, and S. Chiang, "Atomic-scale friction of a tungsten tip on a graphite surface," *Phys. Rev. Lett.*, vol. 59, pp. 1942–1945, Oct 1987.

[30] C. Donnet, "Recent progress on the tribology of doped diamond-like and carbon alloy coatings: a review," *Surface and Coatings Technology*, vol. 100101, no. 0, pp. 180 – 186, 1998.

[31] R. Neitola and T. A. Pakkanen, "Ab initio studies on the atomic-scale origin of friction between diamond (111) surfaces," *The Journal of Physical Chemistry B*, vol. 105, no. 7, pp. 1338–1343, 2001.

[32] S. Dag and S. Ciraci, "Atomic scale study of superlow friction between hydrogenated diamond surfaces," *Phys. Rev. B*, vol. 70, p. 241401, Dec 2004.

[33] R. Neitola and T. A. Pakkanen, "Ab initio studies on the atomic-scale origin of friction between hydrocarbon layers," *Chemical Physics*, vol. 299, no. 1, pp. 47 – 56, 2004.

[34] R. Neitola, H. Ruuska, and T. A. Pakkanen, "Ab initio studies on nanoscale friction between graphite layers: effect of model size and level of theory," *The Journal of Physical Chemistry B*, vol. 109, no. 20, pp. 10348–10354, 2005. PMID: 16852254.

[35] R. Neitola and T. A. Pakkanen, "Ab initio studies on nanoscale friction between fluorinated diamond surfaces: effect of model size and level of theory," *The Journal of Physical Chemistry B*, vol. 110, no. 33, pp. 16660–16665, 2006. PMID: 16913803.

[36] C. Møller and M. S. Plesset, "Note on an approximation treatment for many-electron systems," *Phys. Rev.*, vol. 46, pp. 618–622, Oct 1934.

[37] S. Redner, "Citation statistics from 110 years of physical review," *Physics Today*, vol. 58, pp. 49–54, 2005.

[38] A. P. Society, "Physical review online archive," Jan 2014.

[39] W. Kohn and L. J. Sham, "Self-consistent equations including exchange and correlation effects," *Phys. Rev.*, vol. 140, no. 4A, p. 1133, 1965.

[40] P. Hohenberg and W. Kohn, "Inhomogeneous electron gas," *Phys. Rev.*, vol. 136, no. 3B, p. 864, 1964.

[41] J. P. Perdew and A. Zunger, "Self-interaction correction to density-functional approximations for many-electron systems," *Phys. Rev. B*, vol. 23, pp. 5048–5079, May 1981.

[42] D. M. Ceperley and B. J. Alder, "Ground state of the electron gas by a stochastic method," *Phys. Rev. Lett.*, vol. 45, pp. 566–569, Aug 1980.

[43] T. Reuters, "Web of knowledge," Jan 2014.

[44] J. P. Perdew, K. Burke, and M. Ernzerhof, "Generalized gradient approximation made simple," *Phys. Rev. Lett.*, vol. 77, p. 3865, 1996.

[45] G. Kresse and J. Furthmüller, "Efficiency of ab-initio total energy calculations for metals and semiconductors using a plane-wave basis set," *Comput. Mat. Sci.*, vol. 6, p. 15, 1996.

[46] W. J. Hehre, R. Ditchfield, and J. A. Pople, "Selfconsistent molecular orbital methods. XII. further extensions of gaussiantype basis sets for use in molecular orbital studies of organic molecules," *The Journal of Chemical Physics*, vol. 56, no. 5, pp. 2257–2261, 1972.

[47] P. Blaha, K. Schwarz, P. Sorantin, and S. Trickey, "Full-potential, linearized augmented plane wave programs for crystalline systems," *Computer Physics Communications*, vol. 59, no. 2, pp. 399 – 415, 1990.

[48] X. Gonze, J. Beuken, R. Caracas, F. Detraux, M. Fuchs, G. Rignanese, L. Sindic, M. Verstraete, G. Zerah, F. Jollet, M. Torrent, A. Roy, M. Mikami, P. Ghosez, J. Raty, and D. Allan, "First-principles computation of material properties: the ABINIT software project," *COMPUTATIONAL MATERIALS SCIENCE*, vol. 25, pp. 478–492, NOV 2002.

[49] K. Held, "Lecture notes on computational materials science," 2008.

[50] M. Levy, "Universal variational functionals of electron densities, first-order density matrices, and natural spin-orbitals and solution of the v-representability problem," *Proceedings of the National Academy of Sciences*, vol. 76, no. 12, pp. 6062–6065, 1979.

[51] M. Marder, *Condensed Matter Physics*. Wiley-Interscience, 2000.

[52] O. Gunnarsson, M. Jonson, and B. I. Lundqvist, "Descriptions of exchange and correlation effects in inhomogeneous electron systems," *Phys. Rev. B*, vol. 20, pp. 3136–3164, Oct 1979.

[53] R. Dreizler and E. Gross, *Density Functional Theory*. New York: Plenum Press, 1995.

[54] J. Perdew, J. Chevary, S. Vosko, K. Jackson, M. Pederson, D. Singh, and C. Fiolhais, "Atoms, molecules, solids, and surfaces: Applications of the generalized gradient approximation for exchange and correlation," *Phys. Rev. B*, vol. 46, p. 6671, 1992.

[55] V. Ozoliņš and M. Körling, "Full-potential calculations using the generalized gradient approximation: Structural properties of transition metals," *Phys. Rev. B*, vol. 48, pp. 18304–18307, Dec 1993.

[56] C. Filippi, D. J. Singh, and C. J. Umrigar, "All-electron local-density and generalized-gradient calculations of the structural properties of semiconductors," *Phys. Rev. B*, vol. 50, pp. 14947–14951, Nov 1994.

[57] J. Perdew, J. Chevary, S. Vosko, K. Jackson, M. Pederson, D. Singh, and C. Fiolhais, "Erratum: Atoms, molecules, solids, and surfaces: Applications of the generalized gradient approximation for exchange and correlation," *Phys. Rev. B*, vol. 48, p. 4978, 1993.

[58] J. P. Perdew, K. Burke, and M. Ernzerhof, "Erratum: Generalized gradient approximation made simple," *Phys. Rev. Lett.*, vol. 78, p. 1396, 1997.

[59] J. D. Van der Waals, *Over de Continuiteit van den Gas en Vloeistoftoestand.* PhD thesis, Leiden University, 1873.

[60] E. H. Lieb and W. E. Thirring, "Universal nature of van der Waals forces for Coulomb systems," *Phys. Rev. A*, vol. 34, pp. 40–46, Jul 1986.

[61] R. H. S. Winterton, "Van der Waals forces," *Contemp. Phys.*, vol. 11, no. 6, pp. 559–574, 1970.

[62] H. Butt and M. Kappl, *Surface and Interfacial Forces.* Physics textbook, Wiley, 2009.

[63] H. Hellmann, *Compendium of Chemical Terminology.* International Union of Pure and Applied Chemistry, 2 ed., 1997.

[64] J. Klimeš and A. Michaelides, "Perspective: Advances and challenges in treating van der waals dispersion forces in density functional theory," *J. Chem. Phys.*, vol. 137, no. 12, p. 120901, 2012.

[65] V. R. Cooper, L. Kong, and D. C. Langreth, "Computing dispersion interactions in density functional theory," *Physics Procedia*, vol. 3, no. 3, pp. 1417 – 1430, 2010. Proceedings of the 22th Workshop on Computer Simulation Studies in Condensed Matter Physics (CSP 2009).

[66] J. Klimeš, D. R. Bowler, and A. Michaelides, "Chemical accuracy for the van der Waals density functional," *Journal of Physics: Condensed Matter*, vol. 22, no. 2, p. 022201, 2010.

[67] O. A. Vydrov and T. Van Voorhis, "Nonlocal van der Waals density functional: The simpler the better," *J. Chem. Phys.*, vol. 133, no. 24, p. 244103, 2010.

[68] T. Sato and H. Nakai, "Density functional method including weak interactions: Dispersion coefficients based on the local response approximation," *J. Chem. Phys.*, vol. 131, no. 22, p. 224104, 2009.

[69] T. Sato and H. Nakai, "Local response dispersion method. II. Generalized multi-center interactions," *J. Chem. Phys.*, vol. 133, no. 19, p. 194101, 2010.

[70] M. Dion, H. Rydberg, E. Schröder, D. C. Langreth, and B. I. Lundqvist, "Van der Waals density functional for general geometries," *Phys. Rev. Lett.*, vol. 92, p. 246401, Jun 2004.

[71] F. Furche, "Molecular tests of the random phase approximation to the exchange-correlation energy functional," *Phys. Rev. B*, vol. 64, p. 195120, Oct 2001.

[72] J. G. Ángyán, R.-F. Liu, J. Toulouse, and G. Jansen, "Correlation energy expressions from the adiabatic-connection fluctuationdissipation theorem approach," *J. Chem. Theory Comput.*, vol. 7, no. 10, pp. 3116–3130, 2011.

[73] A. Heßelmann, "Random-phase-approximation correlation method including exchange interactions," *Phys. Rev. A*, vol. 85, p. 012517, Jan 2012.

[74] J. Harl and G. Kresse, "Accurate bulk properties from approximate many-body techniques," *Phys. Rev. Lett.*, vol. 103, p. 056401, Jul 2009.

[75] J. F. Dobson and B. P. Dinte, "Constraint satisfaction in local and gradient susceptibility approximations: Application to a van der Waals density functional," *Phys. Rev. Lett.*, vol. 76, pp. 1780–1783, Mar 1996.

[76] F. Furche and T. Van Voorhis, "Fluctuation-dissipation theorem density-functional theory," *J. Chem. Phys.*, vol. 122, no. 16, p. 164106, 2005.

[77] J. Klimeš, D. R. Bowler, and A. Michaelides, "Van der Waals density functionals applied to solids," *Phys. Rev. B*, vol. 83, p. 195131, May 2011.

[78] A. D. Becke, "On the largegradient behavior of the density functional exchange energy," *J. Chem. Phys.*, vol. 85, no. 12, pp. 7184–7187, 1986.

[79] F. Mittendorfer, A. Garhofer, J. Redinger, J. Klimeš, J. Harl, and G. Kresse, "Graphene on Ni(111): Strong interaction and weak adsorption," *Phys. Rev. B*, vol. 84, p. 201401, Nov 2011.

[80] M. Vanin, J. J. Mortensen, A. K. Kelkkanen, J. M. Garcia-Lastra, K. S. Thygesen, and K. W. Jacobsen, "Graphene on metals: A van der Waals density functional study," *Phys. Rev. B*, vol. 81, p. 081408, Feb 2010.

[81] D.-L. Chen, W. A. Al-Saidi, and J. K. Johnson, "Noble gases on metal surfaces: Insights on adsorption site preference," *Phys. Rev. B*, vol. 84, p. 241405, Dec 2011.

[82] G. Kresse and J. Hafner, "Ab initio molecular dynamics for liquid metals," *Phys. Rev. B*, vol. 47, p. 558, 1993.

[83] G. Kresse and J. Hafner, "Ab initio molecular-dynamics simulation of the liquid-metal-amorphous-semiconductor transition in germanium," *Phys. Rev. B*, vol. 49, p. 14251, 1994.

[84] G. Kresse and J. Furthmüller, "Efficient iterative schemes for ab initio total-energy calculations using a plane-wave basis set," *Phys. Rev. B*, vol. 54, p. 11169, 1996.

[85] D. Vanderbilt, "Soft self-consistent pseudopotentials in a generalized eigenvalue formalism," *Phys. Rev. B*, vol. 41, p. 7892, 1990.

[86] G. Kresse and J. Hafner, "Norm-conserving and ultrasoft pseudopotentials for first-row and transition-elements," *J. Phys.: Condens. Matter*, vol. 6, p. 8245, 1994.

[87] P. E. Blöchl, "Projector augmented-wave method," *Phys. Rev. B*, vol. 50, p. 17953, 1994.

[88] G. Kresse and D. Joubert, "From ultrasoft pseudopotentials to the projector augmented-wave method," *Phys. Rev. B*, vol. 59, p. 1758, 1999.

[89] J. Paier, R. Hirschl, M. Marsman, and G. Kresse, "The perdew-burke-ernzerhof exchange-correlation functional applied to the G2-1 test set using a plane-wave basis set," *The Journal of Chemical Physics*, vol. 122, no. 23, pp. –, 2005.

[90] J. Heyd, G. E. Scuseria, and M. Ernzerhof, "Hybrid functionals based on a screened coulomb potential," *J. Chem. Phys.*, vol. 118, no. 18, p. 8207, 2003.

[91] J. Paier, M. Marsman, K. Hummer, G. Kresse, I. C. Gerber, and J. G. Ángyán, "Screened hybrid density functionals applied to solids," *J. Chem. Phys.*, vol. 124, p. 154709, 2006.

[92] M. Shishkin and G. Kresse, "Implementation and performance of the frequency-dependent *GW* method within the paw framework," *Phys. Rev. B*, vol. 74, p. 035101, Jul 2006.

[93] M. Shishkin and G. Kresse, "Self-consistent *GW* calculations for semiconductors and insulators," *Phys. Rev. B*, vol. 75, p. 235102, Jun 2007.

[94] M. Shishkin, M. Marsman, and G. Kresse, "Accurate quasiparticle spectra from self-consistent *GW* calculations with vertex corrections," *Phys. Rev. Lett.*, vol. 99, p. 246403, Dec 2007.

[95] F. Fuchs, J. Furthmüller, F. Bechstedt, M. Shishkin, and G. Kresse, "Quasiparticle band structure based on a generalized kohn-sham scheme," *Phys. Rev. B*, vol. 76, p. 115109, Sep 2007.

[96] J. Harl and G. Kresse, "Cohesive energy curves for noble gas solids calculated by adiabatic connection fluctuation-dissipation theory," *Phys. Rev. B*, vol. 77, p. 045136, Jan 2008.

[97] J. Harl, L. Schimka, and G. Kresse, "Assessing the quality of the random phase approximation for lattice constants and atomization energies of solids," *Phys. Rev. B*, vol. 81, p. 115126, Mar 2010.

[98] H. Hertz, "Über die Berührung fester elastischer Körper," *Journal für die reine und angewandte Mathematik*, vol. 92, pp. 156–171, 1881.

[99] K. L. Johnson, K. Kendall, and A. D. Roberts, "Surface energy and the contact of elastic solids," *Proceedings of the Royal Society of London. A. Mathematical and Physical Sciences*, vol. 324, no. 1558, pp. 301–313, 1971.

[100] B. Derjaguin, V. Muller, and Y. Toporov, "Effect of contact deformations on the adhesion of particles," *Journal of Colloid and Interface Science*, vol. 53, no. 2, pp. 314 – 326, 1975.

[101] D. Tabor, "Surface forces and surface interactions," *Journal of Colloid and Interface Science*, vol. 58, no. 1, pp. 2 – 13, 1977. International Conference on Colloids and Surfaces.

[102] D. Maugis, "Adhesion of spheres: The JKR-DMT transition using a dugdale model," *Journal of Colloid and Interface Science*, vol. 150, no. 1, pp. 243 – 269, 1992.

[103] R. W. Carpick, D. Ogletree, and M. Salmeron, "A general equation for fitting contact area and friction vs load measurements," *Journal of Colloid and Interface Science*, vol. 211, no. 2, pp. 395 – 400, 1999.

[104] J. F. Archard, "Elastic deformation and the laws of friction," *Proceedings of the Royal Society of London. Series A. Mathematical and Physical Sciences*, vol. 243, no. 1233, pp. 190–205, 1957.

[105] J. A. Greenwood and J. B. P. Williamson, "Contact of nominally flat surfaces," *Royal Society of London Proceedings Series A*, vol. 295, pp. 300–319, dec 1966.

[106] A. Bush, R. Gibson, and T. Thomas, "The elastic contact of a rough surface," *Wear*, vol. 35, no. 1, pp. 87 – 111, 1975.

[107] B. N. J. Persson, "Elastoplastic contact between randomly rough surfaces," *Phys. Rev. Lett.*, vol. 87, p. 116101, Aug 2001.

[108] B. N. J. Persson, F. Bucher, and B. Chiaia, "Elastic contact between randomly rough surfaces: Comparison of theory with numerical results," *Phys. Rev. B*, vol. 65, p. 184106, Apr 2002.

[109] B. Luan and M. O. Robbins, "The breakdown of continuum models for mechanical contacts," *Nature*, vol. 435, pp. 929 – 932, Jun 2005.

[110] Y. Mo, K. T. Turner, and I. Szlufarska, "Friction laws at the nanoscale," *Nature*, vol. 457, pp. 1116 – 1119, Feb 2009.

[111] S. Cheng and M. Robbins, "Defining contact at the atomic scale," *Tribology Letters*, vol. 39, no. 3, pp. 329–348, 2010.

[112] S. Eder, A. Vernes, G. Vorlaufer, and G. Betz, "Molecular dynamics simulations of mixed lubrication with smooth particle post-processing," *Journal of Physics: Condensed Matter*, vol. 23, no. 17, p. 175004, 2011.

[113] N. A. Burnham, R. J. Colton, and H. M. Pollock, "Interpretation issues in force microscopy," *Journal of Vacuum Science & Technology A*, vol. 9, no. 4, pp. 2548–2556, 1991.

[114] D. W. Brenner, O. A. Shenderova, J. A. Harrison, S. J. Stuart, B. Ni, and S. B. Sinnott, "A second-generation reactive empirical bond order (REBO) potential energy expression for hydrocarbons," *Journal of Physics Condensed Matter*, vol. 14, pp. 783–802, Feb. 2002.

[115] R. F. W. Bader, "A quantum theory of molecular structure and its applications," *Chemical Reviews*, vol. 91, no. 5, pp. 893–928, 1991.

[116] R. F. W. Bader, "Molecular fragments or chemical bonds," *Accounts of Chemical Research*, vol. 8, no. 1, pp. 34–40, 1975.

[117] J. Schwinger, "The theory of quantized fields. I," *Phys. Rev.*, vol. 82, pp. 914–927, Jun 1951.

[118] R. F. W. Bader, "Atoms in molecules," *Accounts of Chemical Research*, vol. 18, no. 1, pp. 9–15, 1985.

[119] K. Momma and F. Izumi, "*VESTA3* for three-dimensional visualization of crystal, volumetric and morphology data," *Journal of Applied Crystallography*, vol. 44, pp. 1272–1276, Dec 2011.

[120] G. Henkelman, A. Arnaldsson, and H. Jónsson, "A fast and robust algorithm for bader decomposition of charge density," *Comput. Mater. Sci.*, vol. 36, no. 3, p. 354, 2006.

[121] E. Sanville, S. D. Kenny, R. Smith, and G. Henkelman, "Improved grid-based algorithm for bader charge allocation," *Journal of Computational Chemistry*, vol. 28, no. 5, pp. 899–908, 2007.

[122] W. Tang, E. Sanville, and G. Henkelman, "A grid-based bader analysis algorithm without lattice bias," *Journal of Physics: Condensed Matter*, vol. 21, no. 8, p. 084204, 2009.

[123] R. F. W. Bader, *Atoms in Molecules - A Quantum Theory*. Oxford: University of Oxford Press, 1990.

[124] R. S. Mulliken, "Electronic population analysis on LCAO-MO molecular wave functions. I," *The Journal of Chemical Physics*, vol. 23, no. 10, pp. 1833–1840, 1955.

[125] R. S. Mulliken, "Electronic population analysis on LCAO-MO molecular wave functions. II. overlap populations, bond orders, and covalent bond energies," *The Journal of Chemical Physics*, vol. 23, no. 10, pp. 1841–1846, 1955.

[126] R. S. Mulliken, "Electronic population analysis on LCAO-MO molecular wave functions. III. effects of hybridization on overlap and gross AO populations," *The Journal of Chemical Physics*, vol. 23, no. 12, pp. 2338–2342, 1955.

[127] R. S. Mulliken, "Electronic population analysis on LCAO-MO molecular wave functions. IV. bonding and antibonding in LCAO and valencebond theories," *The Journal of Chemical Physics*, vol. 23, no. 12, pp. 2343–2346, 1955.

[128] F. Hirshfeld, "Bonded-atom fragments for describing molecular charge densities," *Theoretica chimica acta*, vol. 44, no. 2, pp. 129–138, 1977.

[129] P. Bultinck, C. Van Alsenoy, P. W. Ayers, and R. Carb-Dorca, "Critical analysis and extension of the hirshfeld atoms in molecules," *The Journal of Chemical Physics*, vol. 126, no. 14, pp. –, 2007.

[130] F. M. Bickelhaupt, N. J. R. van Eikema Hommes, C. Fonseca Guerra, and E. J. Baerends, "The carbonlithium electron pair bond in $(CH_3Li)_n$ (n = 1, 2, 4)," *Organometallics*, vol. 15, no. 13, pp. 2923–2931, 1996.

[131] C. Fonseca Guerra, J.-W. Handgraaf, E. J. Baerends, and F. M. Bickelhaupt, "Voronoi deformation density (VDD) charges: Assessment of the mulliken, bader, hirshfeld, weinhold, and vdd methods for charge analysis," *Journal of Computational Chemistry*, vol. 25, pp. 189 – 210, 2004.

[132] I. Mayer and P. Salvador, "Overlap populations, bond orders and valences for fuzzy atoms," *Chemical Physics Letters*, vol. 383, no. 34, pp. 368 – 375, 2004.

[133] A. D. Becke, "A multicenter numerical integration scheme for polyatomic molecules," *The Journal of Chemical Physics*, vol. 88, no. 4, pp. 2547–2553, 1988.

[134] R. G. Parr, P. W. Ayers, and R. F. Nalewajski, "What is an atom in a molecule?," *The Journal of Physical Chemistry A*, vol. 109, no. 17, pp. 3957–3959, 2005.

[135] I. Kant, *Kritik der reinen Vernunft*. Johann Friedrich Hartknoch, 1781.

[136] P. M. Morse, "Diatomic molecules according to the wave mechanics. ii. vibrational levels," *Phys. Rev.*, vol. 34, pp. 57–64, Jul 1929.

[137] G. Kresse, M. Marsman, and J. Furthmüller, "Vasp the guide," Jan 2014.

[138] E. N. Voloshina, E. Fertitta, A. Garhofer, F. Mittendorfer, M. Fonin, A. Thissen, and Y. S. Dedkov, "Electronic structure and imaging contrast of graphene moire on metals," *Sci. Rep.*, vol. 3, 2013.

[139] A. Garhofer, *Ab initio studies of graphene-metal interfaces*. PhD thesis, Vienna University of Technology, 2013.

[140] G. Kresse and D. Joubert, "From ultrasoft pseudopotentials to the projector augmented-wave method," *Phys. Rev. B*, vol. 59, pp. 1758–1775, Jan 1999.

[141] M. Methfessel and A. T. Paxton, "High-precision sampling for brillouin-zone integration in metals," *Phys. Rev. B*, vol. 40, pp. 3616–3621, Aug 1989.

[142] J. C. Slater, "Atomic radii in crystals," *Journal of Chemical Physics*, vol. 41, pp. 3199–3204, nov 1964.

[143] E. Clementi, D. L. Raimondi, and W. P. Reinhardt, "Atomic screening constants from SCF functions. II. atoms with 37 to 86 electrons," *The Journal of Chemical Physics*, vol. 47, no. 4, pp. 1300–1307, 1967.

[144] A. Bondi, "Van der Waals volumes and radii," *The Journal of Physical Chemistry*, vol. 68, no. 3, pp. 441–451, 1964.

[145] A. Miedema, "Heat of formation of alloys.," *Philips Technical Review*, vol. 36, no. 8, pp. 217–231, 1976. cited By (since 1996)120.

[146] T. Raghu, R. Sundaresan, P. Ramakrishnan, and T. R. Mohan, "Synthesis of nanocrystalline coppertungsten alloys by mechanical alloying," *Materials Science and Engineering: A*, vol. 304306, no. 0, pp. 438 – 441, 2001.

[147] R. W. G. Wyckoff, *Crystal Structures*. Interscience Publishers New York, second ed., 1963.

[148] P. E. Blöchl, O. Jepsen, and O. K. Andersen, "Improved tetrahedron method for brillouin-zone integrations," *Phys. Rev. B*, vol. 49, pp. 16223–16233, Jun 1994.

[149] L. Vitos, A. Ruban, H. Skriver, and J. Kollr, "The surface energy of metals," *Surface Science*, vol. 411, no. 12, pp. 186 – 202, 1998.

[150] C. Lee, X. Wei, J. W. Kysar, and J. Hone, "Measurement of the elastic properties and intrinsic strength of monolayer graphene," *Science*, vol. 321, no. 5887, pp. 385–388, 2008.

[151] M. Hirano and K. Shinjo, "Atomistic locking and friction," *Phys. Rev. B*, vol. 41, pp. 11837–11851, Jun 1990.

[152] M. Hirano, K. Shinjo, R. Kaneko, and Y. Murata, "Observation of superlubricity by scanning tunneling microscopy," *Phys. Rev. Lett.*, vol. 78, pp. 1448–1451, Feb 1997.

[153] M. Dienwiebel, G. S. Verhoeven, N. Pradeep, J. W. M. Frenken, J. A. Heimberg, and H. W. Zandbergen, "Superlubricity of graphite," *Phys. Rev. Lett.*, vol. 92, p. 126101, Mar 2004.

[154] D. Dietzel, M. Feldmann, U. D. Schwarz, H. Fuchs, and A. Schirmeisen, "Scaling laws of structural lubricity," *Phys. Rev. Lett.*, vol. 111, p. 235502, Dec 2013.

[155] R. Zhang, Z. Ning, Y. Zhang, Q. Zheng, Q. Chen, Q. Xie, Huanhuan Zhang, W. Qian, and F. Wei, "Superlubricity in centimetres-long double-walled carbon nanotubes under ambient conditions," *Nature Nanotechnology*, 2013.

[156] A. E. Filippov, M. Dienwiebel, J. W. M. Frenken, J. Klafter, and M. Urbakh, "Torque and twist against superlubricity," *Phys. Rev. Lett.*, vol. 100, p. 046102, Jan 2008.

[157] X. Feng, S. Kwon, J. Y. Park, and M. Salmeron, "Superlubric sliding of graphene nanoflakes on graphene," *ACS Nano*, vol. 7, no. 2, pp. 1718–1724, 2013.

[158] S. Y. Krylov, K. B. Jinesh, H. Valk, M. Dienwiebel, and J. W. M. Frenken, "Thermally induced suppression of friction at the atomic scale," *Phys. Rev. E*, vol. 71, p. 065101, Jun 2005.

[159] S. Maier, Y. Sang, T. Filleter, M. Grant, R. Bennewitz, E. Gnecco, and E. Meyer, "Fluctuations and jump dynamics in atomic friction experiments," *Phys. Rev. B*, vol. 72, p. 245418, Dec 2005.

[160] G. He, M. H. Müser, and M. O. Robbins, "Adsorbed layers and the origin of static friction," *Science*, vol. 284, no. 5420, pp. 1650–1652, 1999.

[161] M. H. Müser, L. Wenning, and M. O. Robbins, "Simple microscopic theory of amontons's laws for static friction," *Phys. Rev. Lett.*, vol. 86, pp. 1295–1298, Feb 2001.

[162] J. Gao, W. D. Luedtke, D. Gourdon, M. Ruths, J. N. Israelachvili, and U. Landman, "Frictional forces and amontons' law: From the molecular to the macroscopic scale," *J. Phys. Chem. B*, vol. 108, no. 11, pp. 3410–3425, 2004.

[163] N. Gosvami, T. Filleter, P. Egberts, and R. Bennewitz, "Microscopic friction studies on metal surfaces," *Tribology Letters*, vol. 39, no. 1, pp. 19–24, 2010.

[164] L. Wenning and M. H. Müser, "Friction laws for elastic nanoscale contacts," *EPL (Europhysics Letters)*, vol. 54, no. 5, p. 693, 2001.

[165] A. Vernes, S. Eder, G. Vorlaufer, and G. Betz, "On the three-term kinetic friction law in nanotribological systems," *Faraday Discuss.*, vol. 156, pp. 173–196, 2012.

[166] R. M. Overney, H. Takano, M. Fujihira, W. Paulus, and H. Ringsdorf, "Ansiotropy in friction and molecular stick-slip motion," *Phys. Rev. Lett.*, vol. 72, pp. 3546–3549, May 1994.

[167] J. Y. Park, D. F. Ogletree, M. Salmeron, R. A. Ribeiro, P. C. Canfield, C. J. Jenks, and P. A. Thiel, "High frictional anisotropy of periodic and aperiodic directions on a quasicrystal surface," *Science*, vol. 309, no. 5739, pp. 1354–1356, 2005.

[168] A. J. Weymouth, D. Meuer, P. Mutombo, T. Wutscher, M. Ondracek, P. Jelinek, and F. J. Giessibl, "Atomic structure affects the directional dependence of friction," *Phys. Rev. Lett.*, vol. 111, p. 126103, Sep 2013.

[169] R. P. Feynman, "Forces in molecules," *Phys. Rev.*, vol. 56, pp. 340–343, Aug 1939.

[170] M. R. Sørensen, K. W. Jacobsen, and P. Stoltze, "Simulations of atomic-scale sliding friction," *Phys. Rev. B*, vol. 53, pp. 2101–2113, Jan 1996.

[171] A. Martini, Y. Dong, D. Perez, and A. Voter, "Low-speed atomistic simulation of stickslip friction using parallel replica dynamics," *Tribology Letters*, vol. 36, no. 1, pp. 63–68, 2009.

[172] R. Bennewitz, T. Gyalog, M. Guggisberg, M. Bammerlin, E. Meyer, and H.-J. Güntherodt, "Atomic-scale stick-slip processes on Cu(111)," *Phys. Rev. B*, vol. 60, pp. R11301–R11304, Oct 1999.

[173] J. Nieminen, A. Sutton, and J. Pethica, "Static junction growth during frictional sliding of metals," *Acta Metallurgica et Materialia*, vol. 40, no. 10, pp. 2503 – 2509, 1992.

[174] C. Wieferink, P. Krüger, and J. Pollmann, "Simulations of friction force microscopy on the KBr(001) surface based on *ab initio* calculated tip-sample forces," *Phys. Rev. B*, vol. 83, p. 235328, Jun 2011.

[175] Y. N. Zhang, F. Hanke, V. Bortolani, M. Persson, and R. Q. Wu, "Why sliding friction of Ne and Kr monolayers is so different on the Pb(111) surface," *Phys. Rev. Lett.*, vol. 106, p. 236103, Jun 2011.

[176] S. Cahangirov, S. Ciraci, and V. O. Özçelik, "Superlubricity through graphene multilayers between Ni(111) surfaces," *Phys. Rev. B*, vol. 87, p. 205428, May 2013.

[177] D. Pettifor, *Bonding and structure of molecules and solids*. Oxford University Press, 1995.

[178] J. H. Rose, J. R. Smith, and J. Ferrante, "Universal features of bonding in metals," *Phys. Rev. B*, vol. 28, pp. 1835–1845, Aug 1983.

[179] D. Y. W. Yu and F. Spaepen, "The yield strength of thin copper films on kapton," *Journal of Applied Physics*, vol. 95, no. 6, pp. 2991–2997, 2004.

[180] Y. Zhang, Z. Han, K. Wang, and K. Lu, "Friction and wear behaviors of nanocrystalline surface layer of pure copper," *Wear*, vol. 260, no. 9–10, pp. 942 – 948, 2006.

[181] N. Poondla, T. Srivatsan, A. Patnaik, and M. Petraroli, "A study of the microstructure and hardness of two titanium alloys: Commercially pure and Ti_6Al_4V," *Journal of Alloys and Compounds*, vol. 486, no. 12, pp. 162 – 167, 2009.

[182] E. S. Machlin and W. R. Yankee, "Friction of clean metals and oxides with special reference to titanium," *Journal of Applied Physics*, vol. 25, no. 5, pp. 576–581, 1954.

[183] D. H. Buckley, "Influence of crystal orientation on friction characteristics of titanium single crystals in vacuum," *NASA Technical Note*, 1965.

[184] V. Stolyarov, L. Shuster, M. Migranov, R. Valiev, and Y. Zhu, "Reduction of friction coefficient of ultrafine-grained cp titanium," *Materials Science and Engineering: A*, vol. 371, no. 1–2, pp. 313 – 317, 2004.

[185] W. Kohn, "Image of the fermi surface in the vibration spectrum of a metal," *Phys. Rev. Lett.*, vol. 2, pp. 393–394, May 1959.

[186] N. Chaari, E. Clouet, and D. Rodney, "First-principles study of secondary slip in zirconium," *Phys. Rev. Lett.*, vol. 112, p. 075504, Feb 2014.

[187] T. Murakami, H. Mano, K. Kaneda, M. Hata, S. Sasaki, and J. Sugimura, "Friction and wear properties of zirconium and niobium in a hydrogen environment," *Wear*, vol. 268, no. 56, pp. 721 – 729, 2010.

[188] M. Wolloch, G. Feldbauer, P. Mohn, J. Redinger, and A. Vernes, "Ab-initio friction forces on the nanoscale: A DFT study of fcc Cu(111)," August 2014, http://arxiv.org/abs/1408.6059.

Acknowledgments

In many ways this section of the thesis is the most important one, mainly because it gives me a chance to thank all the people who, although they may not be represented on the title page, made this work possible. But also because most of the people I am going to show this thesis will, in all likelihood, only read this few paragraphs. I want to start of by acknowledging that the $3^{1}/_{2}$ years that it took me to carry out the work and compress it into this thesis where the best of my life and this is due to the people I want to thank now:

My advisers, Peter Mohn, Josef Redinger, and András Vernes for all their help and effort and especially the following things: Peter for being the best possible boss and for making me again believe in my work at the worst of times. Sepp for fitting me in his incredibly busy schedule and always finding and correcting the weak point in my arguments. András for the wild, bubbling flow of ideas which, while not all realizable in the available time, formed the foundation of all my work.

My family for their unwavering support, unconditional love, and for making me the person that I am today. I want to thank my mom, Christl, especially for giving me the courage to start this endeavor by pointing out a very important truth that somehow eluded me at that time, namely that I could quit at any time if I am not smart enough to do a PhD. I want to thank my dad, Fredi, for being such a perfect role model for me and for all the incredible advise he gave me during my childhood and adult live. I want to thank my sister, Nora, especially for all the great times we had in the last years and the way she makes me feel whenever I am with her. I hope she is nearly as proud of me as I am of her.

I want to thank my wonderful girlfriend, Simone, for being the most important reason that the last $3^{1}/_{2}$ years where indeed the best years of my life. You are the smartest, funniest, kindest and most beautiful woman I could ever wish for and I still marvel at the fact that you choose to be with me. I love you!

Franz-Philipp Schmidt was and is an integral part of my life as a physicist and without our discussions and arguments I would not have understood most of my undergraduate courses to the extend I did. Since you went back to Graz I miss you profoundly, both in my private and my working life, and hope we continue to keep in touch even when your academic career takes you to France, Switzerland, the USA or some other place that

offers you the professorship that you will eventually accept.

My colleagues, collaborators and friends Andi, Christoph, Gregor, Jacky, Marcel, Robert, Pedro, and Wernfried (in alphabetical order I hope). You guys! You are the main reason I will miss the CMS more than I can probably imagine right now. Thank you, thank you, thank you!

Maria Steiner was not only helpful with all the organizational stuff around the office, but also funny, kind, and a general pleasure to be around and this are only some of the reasons I am thankful to her.

In the prominent and prestigious last place in the longer than expected thank-you-list, that I strangely wrote in English as I only just now realize, are my friends. Manuel, Sandra, Hannah, Andi, Kathi, Agi, Juli, Heinzi, Melli, Jan, ... The list could go on of course, but as there is no good place to stop I might as well do it after 10 names. You all know very well how much I love you and that you make up the best circle of friends in the world. Once I graduate you will automatically be appointed to deputy-PhDs as you are such a big part of me!